Dissertation

Optical Study of Spin and Charge Dynamics in Hybrid Nanostructures and Perovskite Semiconductors

submitted in partial fulfillment of the requirements for the degree of

Dr. rer. nat.

to the Department of Physics at
TU Dortmund University, Germany

by

Eyüp Yalcin

Dortmund, March 2025

TU Dortmund University, Germany

dortmund university

Department of Physics

Date of submission: 26th March 2025

Accepted by the Department of Physics, TU Dortmund University, Dortmund, Germany

Date of the oral examination: 30th May 2025

Examination board:

Prof. Dr. Ilya A. Akimov
Prof. Dr. Mirko Cinchetti
Prof. Dr. Dr. Wolfgang Rhode
PD Dr. Jörg Bünemann

Abstract

The optical orientation and spin dynamics of charge carriers in semiconductors, such as electrons or holes, are of importance in the development of spintronic devices. Currently, there is a great interest in establishing hybrid structures, where the combination of different materials leads to the emergence of new properties. Moreover, lead halide perovskite semiconductors represent a new material system for spintronics, where optical studies of spin dynamics are poorly investigated even in bulk single crystals.

In this work, time-integrated and time-resolved magneto-optical spectroscopy and single beam pump-probe methods are used at low temperatures to investigate the spin dynamics in three type of semiconductor systems.

First, long-range magnetic proximity effect is demonstrated in hybrid systems comprising a semimetal (magnetite Fe_3O_4) or a dielectric (nickel ferrite $NiFe_2O_4$), paired with a CdTe quantum well separated by a nonmagnetic (Cd,Mg)Te barrier. The proximity effect is manifested as the ferromagnet-induced circular polarization of photoluminescence on acceptor-bound holes from the QW and shows an universal behavior. Additionally, it is demonstrated that electrons become slowly polarized indirectly, due to spin-dependent recombination.

Second, the spin dynamics of localized electrons in $MoSe_2$-EuS hybrid structure is investigated. The spin dephasing of such electrons is determined by random effective magnetic fields arise from contact spin interactions, such as the hyperfine interaction with the nuclei in $MoSe_2$ or the exchange interaction with the magnetic ions of the EuS film.

Finally, a high degree of optical orientation of 85 % is demonstrated in lead halide perovskite crystals ($FA_{0.9}Cs_{0.1}PbI_{2.8}Br_{0.2}$ and $MAPbI_3$) which is attributed purely on selection rules for optical transitions and slow spin relaxation in crystals with spatial inversion symmetry.

Kurzfassung

Die optische Orientierung und Spindynamik von Ladungsträgern in Halbleitern, wie Elektronen oder Löcher, sind für die Entwicklung von spintronischen Bauelementen von Bedeutung. Derzeit besteht großes Interesse an der Entwicklung hybrider Strukturen, bei denen die Kombination verschiedener Materialien zu neuen Eigenschaften führt. Darüber hinaus stellen Bleihalogenid-Perowskit-Halbleiter ein neues Materialsystem für die Spintronik dar, in dem optische Studien zur Spindynamik, selbst in massiven Einkristallen, bisher nur wenig erforscht sind.

In dieser Arbeit werden zeitintegrierte und zeitaufgelöste magneto-optische Spektroskopie, sowie Einzelstrahl-Pump-Probe-Methoden bei niedrigen Temperaturen verwendet, um die Spindynamik in drei Arten von Halbleitersystemen zu untersuchen.

Erstens wird der langreichweitige magnetische Proximity-Effekt in Hybridsystemen gezeigt, die aus einem Halbmetall (Magnetit Fe_3O_4) oder einem Dielektrikum (Nickelferrit $NiFe_2O_4$) bestehen, kombiniert mit einem CdTe-Quantentopf, getrennt durch eine nichtmagnetische (Cd,Mg)Te-Barriere. Der Proximity-Effekt äußert sich in der ferromagnetisch induzierten zirkularen Polarisation der Photolumineszenz an akzeptorgebundenen Löchern aus dem Quantentopf und zeigt ein universelles Verhalten. Zusätzlich wird gezeigt, dass die Elektronen aufgrund spinabhängiger Rekombination langsam indirekt polarisiert werden.

Zweitens wird die Spindynamik lokalisierter Elektronen in einer $MoSe_2$-EuS Hybridstruktur untersucht. Die Spindephasierung solcher Elektronen wird durch zufällige effektive Magnetfelder bestimmt, die durch Kontakt-Spin-Wechselwirkungen entstehen, wie die Hyperfeinwechselwirkung mit den Kernen in $MoSe_2$ oder die Austauschwechselwirkung mit den magnetischen Ionen des EuS-Films.

Schließlich wird ein hoher Grad der optischen Orientierung von 85 % in Bleihalogenid-Perowskit-Kristallen ($FA_{0.9}Cs_{0.1}PbI_{2.8}Br_{0.2}$ und $MAPbI_3$) nachgewiesen, der ausschließlich auf den Auswahlregeln für optische Übergänge und die langsame Spinrelaxation in Kristallen mit räumlicher Inversionssymmetrie zurückzuführen ist.

Contents

1 Introduction

The spin of charge carriers in semiconductors such as electrons or holes are often considered as a carrier of information. Here, optical and magnetic control can be established. Firstly, the electron spin can be initialized optically in semiconductors using circularly polarized light. Here, selection rules for optical transitions and the mechanisms of spin relaxation play important role in the temporal dynamics of spin, influencing potential applications. Secondly, use of magnetic components enables further control over electron spin, particularly via the exchange interaction with magnetic ions. Currently there is a great interest in establishing hybrid structures, where the combination of different materials leads to the emergence of new properties. Moreover, lead halide perovskite semiconductors represent a new material system for spintronics, where optical studies of spin dynamics are poorly investigated even in of bulk single crystals.

The integration of magnetism into solid-state electronics is recognized as a key challenge in the development of devices that combine information processing and magnetic recording on a single chip. Strong and tunable coupling between distinct spin systems is required. One such coupling example is the Ruderman-Kittel-Kasuya-Yosida (RKKY) interaction, where the magnetization of an electron gas near a magnetic ion induces an indirect exchange interaction between two magnetic ions. This occurs because the second ion interacts with the magnetization of electrons induced by the first ion [1]. This short-range interaction, on a scale below 1 nm, is determined by the overlap of electron wave functions, imposing high demands on the quality of interfaces between different spin systems for semiconductor spintronics.

Short-range exchange interactions have been employed to control magnetization in metallic nanosystems [2]. This approach is based on the spin-orbit torque [3] that arises from the flow of an electric current. However, the necessity for high current densities ($\sim 10^6\,\mathrm{A\,cm^{-2}}$) limits the integration of this method into semiconductors, leading to the need for alternative solutions.

New properties have been discovered in hybrid ferromagnet-semiconductor (FM-SC) systems [4] when magnetic and semiconductor materials are brought into contact. These systems exhibit both magnetic ordering and excellent optical properties [5, 6, 7]. Additionally, the magnetic moment of the ferromagnet can be tuned via an electric field by applying a bias voltage [8].

A novel long-range exchange interaction, unrelated to the overlap of charge carrier wave functions, was revealed in hybrid FM-SC quantum well (QW) structures [9]. It was suggested that this spin-spin interaction is mediated by elliptically polarized phonons, which exist in ferromagnets due to the breaking of time-reversal symmetry. These phonons penetrate from the ferromagnet through a nonmagnetic semiconductor spacer into the QW while maintaining their circular polarization over distances of several tens of nanometers. The energies of spin levels of holes bound to acceptors in the QW are modified by the spin-phonon interaction.

As a result, an effective p-d exchange interaction is created between the spin of acceptor-bound holes (p-system) and the angular momentum of the phonons, which is

proportional to the magnetization of the ferromagnetic film, carried by its d-electrons. This effect can be viewed as the interaction of the hole spin with an effective magnetic field (approximately 2 T), proportional to the phonon angular momentum. The phenomenon is similar to the spin-dependent optical Stark effect [10] (or inverse Faraday effect [11]) in the optics of atoms and solids, where energy levels are shifted under illumination with circularly polarized light. By analogy, this phenomenon has been termed the phonon Stark effect (or phonon inverse Faraday effect) [9].

The phonon Stark effect can be controlled electrically without current flow and without energy losses [12]. These findings are among the first in a series of notable results on chiral phonon-induced spin phenomena, which are reviewed in Reference [13].

In contrast to the short-range exchange interaction, the long-range exchange mechanism mediated by elliptically polarized phonons does not impose stringent requirements on interface quality. This suggests that the long-range proximity effect is likely universal, occurring in FM-SC hybrid structures with various ferro- and ferrimagnetic materials, and thus opening up prospects for practical applications. Prior studies of the long-range proximity effect have been conducted in FM-SC structures containing a CdTe/(Cd,Mg)Te QW near a metallic FM layer made of cobalt or iron [9, 12, 14, 15, 16].

In Chapter 6 it is demonstrated that the long-range magnetic proximity effect is also present in hybrid structures where the metallic FM layer is substituted by a semimetal (magnetite Fe_3O_4) or a dielectric (nickel ferrite $NiFe_2O_4$) FM. The effect is manifested in the FM-induced circular polarization of photoluminescence (PL) from the CdTe QW, independent of wave function overlap. In contrast to metal-based systems, the proximity effect in these structures is induced by the magnetic material itself (i.e., magnetite or nickel ferrite), rather than by the interfacial ferromagnetic layer.

As in previous studies, the FM-induced PL polarization in both types of systems is attributed to the Zeeman splitting of acceptor-bound holes. The effect is shown to be resonant, as no FM-induced spin polarization of valence band holes (excitonic holes) is observed, due to the critical role of the splitting between heavy and light hole states relative to the phonon energy. Moreover, it is shown that the FM does not directly affect the polarization or frequency of electron Larmor precession in the QW. Instead, electrons become slowly polarized indirectly, due to spin-dependent recombination with acceptor-bound holes.

These results, combined with earlier findings from metal-based hybrid structures, indicate the universal origin of the long-range proximity effect.

Spin-related phenomena in two-dimensional (2D) van der Waals semiconductors such as transition metal dichalcogenides (TMDs) have attracted considerable attention due to their unique energy level structure with spin-valley locking resulting from a strong spin-orbit interaction. The direct bandgap excitons, characterized by large binding energies and high oscillator strengths, determine the extraordinary optical properties of these materials. Novel spin phenomena and their potential applications in spin-based photonic devices are of particular interest [17, 18, 19, 20].

So far, the energy level structure of neutral and charged excitons as well as their spin and valley dynamics in monolayers have been extensively studied. In particular, excitons in Mo-based dichalcogenide monolayers exhibit well-defined selection rules for optical transitions, ultrashort lifetimes on the order of several picoseconds, and fast spin relaxation due to the electron-hole exchange interaction [21]. These properties enable efficient spin-valley pumping of the resident charge carriers with circularly polarized light [22, 23].

In addition, optical experiments have shown exceptionally long spin lifetimes for electrons, reaching hundreds of nanoseconds, with even longer lifetimes observed for holes [24, 25, 26, 27]. In References [24] and [25] the anisotropic spin relaxation of electrons in 2D monolayers was used to explain the spin depolarization of resident electrons in a weak transverse magnetic field of about 10 mT.

The spin dynamics in low-dimensional nanostructures are very sensitive to the anisotropy of magnetic interactions and spin relaxation processes involving both excitons and resident charge carriers. These effects can be studied via spin depolarization in a transverse magnetic field (Hanle effect) and polarization recovery in a longitudinal magnetic field (polarization recovery effect) [28]. The anisotropy is most evident in the angular dependence of the polarization curves, i.e. in the transition from the Hanle effect to the polarization recovery effect in an oblique magnetic field (anisotropic Hanle effect). For excitons, the anisotropic Hanle effect was reported in WSe_2 monolayers [29] and CdSe/ZnSe quantum dots [30]. For electrons, the anisotropy of the g-factor in GaAs/AlGaAs quantum wells was determined using this approach [31]. However, the investigation of resident carrier spins in oblique magnetic fields in 2D van der Waals materials is still largely unexplored.

In Chapter 7 the spin polarization of resident electrons in a hybrid monolayer $MoSe_2$/EuS structure is investigated under resonant optical pumping in an oblique external magnetic field at cryogenic temperatures. An anisotropic Hanle effect is found for resident electrons in $MoSe_2$/EuS, which results from a significant anisotropy of both the electron g-factor and the spin relaxation time. The Hanle effect is strongly influenced by static random fluctuations of an effective magnetic field originating from the hyperfine interaction of localized electrons with the nuclei in $MoSe_2$ or from the exchange interaction between these electrons and the spins of Eu ions in EuS with an interaction strength of several mT.

This interaction leads to an extraordinary Hanle effect. First, in a transverse magnetic field, a depolarization width of only a few mT is observed, which corresponds to a long spin relaxation time of the resident electrons, as confirmed by time-resolved pump-probe measurements. Second, an even larger polarization recovery with a comparable width is observed in a longitudinal magnetic field. This observation suggests that random fluctuations of the effective magnetic field acting on localized electrons play a crucial role in their spin depolarization in a zero external magnetic field. From the dependence of spin polarization on the magnitude and orientation of the external magnetic field, the anisotropy of the g-factor of the interval electrons and the spin relaxation time is determined.

It is emphasized that the EuS film is ferromagnetic, but does not interact directly with the monolayer due to possible oxidation of the EuS surface and therefore there is no giant Zeeman splitting due to a magnetic exchange field as reported in References [32, 33, 34]. Nevertheless, the experimental approach based on the technique of a single laser beam in combination with narrow Hanle curves shows the potential for the application of 2D electrons in $MoSe_2$ for magnetic sensing.

The Hanle and spin polarization recovery effects are investigated for resident electrons in a monolayer $MoSe_2$ on EuS. It is shown that localized electrons provide the dominant contribution to the spin dynamics signal at low temperatures below 15 K for small magnetic fields of only a few mT. The spin relaxation of these electrons is determined by random effective magnetic fields arising from contact spin interactions, in particular the hyperfine interaction with the nuclei in $MoSe_2$ and the exchange interaction with the magnetic ions in the EuS film. From the angular dependence of the spin polarization in the external magnetic field, the anisotropy of the interval electron g-factor and the

spin relaxation time is determined. The non-zero in-plane g-factor, $|g_x| \approx 0.1$, which is comparable to its dispersion, is attributed to randomly localized electrons in the $MoSe_2$ layer.

Lead halide perovskite semiconductors are known for their exceptional photovoltaic efficiencies [35, 36] and their optoelectronic properties [37, 38]. Their simple and cost-effective manufacturing processes make them extremely attractive for applications in solar cells and light-emitting devices. In addition to their optical and electronic properties, these materials exhibit remarkable spin properties that make them promising candidates for quantum technologies and spintronic applications [38, 39, 40, 41].

The study of spin physics in halide perovskite semiconductors remains an emerging field that utilizes experimental techniques and theoretical concepts originally developed for conventional semiconductor spin systems [42]. Various spin-dependent optical techniques have been successfully applied to perovskite single crystals, polycrystalline films, two-dimensional (2D) materials and nanocrystals. These techniques include optical orientation [43, 44], optical alignment [44], polarized photoluminescence in external magnetic fields [45, 46], time-resolved Faraday and Kerr rotation [47, 48], spin-flip Raman scattering [49, 50], and optically detected nuclear magnetic resonance (ODNMR) [51]. An universal dependence of the Landé factors for electrons, holes and excitons on the band gap energy has been established [49, 52]. The reported spin dynamics span a wide temporal range, from a few picoseconds at room temperature [43, 53] to tens of nanoseconds for spin coherence [54] and spin dephasing [51], and even into the sub-millisecond range for longitudinal spin relaxation times [55] at cryogenic temperatures.

Optical orientation is a fundamental effect in spin physics [28, 42], in which circularly polarized photons generate spin-polarized excitons and charge carriers. Their spin polarization can be studied dynamically using various techniques, including polarized photoluminescence, Faraday and Kerr rotation, and spin-dependent photocurrents. The use of ultrashort optical pulses with a duration of less than a picosecond enables ultrafast spin initialization, manipulation and readout, which are crucial for quantum information applications. In lead halide perovskites, optical orientation under pulsed excitation has been used to initiate spin dynamics in polycrystalline films [43, 47], bulk crystals [48, 51], nanocrystals [53, 56], nanoplatelets [57], and 2D perovskite materials [58, 59, 60]. In addition, optical spin manipulation of charge carriers in singly charged $CsPbBr_3$ nanocrystals at room temperature has recently been demonstrated [61].

The electronic band structure of lead halide perovskites is particularly favorable for the optical orientation of charge carriers and excitons. The selection rules for optical transitions allow spin polarization of charge carriers upon absorption of circularly polarized photons as well as nearly 100 % polarized luminescence. This is in contrast to conventional III-V and II-VI bulk semiconductors (such as GaAs and CdTe), where the maximum degree of optical orientation observable in photoluminescence is limited to 25 %. In time-resolved measurements of polarized differential transmission, the excitation of highly spin-polarized charge carriers has been demonstrated [43, 57, 59]. However, in the temperature range from 77 K to 300 K, the spin relaxation time of the charge carriers is remarkably short (less than 3 ps), which leads to their depolarization before recombination. The differential transmission technique does not allow to distinguish the spin polarization of electrons, holes and excitons.

Under continuous wave excitation, only low degrees of optical orientation, measured via the circular polarization of the photoluminescence, have been reported so far. For polycrystalline $MAPbBr_3$ films, a degree of polarization of 3.1 % at 10 K was observed

[39], whereas values of 2 % [62] and 8 % [63] at 77 K were measured. For $MAPbI_3$ an even lower degree of 0.15 % was measured at 77 K [62], while in $CsPbI_3$ nanocrystals a degree of polarization of 4 % was found at 2 K [44]. These results highlight the current challenge of determining the maximum achievable optical orientation in perovskites, identifying the mechanisms limiting spin generation and relaxation, and distinguishing the spin dynamics of electrons, holes and excitons.

In Chapter 8 the spin dynamics of excitons and localized charge carriers in $FA_{0.9}Cs_{0.1}PbI_{2.8}Br_{0.2}$ bulk perovskite and $MAPbI_3$ thin crystals are investigated using the optical orientation technique at cryogenic temperatures. The spin polarization of excitons and charge carriers is detected by polarized photoluminescence, and time-resolved measurements are used to find out their respective contributions. A high optical orientation degree of 85 % is observed for excitons, and this polarization remains stable with respect to the detuning of the excitation energy towards the exciton resonance. Furthermore, the dynamics of spin polarization is studied in both longitudinal and transverse magnetic fields, which allows the determination of the spin relaxation times of excitons and charge carriers.

Part I

Theoretical Background

2 Semiconductor Physics

This chapter provides an overview on the basic semiconductor physics and presents the band structure in Section 2.1 and effects of low dimensions due to confinement in general in Section 2.2, for quantum wells in Section 2.3 and monolayer semiconductor in Section 2.4. The selection rule for optical transition and spin relaxation processes are discussed in Sections 2.5 and 2.6.

2.1 Electronic Band Structure of Semiconductors

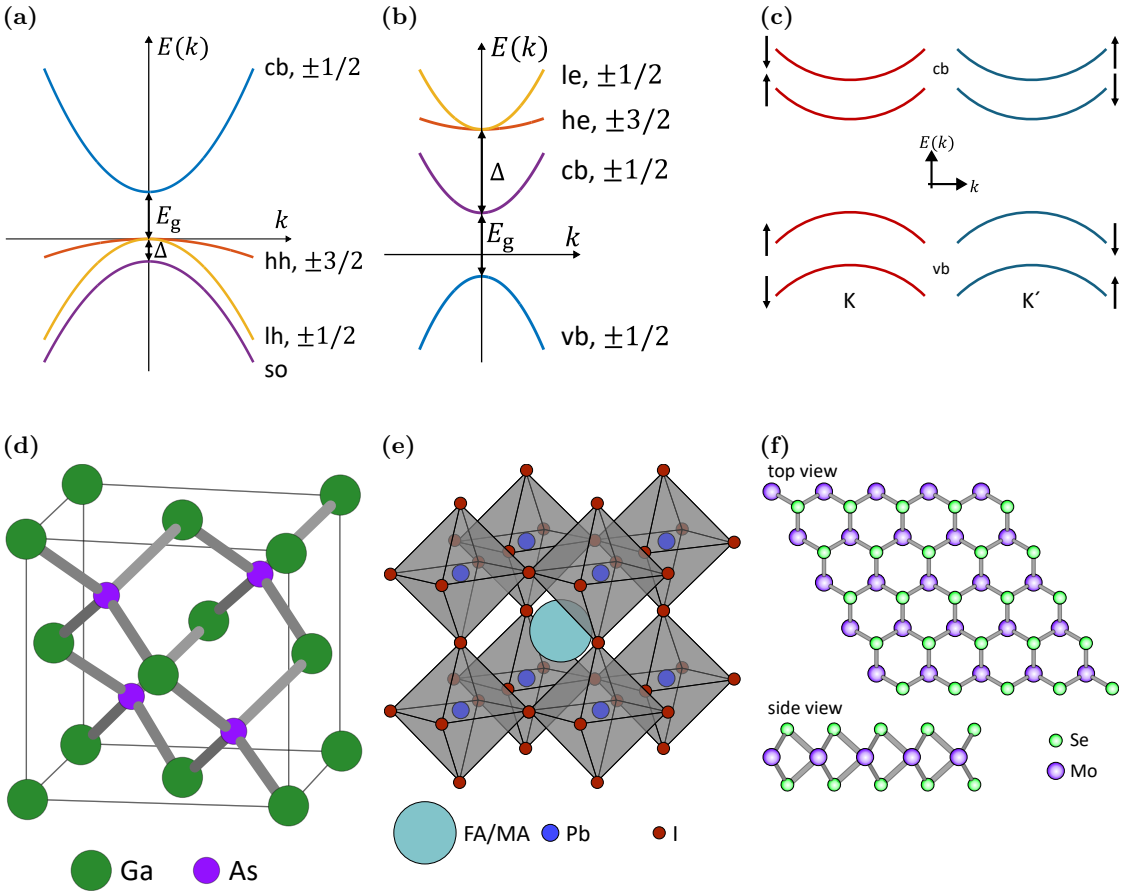

Figure 2.1: Electronic band structure of gallium arsenide (GaAs) 2.1a with s-type conduction band (cb) and p-type valance band (vb) [64, p. 348], lead halide perovskite ($FAPbI_3$/$MAPbI_3$) 2.1b with p-type cb and s-type vb [49], and TMD monolayer of molybdenum diselenide ($MoSe_2$) 2.1c [65, 66]. The bands are denoted with cb, vb, heavy-hole (hh), light-hole (lh), split-off band (so), light-electron (le) heavy-electron (he), spin-up (↑) and spin-down (↓). Their crystal structures are shown below the electronic band structure in Figures 2.1d–2.1f [1, p. 18][67][65, 66].

The electronic band structure of a semiconductor is calculated using the Bloch theorem. The wave function of a charge carrier in a periodic potential $U(r) = U(r + R)$, where R is the periode of the lattice, is described as the product of a plane wave and a function with the periodicity of the crystal:

$$\Psi(r)E = \Psi(r)\left[-\frac{\hbar^2\nabla^2}{2m^*} + U(r)\right], \tag{2.1}$$

$$\Psi(r) = e^{ikr}u(r), \tag{2.2}$$

where Equation (2.1) represents the crystal Hamiltonian, E is the energy eigenvalues, $\hbar$ the reduced Planck's constant, ∇ the nabla operator, and m^* the effective mass of the electron. Equation (2.2) defines the wave function, where e^{ikr} describes a plane wave, k the wave vector of the carrier, and $u(r)$ is the Bloch function that is periodic with R.

The solution of the Bloch functions leads to the formation of energy bands in momentum space k, as shown in Figure 2.1. The optical band gap is defined as the energy difference between the minimum of the conduction band (cb) and the maximum of the valence band (vb).

In the following semiconductors with direct band gap, lead halide perovskites and transition metal dichalcogenide monolayer will be discussed. Semiconductors with a zinc blende crystal structure (e.g. ZnSe, GaAs, CdTe, Figure 2.1d) exhibit a direct band gap at the Γ-point in the Brillouin zone. The spin-orbit coupling leads to an overall angular momentum for the conduction band similar to the orbitals of s-type, characterized by $J = L + S = 0 + 1/2 = 1/2$. For the valence band, the angular momentum is similar to orbitals of the p-type, where $J = 1 + 1/2 = 3/2$. Within the valence band, the orientation quantization of the total angular momentum $J = 3/2$ leads to bands with the quantum numbers $m_J = \pm 3/2, \pm 1/2$, which correspond to the heavy-hole (hh, $m_J = \pm 3/2$) and light-hole bands (lh, $m_J = \pm 1/2$). In addition, a split-off band (so) with $J = 1/2$ and $m_J = \pm 1/2$ is present. Thus only the heavy- and light-hole bands are relevant for the optical properties near the band edge. [68, 69, 70, 71] The degeneracy between light- and heavy-hole bands at $k = 0$ is usually lifted in low dimensional systems [71]. A schematic representation of the GaAs band structure is shown in Figure 2.1a.

The electronic band structure in the vicinity of Γ-point of the Brillouin zone is described by the following expression

$$E = \frac{\hbar^2 k^2}{2m^*}, \tag{2.3}$$

where $\hbar$ denotes the reduced Planck's constant, k the wave vector and m^* the effective mass of the electron or hole. The shape of the bands depends on the effective mass.

Perovskites are semiconductors with the general formula ABX_3, where A is a cation, B is a metal and X is a halide, have a direct band gap at the R-point in the Brillouin zone. The crystal structure for a lead halide perovskite is shown in Figure 2.1e with formamidinium (FA) or methylammonium (MA) as cation, lead (Pb) as metal and iodide (I) as halide. The band structure of perovskites can be strongly adjusted by changing the composition of A, B and X. [64] In these materials, energy band splitting occurs in the conduction band, as shown in Figure 2.1b. It has an inverted band structure as compared to GaAs, where valence band holes have s-type and conduction band electrons p-type Bloch function. [72]

$MoSe_2$ is a transition metal dichalcogenide (TMD) and has an indirect band gap of about 1.1 eV in its bulk form. In a monolayer, this band gap changes to a direct band gap

with a value of about 1.55 eV and strong spin-orbit coupling effects occur. These effects split the conduction and valence bands at the K-point, which leads to the formation of spin-polarized subbands, as shown in Figure 2.1c. [68, 69, 70, 71]

2.2 Semiconductor Nanostructures

The artificial production of nanostructures allows to create semiconductor structures with confinement of the motion of electrons and holes in one or more dimensions.

From the Heisenberg uncertainty principle follows that a confined particle to a region of the z-axis with the length Δz causes an uncertainty in its linear momentum

$$\Delta p_z \sim \frac{\hbar}{\Delta z} \tag{2.4}$$

and additional kinetic energy in the z direction of the confinement

$$E_{\text{confinement}} = \frac{\Delta p_z^2}{2m} \sim \frac{\hbar^2}{2m\Delta z^2}. \tag{2.5}$$

This confinement energy becomes significant if it is greater or comparable to the kinetic energy of the particle to its thermal motion in z direction:

$$E_{\text{confinement}} \gtrsim \frac{1}{2} k_{\text{B}} T \tag{2.6}$$

This relation can be transformed to

$$\Delta z \lesssim \sqrt{\frac{\hbar^2}{m k_{\text{B}} T}} \tag{2.7}$$

in order to estimate the scales at which quantum effects appears and it is equivalent to

$$\Delta z \lesssim \frac{h}{p_z} = \lambda_{\text{deB}} \tag{2.8}$$

for the thermal motion, where λ_{deB} is the de Broglie wavelength. [70]

For a thermal energy $k_{\text{B}}T \approx 25\,\text{meV}$ at room temperature ($T = 293\,\text{K}$) follows for an electron effective mass $m_{\text{e}}^* = 0.1 m_{\text{e}}$ in a semiconductor from Equation (2.7) the length $\Delta z \approx 5.5\,\text{nm}$ [64, 70]

2.3 Quantum Wells

The confinement of a semiconductor crystal in one dimension is called quantum well (QW). By considering a QW where the motion of the electron is free in the x and y planes and confined and quantized along the z-axis, Equation (2.2) has to multiplied with an envelope function $\phi_n(z)$ and it follows

$$\Psi_n\left(\vec{r}, \vec{k}\right) = u(\vec{r}) e^{i(k_x x + k_y y)} \cdot \phi_n(z) \tag{2.9}$$

where n indicates the energy level for the z direction. By solving the equation for a potential well the total energy is obtained

$$E\left(n, \vec{k}\right) = E_n + E\left(\vec{k}\right), \tag{2.10}$$

where E_n is the quantized energy of the n-th level and $E\left(\vec{k}\right)$ is known from Equation (2.3). The solution of E_n in an infinite potential well is given by

$$E_n = \frac{\hbar^2}{2m^*}\left(\frac{n\pi}{d_{\mathrm{QW}}}\right)^2, \tag{2.11}$$

where d_{QW} is the width of the quantum well and n an integer that gives the quantum number of the state. The ground state is $n = 1$ and higher n are the excited states of the system. The quantized energy E_n is proportional to the state n^2 and inversely proportional to the effective mass m^* and the square of the quantum well width d_{QW}. Thus a particle with low mass in a narrow quantum well have the highest energies. Due to dependence of the energy on the effective mass, the electrons, heavy holes and light holes have different quantization energies.

The infinite model overestimates the quantization energy, but the results are valid for the more realistic case of a finite potential well. In the finite potential well the wave function $\phi_n(z)$ penetrates exponential decaying by tunnelling of the particle into the barrier and there is a finite number of quantized states. [70, 71]

2.4 Semiconductor Monolayer

Transition metal dichalcogenides (TMDs or TMDCs) as two-dimensional (2D) materials form stable monolayers with strong in-plane bonding and weak van der Waals interactions with neighboring (barrier) layers.

TMDs are semiconducting materials with the general formula MX_2, where M stands for a transition metal and X for a chalcogen. They exhibit fundamental optical transitions in the visible and adjacent spectral range.

Most single-layer materials have a hexagonal Brillouin zone, which corresponds to a triangular Bravais lattice in real space. The fundamental band gap between the valence and conduction band occurs at the K and K′ points of the Brillouin zone.

The K and K′ points are not equivalent if the inversion symmetry of the crystal is broken. This condition is fulfilled in TMD lattices, whereas in graphene, all sites of the honeycomb lattice are occupied by the same type of atoms, which preserves the inversion symmetry.

Spin-orbit coupling has significant consequences. It leads to a spin-orbit splitting in the conduction bands and to a considerably larger splitting in the valence bands. The spin degeneracy in each valley is canceled. The spin-up state in the K valley remains degenerate with the spin-down state in the K′ valley. The spin-orbit interaction couples the degrees of freedom of spin and valley, whereby the valley degree of freedom can theoretically be treated as pseudo-spin. As a result of this so-called spin-valley locking, the valley occupation at K or K′ can be selectively controlled, for example by choosing the circular polarization of the absorbed photons. Spin-valley locking enables the field of valleytronics, since electronic transport properties become valley-dependent.

The electronic band structure of TMDs is primarily characterized by the dominant contribution of the d electron bands to both the conduction and valence bands. As mentioned above, the band extrema are located at the K and K′ points of the Brillouin zone. Some TMDs, such as $MoSe_2$ and WS_2, exhibit an indirect band gap in the bulk phase (and even in bilayers), but switch to direct in the monolayer due to quantum confinement and changes in the hybridization of the electronic wave functions.

The optical transitions associated with spin-valley locking in TMDs are determined by strongly bound excitonic states. The large exciton binding energies result from the high effective masses of the electrons and holes, the reduced dielectric shielding, which is characteristic of (quasi-)2D systems, and the confinement of charge carriers in a single monolayer.

The nature of the fundamental excitonic transition in TMDs is strongly influenced by exchange interactions within the valleys. In $MoSe_2$ and $MoTe_2$, the excitonic state with the lowest energy is bright, while in WSe_2 and WS_2 the excitonic state with the lowest energy is dark. [71]

2.5 Spin Systems and Selection Rules for Optical Transitions

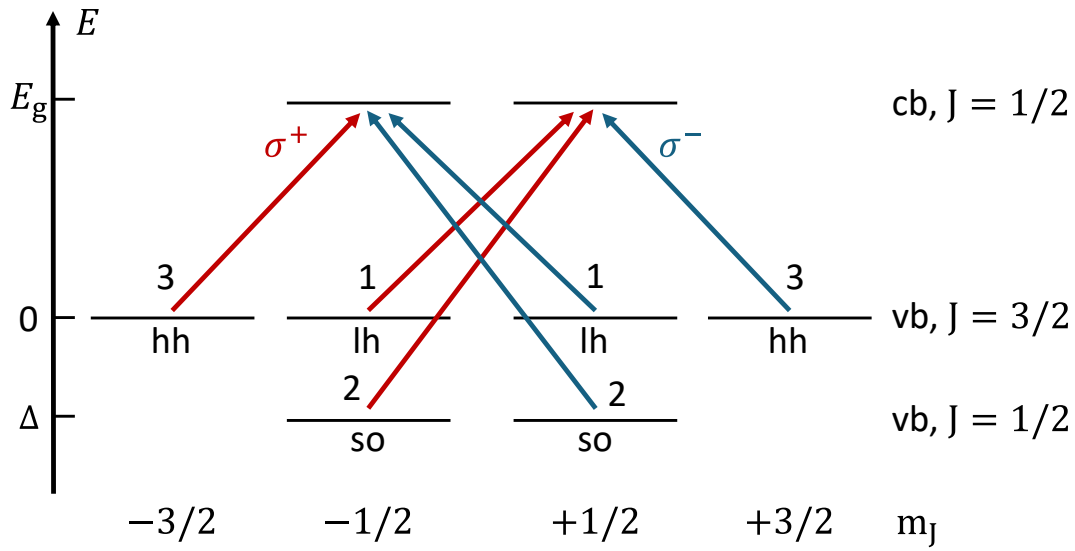

Figure 2.2: Schematic illustration of the selection rules in a zinc-blende structure with optical transition from valence band (vb) to conduction band (cb) and with the polarization σ^+ (red) and σ^- (blue), the transition probabilities at the arrows for the spin states m_J. [64, p. 348]

The conservation of angular momentum is a fundamental law of physics. Similar to particles, electromagnetic waves, i.e. photons have an angular momentum of 1.

Photons of right- or left-polarized light have a projection of angular momentum along their direction of propagation (helicity) that is equal to $+1$ or -1 in units of $\hbar$. Linearly polarized photons are described as a superposition of these two helicity states. When a circularly polarized photon is absorbed, its angular momentum is distributed between the photoexcited electron and the hole according to the selection rules given by the band structure of the semiconductor.

Due to the complex nature of the valence band in a zinc-blende structure (see Figure 2.1a), this angular momentum distribution depends on the momentum p of the generated electron-hole pair (p and $-p$). It can be shown that the averaging over all directions of p leads to a result that is analogous to optical transitions in atomic states. These states correspond to $J = 3/2$ and $m_J = -3/2, -1/2, +1/2, +3/2$, associated with the light and heavy holes in the valence band, and $J = 1/2$ and $m_J = -1/2, +1/2$ associated with the conduction band.

The possible transitions between these states as well as the transitions between the split-off band and the conduction band during the absorption of a left- and right-hand circularly polarized photon are shown in Figure 2.2 together with their relative probabilities (number at begin of arrow).

The spin polarization of excited electrons is defined as the relative spin degree for the transition from vb to cb with its bands $m_J = +1/2$ and $m_J = -1/2$ for a circular polarized excitation

$$P_n = \frac{n_+ - n_-}{n_+ + n_-} \tag{2.12}$$

where the electron densities n_+ for spin up and n_- for spin down polarized parallel ($m_J = +1/2$) and antiparallel ($m_J = -1/2$) to the direction of light propagation.

The relative probabilities from the vb into the cb for the heavy hole $m_J = \pm 3/2$ is 3, for the light hole $\pm 1/2$ is 1 and the split-off band $\pm 1/2$ is 2. [73] For an excitation with σ^+ polarized light and the photon energy $E_\mathrm{g} < \hbar\omega < E_\mathrm{g} + \Delta$ follows for the polarization degree of electrons in GaAs bulk

$$P_n = \frac{1-3}{1+3} = -\frac{2}{4} = -\frac{1}{2} = -50\,\%\,, \tag{2.13}$$

and for the photon energy $\hbar\omega > E_\mathrm{g} + \Delta$

$$P_n = \frac{(1+2)-3}{(1+2)+3} = \frac{0}{6} = 0\,. \tag{2.14}$$

The circular polarization of luminescence is defined as

$$P_\mathrm{circ} = \frac{I^+ - I^-}{I^+ + I^-} \tag{2.15}$$

where $I^\pm$ is the radiation intensity for the helicity $\sigma^\pm$. The intensities $I^\pm$ for electrons and unpolarized holes in GaAs can be described with the electron densities $n_\pm$ and the transition probabilities

$$I^+ = n_+ + 3n_- \tag{2.16}$$

$$I^- = 3n_+ + n_-\,. \tag{2.17}$$

For the photon energy $E_\mathrm{g} < \hbar\omega < E_\mathrm{g} + \Delta$ follows for the maximum circular polarization with spin polarization for σ^+ photoluminescence

$$P_\mathrm{circ} = \frac{(n_+ + 3n_-) - (3n_+ + n_-)}{(n_+ + 3n_-) + (3n_+ + n_-)} \tag{2.18}$$

$$= -\frac{1}{2}P_n = \frac{1}{4} = 25\,\%\,. \tag{2.19}$$

For the photon energy $\hbar\omega > E_\mathrm{g} + \Delta$ follows $P_\mathrm{circ} = P_n = 0\,.$

Due to relaxation processes the circular polarization degree, the achievable circular polarization degree P_circ is decreased and the electron lifetime τ and spin relaxation time τ_s must be taken into account

$$P_\mathrm{circ} = \frac{P_\mathrm{circ,0}}{1 + \tau/\tau_\mathrm{s}}, \tag{2.20}$$

where $P_{\mathrm{circ},0}$ is the theoretically expected circular polarization degree without spin relaxation. The lifetime τ describes the lifetime of the electron in the excited state, before recombination and the spin relaxation time τ_{s} the characteristic time over which the spin polarization of electrons (or holes) decays. It follows for fast spin relaxation $\tau_{\mathrm{s}} \ll \tau$ a smaller polarization degree and for slow spin relaxation times $\tau_{\mathrm{s}} \gg \tau$ close to $P_{\mathrm{circ},0}$. [42, 64, 70, 73]

2.6 Spin Relaxation Processes

There are four mechanisms of spin relaxation for conduction electrons that are considered relevant in metals and semiconductors: the Elliott-Yafet, the Dyakonov-Perel, the Bir-Aronov-Pikus and the hyperfine interaction.

In the Elliott-Yafet mechanism, spin relaxation occurs because the wave functions of the electrons, which are generally associated with a specific spin state, exhibit an admixture of states with opposite spin. This mixing results from the spin-orbit coupling caused by the ions in the crystal lattice.

The Dyakonov-Perel mechanism describes the dephasing of spins in materials that have no center of symmetry. In such systems, an effective magnetic field generated by the combined effects of inversion asymmetry and spin-orbit interaction acts on the electron spins. This effective field changes its direction randomly each time an electron scatters to a different momentum state, leading to spin dephasing.

The Bir-Aronov-Pikus mechanism is important in p-doped semiconductors, where electron-hole exchange interactions generate fluctuating local magnetic fields that invert electron spins.

The hyperfine interaction becomes important when the eigenfunction of the carrier get localized and the number of nuclei with which the carrier interacts becomes smaller. This takes place in case of electrons bound to donors in bulk or in quantum dots where localization is due to 3D confinement. In QW it can also be present due to fluctuations of QW width. [42, 64, 70, 73]

3 Spin in External Magnetic Field

In this chapter a brief introduction about the spin in magnetic field will be given. Applying an external magnetic field to a semiconductor leads to a Zeeman splitting and Larmor precession that can be used to calculate the Landé factor. Magneto-optical Kerr-effects can be used to characterize a sample. By measuring the polarization degree, a decrease or increase in polarization can be observed due to the Hanle effect and polarization recovery, respectively, that can be used to achieve information about spin dynamics of excitons and charge carriers.

In the further sections the theoretical background to understand the effects in this thesis is discussed. These are the single beam pump-probe of spin dynamics approach in Section 3.5, the evolution of spin density of resident electrons in Section 3.6, the long-range magnetic proximity effect in semiconductor hybrid structure in Section 3.7 and the dynamics of exciton and carrier spin precession in magnetic field in perovskites in Section 3.8.

3.1 Magnetism

The strongest magnetic interaction results from the electrostatic Coulomb repulsion between electrons in conjunction with the Pauli exclusion principle. This interaction is known as the exchange interaction and leads to the splitting of energy between singlet and triplet states in atoms.

In condensed matter, the exchange interaction is responsible for correlated magnetism, which exhibits different behaviors such as ferro-, antiferro- and ferrimagnetism. This interaction can be modeled with a simplified Heisenberg-Hamilton formula that only considers the interactions between the nearest neighbors:

$$H_{\mathrm{ex}} = -2C_{\mathrm{exch}} \sum_{i<j} S_i S_j, \tag{3.1}$$

where C_{exch} is the exchange constant, which depends on the overlap of the electron wave functions, and $S_{i,j}$ are the total spin operators for neighboring atoms.

In one-dimensional systems, the three-dimensional spin operator S is replaced by S_z, the spin component along the quantization axis z, resulting in the Ising-Hamiltonian. Depending on the sign of C_{exch}, the ground state has either a parallel ($C_{\mathrm{exch}} > 0$) or an antiparallel ($C_{\mathrm{exch}} < 0$) spin orientation, which corresponds to ferromagnetic or antiferromagnetic behavior.

Ferrimagnets are characterized by two (anti-)ferromagnetically coupled magnetic sublattices whose magnetizations are generally unequal, resulting in a net magnetic moment.

In ferromagnets, spin-orbit interaction plays an important role as the primary source of magnetocrystalline anisotropy. The orbital magnetic moment tends to align along certain crystallographic directions due to the influence of the surrounding charges in the crystal lattice. The spin-orbit interaction couples the spins to these preferred directions, resulting in magnetic alignment along a single direction called the easy axis.

In magnetic films several nanometers thick, shape anisotropy becomes a significant factor, usually aligning the easy axis in the plane of the film. [1]

3.2 Larmor Precession and Anisotropic Landé g-Factor

When an external magnetic field B is applied, the spin-up and spin-down eigenstates are split by Zeeman splitting and an oscillation occurs. The frequency of this Larmor precession ω_L is determined by the spin splitting induced by the magnetic field and is given by

$$\Delta E = \hbar\omega_\mathrm{L} = \frac{e\hbar}{m_0} B = g\mu_\mathrm{B} B, \tag{3.2}$$

where e is the elementary charge, m_0 the mass of the electron, $\hbar$ the reduced Planck's constant [64, p. 798], $\mu_\mathrm{B} = \frac{e\hbar}{2m_0}$ is the Bohr magneton and g is the Landé factor of the particle [64, p. 1073].

The Larmor frequency can be expressed by (see equation (3.2))

$$\omega_\mathrm{L} = \frac{\Delta E}{\hbar} = \frac{g\mu_\mathrm{B}}{\hbar} B. \tag{3.3}$$

The Larmor precession describes the time evolution of the spin in a magnetic field, with the precession frequency directly derived from the Zeeman splitting. It is directly proportional to the Zeeman splitting ΔE. A larger Zeeman splitting corresponds to a higher Larmor precession frequency, meaning the spin precesses faster in a stronger magnetic field. The linear dependence ω_L of on B is used to extract the Landé g-factor experimentally by fitting the Larmor frequency as a function of magnetic field.

The band energy $E(k)$ in a real crystal is anisotropic. Therefore the effective mass m^* is anisotropic and a tensor that depends on the crystal orientation and can be calculated by [64, p. 268]

$$\frac{1}{m^*} = \frac{1}{\hbar^2} \frac{\partial^2 E}{\partial k_i \partial k_j}. \tag{3.4}$$

The g-factor in a semiconductor depends on the effective mass and the spin-orbit splitting energy and therefor the g-factor is anisotropic. For an electron in the conduction band follows [74]

$$g_\mathrm{e} = g_0 \left[1 - \left(\frac{m_0}{m_\mathrm{e}^*} - 1 \right) \frac{\Delta_\mathrm{so}}{3E_\mathrm{g} + 2\Delta_\mathrm{so}} \right] \tag{3.5}$$

with the free electron g-factor $g_0 \approx 2$.

3.3 Magneto-optical Kerr Effect

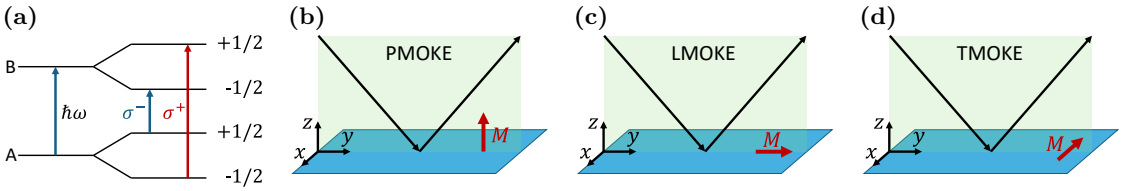

Figure 3.1: The selective absorption of left and right circularly polarized light $\sigma^{\pm}$ by a magnetic atom is shown Figure 3.1a [75, p. 597]. Figures 3.1b – 3.1d showing the three geometries of MOKE (PMOKE, LMOKE and TMOKE) [76, p. 20], with the green plane indicating the plane of light and the blue plane the sample surface plane. The light propagation direction is indicated with black arrows and the direction of magnetization M with red arrows.

Magneto-optical phenomena can be divided into two main categories: the photomagnetic effect, in which a magnetic property of a material is changed by optical excitation, and the magneto-optical effect, in which the optical properties of a material are changed by magnetic influences. The latter will be discussed below.

Magneto-optical effects include phenomena such as the Faraday effect, in which the plane of a linear polarized light transmitted through a material is rotated in accordance with the direction of magnetization, and the magneto-optical Kerr effect (MOKE), in which the plane of a linear polarized light reflected from a material undergoes a similar rotation in accordance with the direction of magnetization.

In the case of the Faraday effect, the rotation angle of the polarization plane θ, is directly proportional to the path of light in the material l, and the magnetic field H applied to the material. This relationship is expressed mathematically as follows

$$\theta = VlH \tag{3.6}$$

where V represents the Verdet constant. The angle of rotation remains invariant with respect to the direction of propagation of the light. This invariance is due to the fact that the phenomenon is caused by the different absorption of two oppositely circularly polarized light beams components, a consequence of spin precession, which is independent of the direction of propagation of the light.

The mechanism of the phenomenon is shown in Figure 3.1a. A magnetic atom at an energy level A that absorbs a photon of energy $\hbar\omega$ and passes to the level B. If the atomic spin is 1/2, each energy level splits into two sublevels $S = -1/2$ and $S = +1/2$, under the influence of a magnetic field H due to Zeeman splitting. Transitions between these levels, which are determined by spectroscopic selection rules, correspond either to $S = +1/2$ at the level A to $S = -1/2$ at the level B or $S = -1/2$ at the level A to $S = +1/2$ at the level B. This selection rule reflects the conservation of angular momentum, since the absorption of circularly polarized light carrying angular momentum requires a corresponding change in the spin angular momentum of the atom.

When a magnetic atom is magnetized, the distribution of the population between the two spin states on the plane A becomes unequal. The refractive index for left and right circularly polarized light becomes different and leads to the observed rotation of the plane of polarization.

The mechanism underlying the magneto-optical Kerr effect is similar to that of the Faraday effect and can differed in three geometries (see Figures 3.1b – 3.1d). When incident light is reflected from the surface of a material that is magnetized perpendicular to the surface ($M \parallel z$) or with a magnetization in light incidence and surface plane ($M \parallel y$), the plane of polarization is rotated during penetration into the skin depth and subsequent reflection. This results in a non-zero rotation of the plane of polarization and is called polar magneto-optical Kerr effect (PMOKE) and longitudinal magneto-optical Kerr effect (LMOKE). The third geometry differs in that the magnetization is perpendicular to the plane of incidence ($M \parallel x$), which leads to the transverse magneto-optical Kerr effect (TMOKE) with change only in the intensity of the reflected light, but no rotation of the polarization. [75, p. 596–597] [76, p. 17–18] [77, p. 137–147]

3.4 Spin Polarization in Magnetic Field

3.4.1 Hanle Effect

The Hanle effect describes the decreasing spin polarization degree excited under polarized light by rising magnetic field, which is applied perpendicular to the spin direction. [78]

The observed effect results from the precession of the electron spins around the direction of the applied magnetic field. With continuous illumination, this precession leads to a reduction in the average projection of the electron spin along the direction of observation. This projection determines the degree of circular polarization of the luminescence. Consequently, the degree of polarization decreases as a function of the transverse magnetic field. By measuring this dependence under stationary conditions, both the spin relaxation time and the recombination time can be determined.

This phenomenon is described by the precession of the electron spins in a magnetic field $\vec{B}$ with a Larmor frequency $\vec{\Omega}$. The dynamics of this precession, together with spin pumping, spin relaxation and recombination, is determined by the following equation of motion for the average spin vector $\vec{S}$:

$$\frac{d\vec{S}}{dt} = \vec{\Omega} \times \vec{S} - \frac{\vec{S}}{\tau_\mathrm{s}} - \frac{\vec{S} - \vec{S}_0}{\tau}\,, \tag{3.7}$$

where the first term on the right-hand side describes the Larmor spin precession in the magnetic field $\vec{\Omega} = \frac{g\mu_\mathrm{B}}{\hbar}\vec{B}$ (see Equation (3.3)). The second term represents the spin relaxation, where τ_s spin relaxation time, and the third term takes the generation of spin by optical excitation $\vec{S}_0/\tau$ and recombination $-\vec{S}/\tau$ into account where τ is the lifetime of the electron. The vector $\vec{S}_0$ is aligned along the direction of the exciting light beam, and its absolute value corresponds to the initial average spin of the electrons generated by light.

In the steady state $d\vec{S}/dt = 0$ and in the absence of a magnetic field $B = 0$, the spin projection along the z-axis is given by:

$$S_z(0) = \frac{S_0}{1 + \tau/\tau_\mathrm{s}}\,, \tag{3.8}$$

where $S_z(0)$ represents the projection of the spin vector along the direction of S_0 in the z-axis. Since $S_z(0)$ is equivalent to the degree of polarization of the luminescence (as discussed in Section 2.5), this expression corresponds to the formula for P in Equation (2.20).

If a transverse magnetic field is applied to S_0, the spin projection along the z-axis becomes

$$S_z(B) = \frac{S_z(0)}{1 + (\Omega T_\mathrm{s})^2} \tag{3.9}$$

with

$$\frac{1}{T_\mathrm{s}} = \frac{1}{\tau} + \frac{1}{\tau_\mathrm{s}} \tag{3.10}$$

where T_s represents the spin lifetime and defines the width of the depolarization curve with the half-width of the Hanle curve

$$B_{1/2} = \frac{\hbar}{\mu_\mathrm{B} g T_\mathrm{s}} \,. \tag{3.11}$$

As a result of the Hanle effect, the spin projection S_z and consequently the degree of circular polarization of the luminescence decreases as a function of the transverse magnetic field.

By combining measurements of the zero-field polarization value $P = S_z(0)$ with the magnetic field dependence obtained from the Hanle effect, the electron lifetime τ and the spin relaxation time τ_s under stationary conditions can be extracted if the g-factor is known. It follows for the electron lifetime [64, p. 1365–1367]

$$\tau = \frac{S_0}{S_z(B=0)} \frac{\hbar}{g \mu_\mathrm{B} B_{1/2}} \tag{3.12}$$

and for the spin relaxation time

$$\tau_\mathrm{s} = \frac{S_0}{S_0 - S_z(B=0)} \frac{\hbar}{g \mu_\mathrm{B} B_{1/2}} \,. \tag{3.13}$$

When polarized electrons are generated by a short optical pulse, time-resolved measurements show a damped spin precession around the magnetic field direction. This behavior is described by Equation (3.7) for a given initial spin value and provides a direct observation of spin dynamics. [42, p. 26]

The dynamics of the polarization is described by an oscillating decay in transverse magnetic fields and given by [28]:

$$P(t) = P_0 \cos(\Omega t) \exp\left(-\frac{t}{\tau_\mathrm{s}}\right) \tag{3.14}$$

The steady-state polarization degree in a longitudinal magnetic field is described by a Boltzmann statistic with the equation for Zeeman energy splitting (3.2) [79, 80, 81]

$$P_\mathrm{steady} = \tanh\left(\frac{\Delta E}{2 k_\mathrm{B} T}\right) \tag{3.15}$$

$$= \tanh\left(\frac{g \mu_\mathrm{B} B}{2 k_\mathrm{B} T}\right) \tag{3.16}$$

and it follows for free carriers with Equation (3.16) in (2.20), where the polarization is proportional to the spin density in (3.8):

$$P = \frac{\tau_\mathrm{s}}{\tau_\mathrm{s} + \tau} \tanh\left(\frac{g \mu_\mathrm{B} B}{2 k_\mathrm{B} T}\right) \tag{3.17}$$

3.4.2 Polarization Recovery Effect

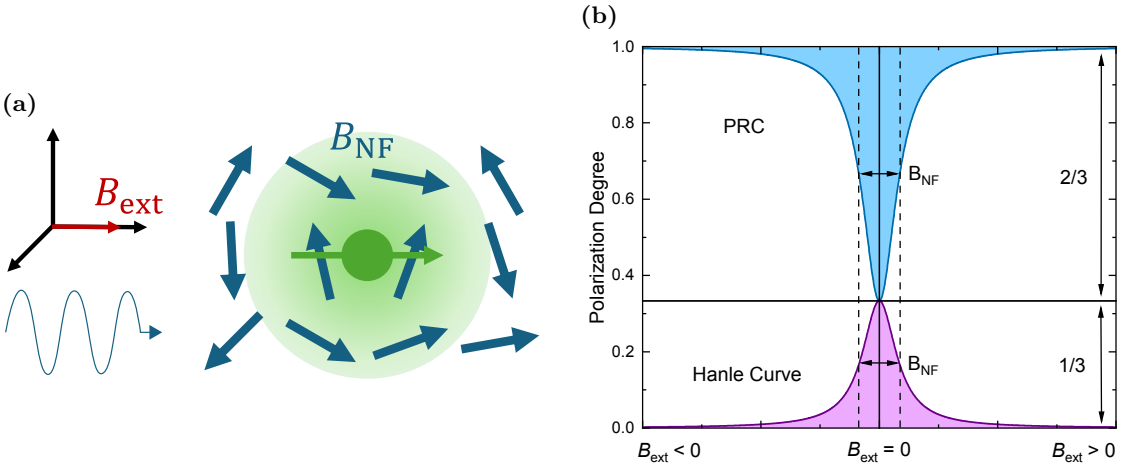

Figure 3.2: Principle of polarization recovery effect. Figure 3.2a The carrier spin (green) is surrounded by randomly oriented nuclear spins (blue), which result in a nuclear fluctuation spin field (B_{NF}). By applying an external magnetic field B_{ext} in Faraday geometry along the direction of light propagation (blue wave), the effective spin field can be overcome. Figure 3.2b shows a polarization recovery curve (PRC) (Faraday geometry, blue curve) and Hanle curve (Voigt geometry, violet curve) in an external magnetic field. The PRC and Hanle curve have an intercept at $B_{\mathrm{ext}} = 0$. The vertically dashed lines indicates the half-width at half-maximum of both curves. The polarization is $1/3$ at zero magnetic field for same carrier spin and nuclear spin direction and reaches 1 at higher external magnetic fields for the PRC and 0 for the Hanle curve. [82] [83, p. 16f]

The carrier spins are aligned along the direction of propagation of the light when polarized by circularly polarized light. The average spin of nuclei is not zero (static fluctuation). Due to hyperfine interaction there is an effective magnetic field acting on electrons which is proportional to the average nuclei spin. The carrier spins interact with the nuclear magnetic field even in the absence of an external magnetic field (B_{ext}). The nuclear magnetic field is randomly oriented, either parallel or perpendicular to the orientation of the carrier spins. The perpendicular component causes a precessional motion of the spins, which leads to a mixing of the spin-up and spin-down eigenstates.

If an external magnetic field is applied along the direction of the carrier spins (Faraday geometry), and is much larger than the effective nuclear field due to fluctuations ($B_{\mathrm{ext}} \gg B_{\mathrm{NF}}$), the carrier spins can align with their eigenstates. On average, of the total nuclear spin fluctuations, about one third of the spins are aligned parallel and two thirds perpendicular to the carrier spin. The polarization of the carrier spins with an applied external magnetic field is therefore three times as large as the maximum polarization that can be achieved by the nuclear spin fluctuations alone. [84]

This polarization behavior is mapped in the polarization recovery curve (PRC). A PRC is observed when the external magnetic field is increased or decreased in the Faraday geometry, with a dip occurring at $B_{\mathrm{ext}} = 0$. A simple PRC has the form of a Lorentz curve, but can have several Lorentz curves in complex systems. The schematic representation of the PRC and Hanle curve can be seen in Figure 3.2. [82]

3.5 Single Beam Pump-Probe of Spin Dynamics

One of the most widely used techniques for determining the spin relaxation times of both photoexcited and resident charge carriers in semiconductors is the Hanle effect. This phenomenon is characterized by the depolarization of photoluminescence when a transverse magnetic field is applied [42] (see Section 3.4.1). In its simplest form, the depolarization curve is described by a Lorentz profile with a half-width at half-maximum $B_{1/2} = \hbar/(g\mu_B T_s)$, where $\hbar$ denotes the reduced Planck constant, g the Landé factor of the spin-polarized charge carriers (e.g. conduction band electrons or valence electrons), μ_B is the Bohr magneton and T_s is the spin lifetime. The spin lifetime T_s is determined by the spin relaxation time τ_s and the charge carrier lifetime τ as $T_s^{-1} = \tau^{-1} + \tau_s^{-1}$. The exact determination of the spin lifetime from the Hanle curve requires precise knowledge of the g-factor.

Optical control of spin states and deeper insights into the associated dynamics can be achieved by time-resolved techniques such as Faraday or Kerr rotation with pump-probe [85, 86]. These methods utilize pulsed laser sources arranged in a pump-probe configuration to resolve the pump-induced spin dynamics over time and extract key parameters, including the g-factor and the spin relaxation time [42, 87]. Of particular interest is the range in which the spin lifetime exceeds the pulse spacing of the laser source. Under such conditions, resonant spin amplification occurs when the Larmor precession frequency $\omega_L = g\mu_B B/\hbar$ is a multiple of $2\pi f$, where f is the laser pulse repetition rate and B is the external magnetic field strength [88, 89, 90, 91, 92, 93]. Time-resolved pump-probe Faraday or Kerr rotation measurements require a complex optical setup that includes precise alignment of the two laser beams, a mechanical delay line and polarization-sensitive detection.

An alternative method for studying spin dynamics in semiconductors is based on optical resonance pumping of resident electrons. Specifically, a single laser beam tuned in resonance with the transition of the charged exciton (trion) in a semiconductor quantum well is used to spin-pump resident electrons in their ground state. The absorption of the same laser beam is used to monitor the electron spin polarization. If an external magnetic field is applied in the Voigt geometry, a depolarization of the electron spin occurs, which enables the observation of the Hanle effect.

Hanle peaks are not limited to $B = 0$, but also occur with magnetic fields that fulfill the resonance condition $\omega_L = 2\pi n f$, where n is an integer. This occurs when a pulsed laser source with a high repetition rate ($f \gg \tau_s^{-1}$) is used. These observations are interpreted as optical pumping in the rotating frame, where the frequency of the rotation corresponds to f or its higher harmonics. [94]

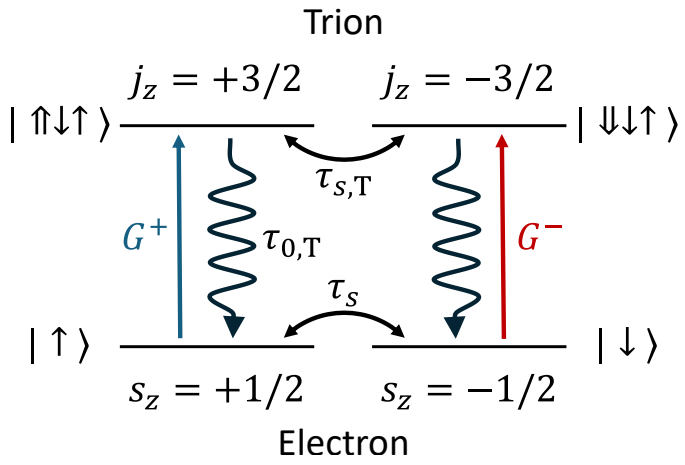

Figure 3.3: Energy level diagram with optical transitions for localized trions (T) in a CdTe/(Cd,Mg)Te quantum well structure, with indicated spin pumping $G^{\pm}$, trion lifetime $\tau_{0,\mathrm{T}}$ and trion relaxation time $\tau_{\mathrm{s,T}}$, and the spin relaxation time of resident electrons τ_{s} for the spin projection $\pm 1/2$. [94]

The energy level structure and the possible optical transitions between the levels in a CdTe/(Cd,Mg)Te quantum well structure are shown in Figure 3.3. The ground state consists of a doublet, which is characterized by an electron spin $s = 1/2$. The optically excited trion complex is formed by two electrons and a hole. The negatively charged exciton (X^-) in the singlet state consists of two conduction band electrons with antiparallel spins, resulting in a total spin $s = 0$, and a hole with angular momentum projections $j_z = \pm 3/2$. The z-axis is defined by the boundary axis of the quantum well (QW), which coincides with the growth direction of the structure and is parallel to the light propagation direction.

The generation of trions by resonant excitation is determined by the polarization of the light and the spin polarization of the resident electron ensemble. The selective excitation of spin-up electrons $|\uparrow\rangle$ is achieved by pumping with σ^+-polarized photons. The excited spin-up trion state X^- $|\Uparrow\uparrow\downarrow\rangle$ either decays radiatively through the same channel or, after a hole spin-flip process to $|\Downarrow\uparrow\downarrow\rangle$, by emitting a σ^--polarized photon. This latter process generates spin-down electrons $|\downarrow\rangle$. Consequently, the repeated resonant excitation of trions with σ^+-polarized light leads to a non-equilibrium state characterized by a larger population of spin-down electrons compared to spin-up electrons, a phenomenon known as optical pumping.

As a result of optical pumping, the light absorption decreases because the electron population in the ground state with spin projection $+1/2$ decreases under σ^+-polarized excitation. This reduction in the electron population lowers the trion excitation rate. Therefore, the spin polarization of the resident electrons can be studied by the decreasing of the trion absorption, which manifests itself in an increase in the intensity of the transmitted light. [95]

In the presence of an external magnetic field $\vec{B}$ aligned along the x-axis, the equation of motion for the spin density of the resident electrons $\vec{S}$, is expressed as follows

$$\frac{d\vec{S}}{dt} = \vec{G} - \frac{\vec{S}}{\tau_{\mathrm{s}}} + \vec{\Omega} \times \vec{S}, \tag{3.18}$$

where $\vec{G} = (0, 0, G)$ represents the spin pump term, τ_{s} denotes the spin relaxation time of the resident electrons and $\vec{\Omega} = (\omega_{\mathrm{L}}, 0, 0)$ characterizes the Larmor precession of $\vec{S}$ around

the external magnetic field [96, 97].

The spin pump term $\vec{G}$ depends on the helicity of the pump light:

$$G = -\frac{n_\mathrm{e}\rho_\mathrm{c}\tilde{G}}{2}\frac{\tau_{0,\mathrm{T}}}{\tau_{0,\mathrm{T}}+\tau_{\mathrm{s,T}}}, \tag{3.19}$$

where n_e is the electron density in the conduction band of the QW,

$$\tilde{G} = \frac{G^+ + G^-}{2} \tag{3.20}$$

is the optical generation rate, which is proportional to the laser intensity I, and

$$\rho_\mathrm{c} = \frac{G^+ - G^-}{G^+ + G^-} \tag{3.21}$$

is the circular degree of polarization of the exciting light. The parameters $\tau_{0,\mathrm{T}}$ and $\tau_{\mathrm{s,T}}$ represent the trion lifetime and the trion spin relaxation time, respectively, while G^+ and G^- correspond to the contributions of the σ^+ and σ^- polarized light components. Equation (3.18) is valid for low pump rates $G\tau_\mathrm{s} \ll n_\mathrm{e}/2$, which ensures a small spin polarization without saturation effects [97]. In addition, the condition $\tau_\mathrm{s} \gg \tau_{0,\mathrm{T}}, \tau_{\mathrm{s,T}}$ is assumed. This criterion is fulfilled for CdTe/(Cd,Mg)Te quantum well structure, for which $\tau_{0,\mathrm{T}} = 50\,\mathrm{ps}$ and $\tau_{\mathrm{s,T}} = 1000\,\mathrm{ps}$ [89, 98].

Under the conditions of low pump rates, the trion population remains significantly smaller than the ground state population, and the light absorption is expressed as

$$A \propto \left(\frac{n_\mathrm{e}}{2} + \rho_\mathrm{c} S_z\right) I. \tag{3.22}$$

The second term on the right-hand side of the Equation (3.22) takes into account the spin-dependent absorption caused by optical pumping. For σ^+-polarized light ($\rho_\mathrm{c} > 0$) optical pumping leads to negative spin polarization ($S_z < 0$), while σ^- excitation ($\rho_\mathrm{c} < 0$) leads to $S_z > 0$. With circularly polarized light, the transmitted intensity therefore increases due to absorption bleaching, while with linearly polarized excitation ($S_z = 0$) the transmitted intensity reaches a minimum. It should be noted that the transmission fluctuations depend on the degree of circular polarization of the incident laser light, but are independent of the sign of the polarization. The difference in intensity, ΔT between circularly ($\rho_\mathrm{c} = \pm 1$) and linearly polarized ($\rho_\mathrm{c} = 0$) light is given by

$$\Delta T \propto |S_z| I. \tag{3.23}$$

The steady-state solution of the Equation (3.18) with continuous wave excitation is described by the Hanle curve

$$S_{z0} = \frac{P\tau_\mathrm{s}}{1+\omega_\mathrm{L}^2\tau_\mathrm{s}^2}. \tag{3.24}$$

With pulsed laser excitation, the excitation rate is time-dependent

$$G(t) = G_0 \sum_{-\infty}^{+\infty} \exp\left(i2\pi n f t\right), \tag{3.25}$$

where G_0 is proportional to the time-integrated laser intensity I. Using the Equation (3.18), the stationary solution is obtained as follows

$$\frac{\Delta T}{I} \propto \sum_{-\infty}^{+\infty} |S_{zn}|, \tag{3.26}$$

where S_{z0}, given by the Equation (3.24), represents the Hanle curve around $B = 0$, and higher harmonics ($|n| > 0$) correspond to the optical pumping of resident electron spins in the rotating frame

$$S_{zn} = \frac{1}{2} S_{z0} \left(\omega_\mathrm{L} - 2\pi n f\right). \tag{3.27}$$

The factor 1/2 in Equation (3.27) results from the fact that the harmonic excitation signal is expressed as the sum of two oppositely rotating components with half the amplitude. In the rotating frame, only one component contributes to the solution of the steady state. The harmonics with $n \neq 0$ correspond to Hanle effect cloning, where the Larmor precession frequency ω_L is replaced by $\omega_\mathrm{L} - 2\pi n f$ in Equation (3.24). [94]

3.6 Evolution of Spin Density of Resident Electrons

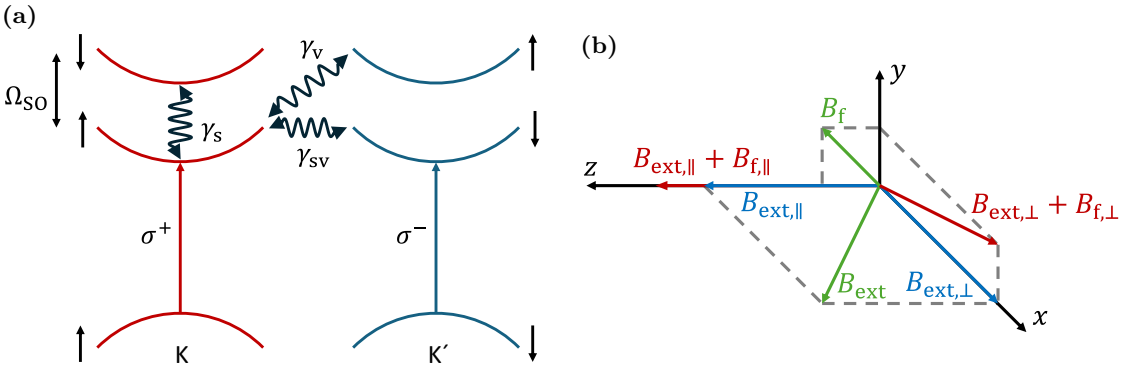

Figure 3.4: Figure 3.4a Scheme of energy states and intervalley scattering in the K and K′ valley in a $MoSe_2$ monolayer. Indicated are the magnitude of spin-orbit splitting Ω_{SO}, spin conserving intervalley scattering rate γ_v, spin relaxation rate within the same valley γ_s, and intervalley spin relaxation rate γ_{sv}. Figure 3.4b The external magnetic field B_{ext} is applied in the xz-plane at an angle α relative to the z-axis. B_f is the random fluctuation field. Red arrows indicate longitudinal ($\parallel$) and transverse ($\perp$) components of the total magnetic field acting on the electrons.

The dynamic of the spin density of the resident electron spins $\vec{S}$ can be described with the Bloch equations [97] for low pumping rates $G/\gamma \ll n_e/2$

$$\frac{d\vec{S}}{dt} = \vec{G} + \vec{\Omega} \times \vec{S} - \gamma \cdot \vec{S} \tag{3.28}$$

with the pumping term $\vec{G}$, the Larmor frequency $\vec{\Omega}$ and the spin relaxation rate γ.

The pumping term $\vec{G} = (0, 0, G)$ describes the creation of spins in excited states by pumping. The second term in Equation (3.28) is the cross product between the Larmor

frequency and spin orientation and describes the dynamics of the spin. Spin pumping of the resident electrons is achieved by exciting the trions with circularly polarized light. Due to the spin relaxation in the trion state, the repeated excitation of spin-polarized trions leads to a dynamic polarization of the resident charge carriers [94, 96] Since $E_\mathrm{F} < \Omega_\mathrm{SO}$, only resident electrons in the lowest energy states K $\uparrow$ and K$'$ $\downarrow$ are considered, which are doubly degenerate at $B = 0$.

The intervalley spin relaxation is then determined by $\gamma = \gamma_\mathrm{sv}$, with the assumption that it is anisotropic and following applies $\gamma_\perp = \gamma_x = \gamma_y$ and $\gamma_\parallel = \gamma_z$.

By considering the polarization recovery and Hanle effect, the effective magnetic field B_f fluctuating from one electron to an other is introduced and thereby leading to additional depolarization of the signal, even in zero external magnetic field.

Also the anisotropic electron g-factor g_i is taken into account which results in Larmor precession frequency components $\Omega_i = g_i \Omega_0$, where $\Omega_0 = \mu_\mathrm{B} B_\mathrm{ext}$ with μ_B being the Bohr magneton and $i = x, y, z$ the direction of the magnetic field.

In this case it is a contact spin interaction, which requires electron localization [99].

3.6.1 Steady-State Solution of the Spin Density of Resident Electrons

The Equation (3.28) has to be separated and solved for the steady-state solution. The calculation of the second term with solving the cross product gives

$$\begin{pmatrix} \Omega_x \\ \Omega_y \\ \Omega_z \end{pmatrix} \times \begin{pmatrix} S_x \\ S_y \\ S_z \end{pmatrix} = \begin{pmatrix} \Omega_y S_z - \Omega_z S_y \\ \Omega_z S_x - \Omega_x S_z \\ \Omega_x S_y - \Omega_y S_x \end{pmatrix} \tag{3.29}$$

Assuming a xz-plane with an applied magnetic field in horizontal direction, the y-direction can be neglected.

The third term of the equation can be extended written as:

$$\gamma \cdot \vec{S} = \begin{pmatrix} \gamma_\perp & 0 & 0 \\ 0 & \gamma_\perp & 0 \\ 0 & 0 & \gamma_\parallel \end{pmatrix} \cdot \begin{pmatrix} S_x \\ S_y \\ S_z \end{pmatrix} \tag{3.30}$$

Thus separation of Equation (3.28) with the pumping term and Equations (3.29) and (3.30) leads to

$$\frac{dS_x}{dt} = \Omega_y S_z - \Omega_z S_y - \gamma_\perp S_x \tag{3.31}$$

$$\frac{dS_y}{dt} = \Omega_z S_x - \Omega_x S_z - \gamma_\perp S_y \tag{3.32}$$

$$\frac{dS_z}{dt} = G + \Omega_x S_y - \Omega_y S_x - \gamma_\parallel S_z \tag{3.33}$$

for the xyz-direction components of the spin density. In case of steady-state $^{d\vec{S}}/_{dt} = 0$ and $\Omega_y = 0$ the separated but depending equation are following:

$$S_x = -\frac{\Omega_z S_y}{\gamma_\perp} \tag{3.34}$$

$$S_y = \frac{\Omega_z S_x - \Omega_x S_z}{\gamma_\perp} \tag{3.35}$$

$$S_z = \frac{G + \Omega_x S_y}{\gamma_\parallel} \tag{3.36}$$

With the Equation (3.34) for S_x in (3.35) follows an independent S_y from S_x:

$$S_y = -\frac{\Omega_x S_z \gamma_\perp}{\gamma_\perp^2 + \Omega_z^2} \tag{3.37}$$

With Equation (3.37) for S_y in (3.36), and consideration of the anisotropy with $\gamma_\perp = \gamma_x = \gamma_y$ and $\gamma_\parallel = \gamma_z$ follows the independent steady-state solution for S_z in absence of fluctuation fields B_f:

$$\boxed{S_z = \frac{G}{\gamma_\parallel} \frac{\Omega_z^2 + \gamma_\perp^2}{\Omega_z^2 + \frac{\gamma_\perp}{\gamma_\parallel}\Omega_x^2 + \gamma_\perp^2}} \tag{3.38}$$

3.6.2 Steady-State Solution with Fluctuating Magnetic Fields

The initial polarization at zero external magnetic field $B_\mathrm{ext} = 0\,\mathrm{T}$ can be explained by fluctuation fields B_f that leads to an effective magnetic field $B = B_\mathrm{ext} + B_\mathrm{f}$ (see Figure 3.4b) that interact with the electron spin. In this case the Larmor precession has the form $\Omega_i = g_i \Omega_0 + bI_i$ with the applied magnetic field direction in the indices $i = x, y, z$, the Larmor precession in magnetic field $\Omega_0 = \mu_\mathrm{B} B$ and the interaction with the fluctuating spin I with the strength of interaction b. With this and due to radial symmetry in the sample plane, that corespondents to a rotation around the z-axis, the Larmor precession can be transformed in $\Omega_z^2 \to (\Omega_z + bI_z)^2$ and $\Omega_x^2 \to (\Omega_x + bI_x)^2 + (bI_y)^2$. With this substitution in Equation (3.38) follows

$$S_z = \frac{G}{\gamma_\parallel} \frac{(\Omega_z + bI_z)^2 + \gamma_\perp^2}{(\Omega_z + bI_z)^2 + \frac{\gamma_\perp}{\gamma_\parallel}\left((\Omega_x + bI_x)^2 + (bI_y)^2\right) + \gamma_\perp^2}\,. \tag{3.39}$$

The magnitude and direction of the fluctuating field are randomly distributed, which can be captured by a Gaussian distribution function [84]. In this case the magnitude of S_z can be obtained only numerically. For this reason a simplified approach is used where averaging should result in vanishing of the terms linear to $\langle I_i \rangle = 0$ and the second order terms are replaced by the mean-square value $\langle I_i^2 \rangle = \frac{1}{3} I_0^2$ [100].

With this assumptions follows the steady-state solution for S_z with fluctuating magnetic fields

$$\boxed{S_z = \frac{G}{\gamma_\parallel} \frac{\Omega_z^2 + \frac{1}{3}(bI_0)^2 + \gamma_\perp^2}{\Omega_z^2 + \frac{\gamma_\perp}{\gamma_\parallel}\Omega_x^2 + \left(\frac{1}{3} + \frac{2}{3}\frac{\gamma_\perp}{\gamma_\parallel}\right)(bI_0)^2 + \gamma_\perp^2}} \tag{3.40}$$

3.6.3 Angular Dependence of Spin Density

The angular dependence of the relative spin density follows with consideration of the anisotropy $\Omega_x = g_x \Omega_0 \sin(\alpha)$ and $\Omega_z = g_z \Omega_0 \cos(\alpha)$
for $\alpha \neq 0$

$$S_z(\alpha) = \frac{G}{\gamma_\parallel} \frac{\Omega_0^2 g_z^2 \cos^2(\alpha) + \frac{1}{3}(bI_0)^2 + \gamma_\perp^2}{\Omega_0^2 g_z^2 \cos^2(\alpha) + \frac{\gamma_\perp}{\gamma_\parallel}\Omega_0^2 g_x^2 \sin^2(\alpha) + \left(\frac{1}{3} + \frac{2}{3}\frac{\gamma_\perp}{\gamma_\parallel}\right)(bI_0)^2 + \gamma_\perp^2} \tag{3.41}$$

and for $\alpha = 0$

$$S_z(0) = \frac{G}{\gamma_\parallel} \frac{\Omega_0^2 g_z^2 + \frac{1}{3}(bI_0)^2 + \gamma_\perp^2}{\Omega_0^2 g_z^2 + \left(\frac{1}{3} + \frac{2}{3}\frac{\gamma_\perp}{\gamma_\parallel}\right)(bI_0)^2 + \gamma_\perp^2} \tag{3.42}$$

In case of large external magnetic fields B_{ext} is $\Omega_0^2 \gg \gamma_\perp^2 (bI_0)^2$ all terms without Ω_0^2 are negligible and thus the equation is independent from fluctuation fields. From this follows for Equations (3.41) and (3.42):

$$S_z(\alpha) = \frac{G}{\gamma_\parallel} \frac{\Omega_0^2 g_z^2 \cos^2(\alpha)}{\Omega_0^2 g_z^2 \cos^2(\alpha) + \frac{\gamma_\perp}{\gamma_\parallel} \Omega_0^2 g_x^2 \sin^2(\alpha)} \tag{3.43}$$

$$S_z(0) = \frac{G}{\gamma_\parallel} \tag{3.44}$$

The angular dependence of relative spin density can be defined by

$$A(\alpha) = \frac{S_z(\alpha)}{S_z(0)} \tag{3.45}$$

with Equations (3.43) and (3.44) in (3.45) follows

$$A(\alpha) = \frac{\Omega_0^2 g_z^2 \cos^2(\alpha)}{\Omega_0^2 g_z^2 \cos^2(\alpha) + \frac{\gamma_\perp}{\gamma_\parallel} \Omega_0^2 g_x^2 \sin^2(\alpha)} \tag{3.46}$$

$$= \frac{\Omega_0^2 \cos^2(\alpha) g_z^2}{\Omega_0^2 \cos^2(\alpha) \frac{\gamma_\perp}{\gamma_\parallel} g_x^2 \left(\frac{\gamma_\parallel}{\gamma_\perp} \frac{g_z^2}{g_x^2} + \frac{\sin^2(\alpha)}{\cos^2(\alpha)} \right)} \tag{3.47}$$

$$= \frac{\frac{\gamma_\parallel}{\gamma_\perp} \frac{g_z^2}{g_x^2}}{\frac{\gamma_\parallel}{\gamma_\perp} \frac{g_z^2}{g_x^2} + \tan^2(\alpha)} \,. \tag{3.48}$$

With a definition of a ratio for anisotropy

$$a^2 = \frac{\gamma_\parallel g_z^2}{\gamma_\perp g_x^2} \tag{3.49}$$

in Equation (3.48) follows the angular dependence of relative spin density amplitude equation

$$\boxed{A(\alpha) = \frac{a^2}{a^2 + \tan^2(\alpha)}} \tag{3.50}$$

This evaluation was previously used to determine the anisotropy of the g-factor of localized electrons in a GaAs/AlGaAs quantum well structure [31] and does not depend on the distribution of the fluctuating fields.

3.6.4 Estimation of the Anisotropy in HWHM

In Figure 3.5 are the schematic curves for a Hanle effect (red curve) and polarization recovery (blue curve) shown. The shape for Hanle effect for magnetic fields applied in x-direction follows with the condition $\Omega_z = 0$ and $\Omega_x \neq 0$ in Equation (3.40)

$$S_{z,\text{V}} = \frac{G}{\gamma_\parallel} \frac{\frac{1}{3}(bI_0)^2 + \gamma_\perp^2}{\frac{\gamma_\perp}{\gamma_\parallel} \Omega_x^2 + \left(\frac{1}{3} + \frac{2}{3} \frac{\gamma_\perp}{\gamma_\parallel} \right) (bI_0)^2 + \gamma_\perp^2} \tag{3.51}$$

and for PRC with magnetic fields applied in z-direction $\Omega_z \neq 0$ and $\Omega_x = 0$

$$S_{z,\text{F}} = \frac{G}{\gamma_\parallel} \frac{\Omega_z^2 + \frac{1}{3}(bI_0)^2 + \gamma_\perp^2}{\Omega_z^2 + \left(\frac{1}{3} + \frac{2}{3} \frac{\gamma_\perp}{\gamma_\parallel} \right) (bI_0)^2 + \gamma_\perp^2} \,. \tag{3.52}$$

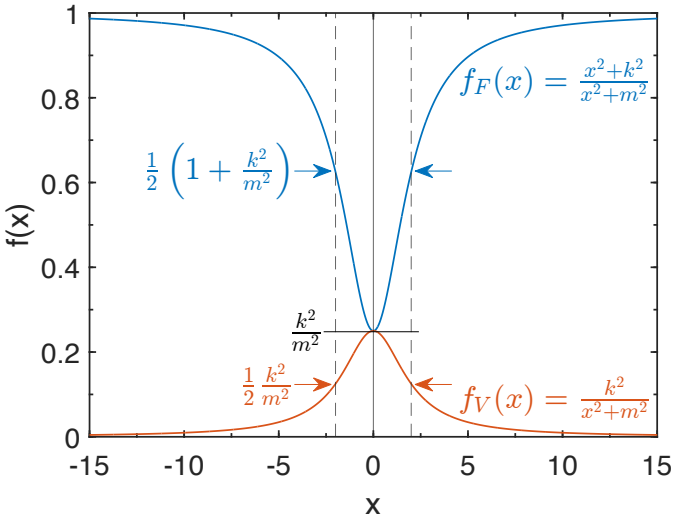

Figure 3.5: Schematic curves of Hanle effect (red curve, function indicated as V for Voigt) and polarization recovery (blue curve, Faraday F) with example parameter $k = 1$ and $m = 2$ showing the half-width at half-maximum for both curves and cutting point at $f(0) = {}^{k^2}/_{m^2}$. The vertically dashed lines indicates the position $x_{1/2} = m$ of the HWHM that is equivalent to an applied external magnetic field B and the function $f_{\mathrm{F,V}}(x)$ are the polarization degree in dependence of the magnetic field $P_{\mathrm{F,V}}(B)$.

The terms in both Equations (3.51) and (3.52) can be defined as

$$k^2 = \frac{1}{3}(bI_0)^2 + \gamma_\perp^2 \tag{3.53}$$

$$m^2 = \left(\frac{1}{3} + \frac{2}{3}\frac{\gamma_\perp}{\gamma_\parallel}\right)(bI_0)^2 + \gamma_\perp^2 \tag{3.54}$$

$$x_{\mathrm{F}}^2 = \Omega_z^2 \tag{3.55}$$

$$x_{\mathrm{V}}^2 = \frac{\gamma_\perp}{\gamma_\parallel}\Omega_x^2 \tag{3.56}$$

to describe the simple shape of the steady-state solution for S_z in Voigt (V) and Faraday (F) geometry.

It follows for Hanle curve

$$f(x) = \frac{k^2}{x^2 + m^2} \tag{3.57}$$

where $f(0) = \frac{k^2}{m^2}$ is the amplitude of the Hanle curve and $f_{1/2} = \frac{1}{2}\frac{k^2}{m^2}$ the half-maximum of the amplitude. The simplified function describes the polarization in dependence of the magnetic field $f(x) = P(B)$. The position $x_{1/2}$ of the half-amplitude describes the half-width at half-maximum (HWHM) and can be calculated with

$$f(x) = f_{1/2} \tag{3.58}$$

$$\Rightarrow \frac{k^2}{x^2 + m^2} = \frac{1}{2}\frac{k^2}{m^2} \tag{3.59}$$

with solving the equation to x follows the HWHM $x_{1/2}$

$$x^2 = m^2 \tag{3.60}$$

$$\Rightarrow x_{1/2} = \pm m\,. \tag{3.61}$$

With the definition for x_{V} and m above follows the HWHM in Voigt geometry

$$\sqrt{\frac{\gamma_\perp}{\gamma_\parallel}}\Omega_x = \sqrt{\left(\frac{1}{3}+\frac{2}{3}\frac{\gamma_\perp}{\gamma_\parallel}\right)(bI_0)^2+\gamma_\perp^2} \tag{3.62}$$

$$\boxed{\sqrt{\frac{\gamma_\perp}{\gamma_\parallel}}g_x\Omega_0 = \sqrt{\left(\frac{1}{3}+\frac{2}{3}\frac{\gamma_\perp}{\gamma_\parallel}\right)(bI_0)^2+\gamma_\perp^2}}\,. \tag{3.63}$$

The simplified function of the Faraday geometry has the form

$$f(x) = \frac{x^2+k^2}{x^2+m^2} \tag{3.64}$$

with the amplitude

$$f(0) = 1-\frac{k^2}{m^2} \tag{3.65}$$

and its half-maximum

$$f_{1/2} = \frac{k^2}{m^2}+\frac{1}{2}\left(1-\frac{k^2}{m^2}\right) = \frac{1}{2}\left(1+\frac{k^2}{m^2}\right)\,. \tag{3.66}$$

Thus the position $x_{1/2}$ of the half-maximum is calculated with

$$f(x) = f_{1/2} \tag{3.67}$$

$$\frac{x^2+k^2}{x^2+m^2} = \frac{1}{2}\left(1+\frac{k^2}{m^2}\right) \tag{3.68}$$

with simplifying and solving for x follows

$$\begin{aligned} x^2-\frac{k^2}{2m^2}-\frac{x^2}{2} &= \frac{m^2}{2}+\frac{k^2}{2}-k^2 \\ x^2 &= \frac{\left(m^2-k^2\right)m^2}{m^2-k^2} \\ x^2 &= m^2 \\ \Rightarrow x_{1/2} &= \pm m\,. \end{aligned} \tag{3.69}$$

With the definition for x_{F} and m above follows the HWHM in Faraday geometry

$$\Omega_z = \sqrt{\left(\frac{1}{3}+\frac{2}{3}\frac{\gamma_\perp}{\gamma_\parallel}\right)(bI_0)^2+\gamma_\perp^2} \tag{3.70}$$

$$\boxed{g_z\Omega_0 = \sqrt{\left(\frac{1}{3}+\frac{2}{3}\frac{\gamma_\perp}{\gamma_\parallel}\right)(bI_0)^2+\gamma_\perp^2}}\,. \tag{3.71}$$

Equating the Equations (3.63) and (3.71) leads to

$$g_z\Omega_0^{\mathrm{F}} = \sqrt{\frac{\gamma_\perp}{\gamma_\parallel}}g_x\Omega_0^{\mathrm{V}} = \sqrt{\left(\frac{1}{3}+\frac{2}{3}\frac{\gamma_\perp}{\gamma_\parallel}\right)(bI_0)^2+\gamma_\perp^2} \tag{3.72}$$

$$\boxed{\Omega_0^{\mathrm{F}} = \sqrt{\frac{\gamma_\perp}{\gamma_\parallel}}\frac{g_x}{g_z}\Omega_0^{\mathrm{V}} = \frac{1}{g_z}\sqrt{\left(\frac{1}{3}+\frac{2}{3}\frac{\gamma_\perp}{\gamma_\parallel}\right)(bI_0)^2+\gamma_\perp^2}}\,. \tag{3.73}$$

The ratio $\sqrt{\frac{\gamma_\perp}{\gamma_\parallel}}\frac{g_x}{g_z} = a$ from Equation (3.49) can be evaluated experimentally in the limit of large fields using Equation (3.50).

3.7 Long-Range Magnetic Proximity Effect in Semiconductor Hybrid Structure

3.7.1 Principle of the Long-Range Proximity Effect

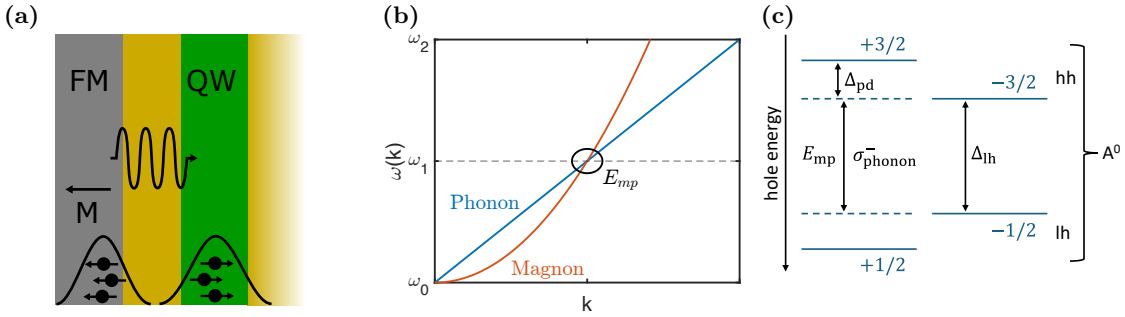

Figure 3.6: Scheme of the long-range proximity effect principle. Figure 3.6a shows the schematic drawing of a sample with Cobalt (Co) FM, CdTe QW and CdMgTe barrier between that the wave function can not overlap. The proximity effect is mediated by chiral phonons. Figure 3.6b shows dispersion relation of a phonon and a magnon in a FM material with a linear and quadratic behavior, respectively. At the intercept is the resonance that leads to coupling between magnon and TA phonons. The phonons get elliptically polarized due to strong spin-phonon interaction. [101] Figure 3.6c shows the energy state of acceptor-bound hole (A^0) with splitting in light hole lh and heavy hole hh. At the right spin side ($-1/2 \leftrightarrow -3/2$) the energy gap is Δ_{lh} and the energy is close to magnon-phonon energy E_{mp}. At the left spin side ($+1/2 \leftrightarrow +3/2$) the coupling with phonons leads to repelling of the levels resulting in splitting Δ_{pd}.

The magnetic proximity effect is the interaction between the spin systems of a magnetic layer and quantum well in a hybrid semiconductor structure. By bringing them close, there is an overlap of the wave function of the magnetic layer and QW and a dynamic and steady state effect can occur. This can be due to spin depending tunneling [7] and exchange interaction that leads to splitting and build up of steady state polarization if the splitting Δ is comparable or larger than thermal energy $k_{\mathrm{B}}T$ [8, 4]. With a barrier large enough between the magnetic and quantum well layer the wave function does not overlap and a direct interaction is not possible (Figure 3.6a).

In Reference [9] it was demonstrated that another type of indirect exchange interaction induced by interaction with elliptically polarized phonons may take place. The long-range proximity effect was demonstrated in structure Co-CdMgTe/CdTe where the p-electrons of the QW and d-acceptor bound holes from the magnetic layer have an indirect exchange interaction. The chiral phonons (elliptically polarized) originate from the FM layer where the interaction is mediated by chiral phonons that is possible at the intercept in the dispersion relation of the magnon and phonon (Figure 3.6b). [101] The dispersion relation for the phonon is linear ($\omega(k) \propto k$) and for the magnon is quadratic ($\omega(k) \propto k^2$). The non-zero resonance point of the magnon and phonon have the energy $E_{\mathrm{mp}} = \hbar\omega_1 \approx 1\,\mathrm{meV}$. Such phonons have no barrier and easily penetrate into the non-magnetic semiconductor

part of the structure and reach the QW layer. Here the hole bound to acceptor have a resonance energy, where the state is split that corresponds to splitting between the heavy and light hole states.

Figure 3.6c shows the energy states of the acceptor bound hole for $+1/2 \leftrightarrow +3/2$ spins at the left side and $-1/2 \leftrightarrow -3/2$ spins at the right side. The energy states are split in hh and lh with an energy gap Δ_{lh} for the spins at the right side. This energy is close to the magnon-phonon interaction energy E_{mp}. At the left spin side ($+1/2 \leftrightarrow +3/2$) spin-orbit interaction leads to spin dependent coupling of holes with circular polarized phonons. As the result splitting with Δ_{pd} occurs which is an equivalent of optical AC Stark effect. The magnitude of Δ_{pd} was shown to be in the range from 50 µeV to 100 µeV which corresponds to effective magnetic field of 1–2 T [9, 14]. The splitting Δ_{pd} to the magnon-phonon energy that correspondents to interaction energy and can be detected by the polarization of the photoluminescence. [102]

Low voltage control of proximity effect was demonstrated in [12] and structures with Fe-based hybrid structures were studied in [9]. However no studies with dielectric FM and TMD monolayer hybrid structure were investigated.

3.7.2 Recombination-Induced Spin Orientation of Electrons

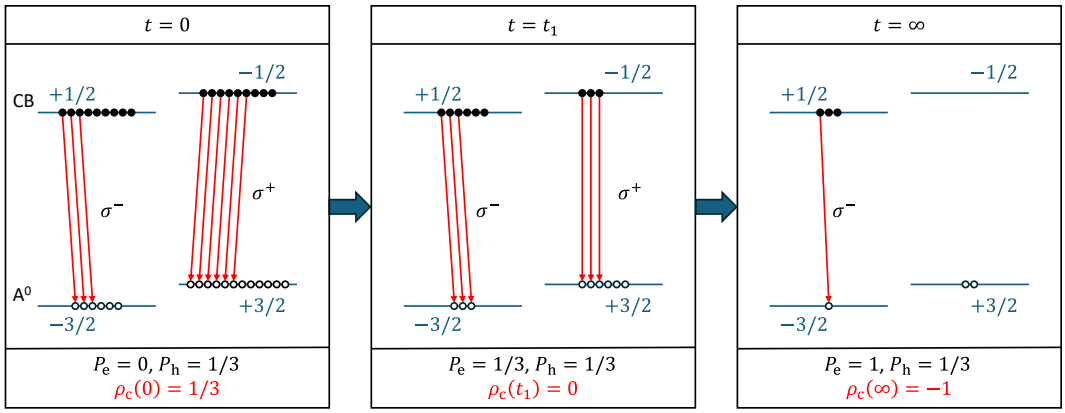

Figure 3.7: Schematic illustration of the recombination-induced spin orientation of electrons in electron-hole representation. The holes bound to acceptors (A^0) are independent of the time and have a steady-state polarization ($P_h = 1/3$ in this example). The spin relaxation of the electron in the conduction band (CB) is neglected. The red arrows show the recombination of the electron with holes, that initiates the next illustrated step.

The dynamics of proximity effect in time-resolved photoluminescence (TRPL) allows to obtain important information about the magnitude of the splitting and types of carriers, e.g. hole or electrons which are getting spin polarized. Same concerns optical orientation in CdTe/CdMgTe QW. Therefore spin dynamics of carriers play important role. Here the degree of circular polarization of PL as function of time under unpolarized (or linear polarized) excitation is considered which is relevant for interpretation of spin dynamics in hybrid structures. The effect is absent at $B = 0$ thus the situation in case of Zeeman split levels is considered. This can be due to external field or effective exchange field originating from magnetized FM layer in hybrid structure.

In Figure 3.7 the qualitative explanation of the dynamical polarization of electrons after excitation with polarized (or unpolarized) laser pulse is illustrated in three steps

from left to right. By neglecting the spin relaxation of the electrons the polarization of the electrons is due to recombination with spin polarized holes. Immediately after excitation ($t = 0$) the electrons and holes are unpolarized. The photoluminescence (PL) polarization begins to increase due to spin relaxation of the holes at the level with lower hole energy (i.e. $+3/2$) and the level with angular momentum $+3/2$ is predominantly populated. If the hole spin relaxation is fast enough then steady state population for holes is achieved which depends on the magnetic field B and thermal energy $k_\mathrm{B}T$. In this figure the hole polarization is set to $P_\mathrm{h} = 1/3$ (note it can be different and depends on temperature and magnetic field) and the PL polarization reaches a maximum value of $\rho_\mathrm{c} = P_\mathrm{h} > 0$. The middle Figure 3.7 shows the recombination at time $t = t_1$. The electron state with spin projection $-1/2$ decays faster than the $+1/2$ state, and a non-equilibrium spin orientation of the electrons occurs. The electron spin is oriented along the hole spin, and the electron polarization P_e increases with time. It is screening the hole polarization, so that $P_\mathrm{e} = P_\mathrm{h}$ and the PL polarization is zero. The right Figure 3.7 shows the temporal evolution for infinite times $t = \infty$. The electron polarization keeps accumulating and saturates at $P_\mathrm{e} = 1$. It does not depend on the value of the hole spin polarization in case it is non-zero. The PL polarization changes sign and saturates at $\rho_\mathrm{c} = -1$. In this simplified model, the sign change of ρ_c occurs at time $t_1 \approx \tau_0$, and the characteristic time of saturation τ_0/P_h, with the instantaneous lifetime τ_0 of the photoexcited electrons. Thus the hole polarization P_h determines the speed of the occurring saturation, and the characteristic time of saturation is longer for lower P_h.

For the quantitative description of the dynamics of spin orientation the case of non-exponential bimolecular recombination is considered, that is typical for intrinsic (undoped) semiconductors. By neglecting the spin relaxation the recombination-induced orientation of electrons can be described by the equation

$$\frac{dn_{\pm 1/2}}{dt} = \frac{G}{2} - C p_{\mp 3/2} n_{\pm 1/2} \tag{3.74}$$

with the densities of electrons $n_{\pm 1/2}$ with spin projection $\pm 1/2$, the densities of holes $p_{\pm 3/2}$ with angular momentum projection $\pm 3/2$ on the QW confinement axis (z-axis), the coefficient of bimolecular recombination C and generation rate of electrons G. For pulsed excitation $G = 0$ and $n(t = 0) = n_0$ can be assumed. With taking care about the circularly polarized components $\sigma^\pm$ of the PL intensity follows

$$I_{\sigma^\pm} = C p_{\pm 3/2} n_{\mp 1/2} \tag{3.75}$$

The total densities n (for electrons) and p (for holes) and their respective spin polarizations P_e and P_h are defined as follows:

$$n = n_{+1/2} + n_{-1/2} \tag{3.76}$$

$$p = p_{+3/2} + p_{-3/2} \tag{3.77}$$

and

$$P_\mathrm{e} = \frac{n_{+1/2} - n_{-1/2}}{n_{+1/2} + n_{-1/2}} \tag{3.78}$$

$$P_\mathrm{h} = \frac{p_{+3/2} - p_{-3/2}}{p_{+3/2} + p_{-3/2}}\,. \tag{3.79}$$

By solving the Equation (3.76) for $n_{+1/2} = n - n_{-1/2}$ and $n_{-1/2} = n - n_{+1/2}$ in Equation (3.78) and solving the Equation (3.77) for $p_{+3/2} = p - p_{-3/2}$ and $p_{-3/2} = p - p_{+3/2}$ in Equation (3.79), the following expressions are obtained:

$$n_{\pm 1/2} = \frac{n}{2}(1 \pm P_\mathrm{e})\,, \tag{3.80}$$

$$p_{\pm 3/2} = \frac{p}{2}(1 \pm P_\mathrm{h})\,. \tag{3.81}$$

The total intensity of photoluminescence (PL) I and the degree of circular polarization ρ_c are given by:

$$I = I_{\sigma^+} + I_{\sigma^-} \tag{3.82}$$

$$= \frac{Cp}{2} n(1 - P_\mathrm{e}P_\mathrm{h}) \tag{3.83}$$

$$\rho_\mathrm{c} = \frac{I_{\sigma^+} - I_{\sigma^-}}{I_{\sigma^+} + I_{\sigma^-}} \tag{3.84}$$

$$= \frac{P_\mathrm{h} - P_\mathrm{e}}{1 - P_\mathrm{e}P_\mathrm{h}} \tag{3.85}$$

As shown in Figure 3.7, a collection of holes in the $+3/2$ state leads to σ^+-polarized PL, while electrons in the $+1/2$ state contribute to σ^--polarized PL. Therefore, the polarizations in Equation (3.85) are subtracted to reflect these opposite contributions.

The kinetic Equation (3.74), expressed in terms of carrier densities and spin polarizations, is as follows:

$$\frac{dn}{dt} = G - \frac{Cp}{2} n(1 - P_\mathrm{e}P_\mathrm{h})\,, \tag{3.86}$$

$$\frac{d(nP_\mathrm{e})}{dt} = \frac{Cp}{2} n(P_\mathrm{h} - P_\mathrm{e})\,. \tag{3.87}$$

In the following analysis, the fact that the holes quickly reach a stationary state with a polarization of

$$P_\mathrm{h} = -\frac{g_\mathrm{A}\mu_\mathrm{B}B}{2k_\mathrm{B}T}\,, \tag{3.88}$$

is used, whereby this polarization is time-independent. This reflects the short relaxation time of the hole spin τ_sh compared to the characteristic recombination time. Consequently, the kinetics are considered at time delays $t > \tau_\mathrm{sh}$ after excitation.

The initial conditions for the electron polarization and density are defined as $P_\mathrm{e}(t = 0) = 0$ and $n(t = 0) = n_0$. Since a non-exponential decay of the PL intensity is considered in this recombination-induced orientation scenario, no time-independent lifetime can be introduced. Therefore, the density kinetics of both electrons and holes must be taken into account.

In the simplest case, in which there are no traps, the condition of quasi-neutrality applies, so that $n(t) = p(t)$. The following expressions for the electron density and polarization can be derived from the basic Equations (3.86) and (3.87):

$$\frac{dn}{dt} = -\frac{Cn^2(t)}{2}(1 - P_\mathrm{e}P_\mathrm{h})\,, \tag{3.89}$$

$$\frac{dP_\mathrm{e}}{dt} = \frac{Cn(t)}{2} P_\mathrm{h}(1 - P_\mathrm{e}^2)\,. \tag{3.90}$$

The Equations (3.89) and (3.90) are strongly non-linear. In particular, the term $(1 - P_e^2)$ acts as a limiting factor that prevents an unlimited growth of the electron spin polarization.

The solution of the Equations (3.89) and (3.90) for the condition $P_e P_h \ll 1$ and with initial conditions $P_e(t = 0) = 0$ and $n(t = 0) = n_0$ is given by

$$n(t) = \frac{n_0}{1 + \frac{t}{\tau_0}}, \tag{3.91}$$

$$P_e(t) = \frac{\left(1 + \frac{t}{\tau_0}\right)^{P_h} - \left(1 + \frac{t}{\tau_0}\right)^{-P_h}}{\left(1 + \frac{t}{\tau_0}\right)^{P_h} + \left(1 + \frac{t}{\tau_0}\right)^{-P_h}}. \tag{3.92}$$

Here the time constant $\tau_0 = 2/(Cn_0)$ is introduced, which represents the instantaneous lifetime of the electrons at the time of excitation. With this solution, the expressions for the PL intensity and its polarization become

$$I(t) = \frac{Cn^2(t)}{2} = \frac{n_0}{\tau_0} \frac{1}{\left(1 + \frac{t}{\tau_0}\right)^2}, \tag{3.93}$$

$$\rho_c = P_h - P_e(t) \tag{3.94}$$

$$= P_h - \frac{\left(1 + \frac{t}{\tau_0}\right)^{P_h} - \left(1 + \frac{t}{\tau_0}\right)^{-P_h}}{\left(1 + \frac{t}{\tau_0}\right)^{P_h} + \left(1 + \frac{t}{\tau_0}\right)^{-P_h}}. \tag{3.95}$$

For small P_h (i.e. $P_h \ll 1$) the polarization ρ_c reverses the sign with a delay time $t_1 \approx (e - 1)\tau_0$, whereby the intensity decreases by a factor of ten. The linear range in which the spin relaxation of the electrons remains small ($P_e^2 \ll 1$) is now to be investigated.

The equation for the electron density $n(t) = \frac{n_0}{1+\frac{t}{\tau_0}}$ remains unchanged, while the polarization develops as follows

$$\frac{dP_e}{dt} = \frac{Cn(t)}{2} P_h - \frac{P_e - P_e^{eq}}{\tau_{se}}, \tag{3.96}$$

with the initial condition $P_e(0) = 0$. Here $P_e^{eq} = -g_e \mu_B B/(2k_B T)$ is the thermal equilibrium spin polarization of electrons and τ_{se} the spin relaxation time of electrons. The degree of polarization is then expressed as

$$\rho_c(t) = P_h - P_e^{eq}\left(1 - \exp\left(-\frac{t}{\tau_{se}}\right)\right) - \tilde{P}_h \exp\left(-\frac{t}{\tau_{se}}\right) \int_0^{\frac{t}{\tau_{se}}} \frac{e^x}{x + \alpha}\, dx, \tag{3.97}$$

where the parameter $\alpha = \frac{\tau_0}{\tau_{se}} = \frac{2}{Cn_0\tau_{se}}$ represents the ratio of the electron spin relaxation time to the electron lifetime at the moment of excitation and $\tilde{P}_h$ is the recombination-induced dynamic spin polarization.

The physical meaning of the Equation (3.97) is as follows: The first two terms describe the dynamics without recombination-induced orientation and indicate that spin relaxation dominates under the condition $\alpha = \frac{\tau_0}{\tau_{se}} \gg 1$.

The last term in the Equation (3.97) results from the recombination-related orientation of the electrons and becomes significant when $\alpha \leq 1$. This form of the equation reflects the fact that the instantaneous lifetime of the electrons $\tau(t) = \frac{2}{Cn(t)}$ is not constant due to time-dependent recombination with photoexcited holes. In contrast to a p-type semiconductor, where the lifetime is usually constant, it varies with time.

At the beginning, this last term is zero, since the electrons are unpolarized at $t = 0$. It also approaches zero when $t \to \infty$, where the instantaneous electron lifetime diverges ($\tau(t) \to \infty$), and spin relaxation begins to dominate. For intermediate times this term becomes particularly significant.

For delay times that are shorter than the initial instantaneous lifetime ($t \ll \tau_0$), the Equation (3.97) can be approximated in linear form:

$$\rho_c(t) = P_h - \frac{t}{\tau_{se}} \left(P_e^{eq} + \frac{\tilde{P}_h}{\alpha} \right) . \tag{3.98}$$

The Equation (3.98) must be applied with caution, as the spin relaxation of the holes must also be taken into account for time delays ($t \leq \tau_{sh}$).

3.8 Dynamics of Exciton and Carrier Spin Precession in Magnetic Field in Perovskites

The top valence and bottom conduction bands in lead halide perovskite semiconductors are two-fold spin-degenerate and can be described using spin-$\frac{1}{2}$ operators (see Figure 2.1b). This property leads to unique exciton spin dynamics in an external magnetic field, which is determined by the interplay between the exchange interaction and the Zeeman splitting of individual charge carriers. The Hamiltonian describing an electron-hole pair in perovskites with cubic symmetry under an external magnetic field B is given by

$$\hat{H} = \mu_B g_e \hat{s}_e B + \mu_B g_h \hat{s}_h B + \Delta_{\text{exch,e-h}} \hat{s}_e \cdot \hat{s}_h, \tag{3.99}$$

where μ_B is the Bohr magneton, B is the external magnetic field, and $\Delta_{\text{exch,e-h}}$ denotes the electron-hole exchange splitting. The spin operators of the electron and hole are represented by $\hat{s}_e$ and $\hat{s}_h$, respectively. The exchange interaction in the cubic symmetry can be expressed as $\hat{s}_e \cdot \hat{s}_h = \frac{1}{2}\hat{J}^2 - \frac{3}{4}$, where $\hat{J} = \hat{s}_e + \hat{s}_h$ is the total spin operator of the electron-hole pair, and $\hat{J}^2 = J(J+1)$. The total spin quantum number J can assume values of either 0 or 1.

The eigenstates of the exchange interaction Hamiltonian are chosen in the form $|J, J_z\rangle$ and given by

$$\phi_1 = |1, +1\rangle = |\uparrow, \Uparrow\rangle, \tag{3.100}$$

$$\phi_2 = |1, 0\rangle = \frac{1}{\sqrt{2}}(|\uparrow, \Downarrow\rangle + |\downarrow, \Uparrow\rangle), \tag{3.101}$$

$$\phi_3 = |1, -1\rangle = |\downarrow, \Downarrow\rangle, \tag{3.102}$$

$$\phi_4 = |0, 0\rangle = \frac{1}{\sqrt{2}}(|\uparrow, \Downarrow\rangle - |\downarrow, \Uparrow\rangle). \tag{3.103}$$

Here, the symbols $\uparrow$ and $\Uparrow$ represent the electron and hole spins, respectively, where the up and down arrows denote spin projections of $+\frac{1}{2}$ and $-\frac{1}{2}$. In the following discussion the z-axis is chosen to align with the wave vector k of the incident light.

At $B = 0$, the eigenstates consist of the spin singlet state ($J = 0$) with energy $-\frac{3}{4}\Delta_{\text{exch,e-h}}$ and the spin triplet states ($J = 1$) with energy $\frac{1}{4}\Delta_{\text{exch,e-h}}$, resulting in a splitting of $\Delta_{\text{exch,e-h}}$ between these states. The states with $J_z = \pm 1$ (ϕ_1 and ϕ_3) are optically active in $\sigma^{\pm}$ circular polarizations. The exciton state $|1, 0\rangle$ possesses a dipole moment along the z-axis (referred to as the "longitudinal" exciton) and remains optically inactive in this geometry. The state $|0, 0\rangle$ is optically dark due to spin selection rules.

In the presence of a magnetic field, states with the same total spin projection along the field direction undergo mixing, while states with different total spin components experience Zeeman splitting. Specifically, in the Voigt geometry, where $B = (B_\mathrm{V}, 0, 0) \parallel x$, the Hamiltonian in Equation (3.99) takes the form

$$\hat{H} = \frac{1}{2\sqrt{2}} \begin{pmatrix} 2\sqrt{2}\Delta_{\text{exch,e-h}} & \mu_\mathrm{B} g_{\mathrm{V,X}} B_\mathrm{V} & 0 & -\mu_\mathrm{B} g_{\mathrm{V,DX}} B_\mathrm{V} \\ \mu_\mathrm{B} g_{\mathrm{V,X}} B_\mathrm{V} & 2\sqrt{2}\Delta_{\text{exch,e-h}} & \mu_\mathrm{B} g_{\mathrm{V,X}} B_\mathrm{V} & 0 \\ 0 & \mu_\mathrm{B} g_{\mathrm{V,X}} B_\mathrm{V} & 2\sqrt{2}\Delta_{\text{exch,e-h}} & \mu_\mathrm{B} g_{\mathrm{V,DX}} B_\mathrm{V} \\ -\mu_\mathrm{B} g_{\mathrm{V,DX}} B_\mathrm{V} & 0 & \mu_\mathrm{B} g_{\mathrm{V,DX}} B_\mathrm{V} & 0 \end{pmatrix}, \tag{3.104}$$

where $g_{\mathrm{V,X}} = g_{\mathrm{V,e}} + g_{\mathrm{V,h}}$ is the so-called bright exciton g-factor, and $g_{\mathrm{V,DX}} = g_{\mathrm{V,e}} - g_{\mathrm{V,h}}$ is the dark exciton g-factor.

In the Voigt geometry all excitonic states become optically active. For general cases the notations of the bright and dark exciton g-factors are used in analogy with the Faraday geometry. The Larmor frequency of the bright exciton is given by $\omega_{\mathrm{L,X}} = \frac{\mu_\mathrm{B} g_{\mathrm{V,X}} B_\mathrm{V}}{\hbar}$.

The energies of the exciton states in the presence of the magnetic field are given by

$$E_\mathrm{I} = \frac{1}{2}\left(\Delta_{\text{exch,e-h}} - \sqrt{\Delta^2_{\text{exch,e-h}} + (\mu_\mathrm{B} g_{\mathrm{V,DX}} B_\mathrm{V})^2}\right), \tag{3.105}$$

$$E_\mathrm{II} = \frac{1}{2}\left(\Delta_{\text{exch,e-h}} + \sqrt{\Delta^2_{\text{exch,e-h}} + (\mu_\mathrm{B} g_{\mathrm{V,DX}} B_\mathrm{V})^2}\right), \tag{3.106}$$

$$E_\mathrm{III} = \Delta_{\text{exch,e-h}} - \frac{1}{2}\mu_\mathrm{B} g_{\mathrm{V,X}} B_\mathrm{V}, \tag{3.107}$$

$$E_\mathrm{IV} = \Delta_{\text{exch,e-h}} + \frac{1}{2}\mu_\mathrm{B} g_{\mathrm{V,X}} B_\mathrm{V}. \tag{3.108}$$

The eigenfunctions can be conveniently expressed as superpositions of the basis states Equations (3.100)–(3.103) in the form

$$|i\rangle = \sum_j a_{i,j} \phi_j, \tag{3.109}$$

where the index $i = \mathrm{I}, \mathrm{II}, \mathrm{III}, \mathrm{IV}$ denotes the eigenstates in the presence of the magnetic field, and the subscript $j = 1, 2, 3, 4$ refers to the basis functions in Equations (3.100)–(3.103). The coefficients $a_{i,j}$ can be rewritten in column-vector form:

$$a_{\mathrm{I},j} = \begin{pmatrix} \frac{1}{2}\sqrt{1 - \Delta_{\text{exch,e-h}}/C} \\ 0 \\ -\frac{1}{2}\sqrt{1 - \Delta_{\text{exch,e-h}}/C} \\ \frac{\mu_\mathrm{B} g_{\mathrm{V,DX}} B_\mathrm{V}}{\sqrt{2C(C - \Delta_{\text{exch,e-h}})}} \end{pmatrix}, \qquad a_{\mathrm{II},j} = \begin{pmatrix} -\frac{1}{2}\sqrt{1 + \Delta_{\text{exch,e-h}}/C} \\ 0 \\ \frac{1}{2}\sqrt{1 + \Delta_{\text{exch,e-h}}/C} \\ \frac{\mu_\mathrm{B} g_{\mathrm{V,DX}} B_\mathrm{V}}{\sqrt{2C(C + \Delta_{\text{exch,e-h}})}} \end{pmatrix} \tag{3.110}$$

$$a_{\mathrm{III},j} = \begin{pmatrix} \frac{1}{2} \\ -\frac{\sqrt{2}}{2} \\ \frac{1}{2} \\ 0 \end{pmatrix}, \qquad a_{\mathrm{IV},j} = \begin{pmatrix} \frac{1}{2} \\ \frac{\sqrt{2}}{2} \\ \frac{1}{2} \\ 0 \end{pmatrix} \tag{3.111}$$

with $C = \sqrt{\Delta^2_{\text{exch,e-h}} + (\mu_\mathrm{B} g_{\mathrm{V,DX}} B_\mathrm{V})^2}$.

The dependence of the exciton energy levels on B_V is depicted in Figure 3.8a for the case of zero exchange interaction, $\Delta_{\text{exch,e-h}} = 0\,\mathrm{meV}$. In this scenario, a linear Zeeman splitting is observed for all four states. When a significant exchange interaction is present,

$\Delta_{\text{exch,e-h}} = 0.42\,\text{meV}$, states III and IV exhibit a linear-in-B_V Zeeman splitting, whereas states I and II show a linear splitting only at high magnetic fields, with an offset given by $\Delta_{\text{exch,e-h}}$ for $B_\text{V} \to 0$ (see Figure 3.8d).

To compute the time- and polarization-resolved photoluminescence (PL) intensity following polarized excitation by a short laser pulse, a coherent model is employed, neglecting both the finite exciton lifetime and spin relaxation processes. The wave function of the system $\Psi(t)$ is therefore expressed as a superposition of the eigenstates $|i\rangle$ from Equation (3.109):

$$\Psi(t) = \sum_{i=\text{I}}^{\text{IV}} C_i |i\rangle \exp(-i\omega_i t), \qquad \omega_i = E_i/\hbar. \tag{3.112}$$

The coefficients C_i are determined by the initial conditions. Excitation with circularly polarized light creates excitons in the ϕ_1 or ϕ_3 states, depending on photon helicity. The initial state $(\phi_1 - \phi_3)/\sqrt{2}$ corresponds to horizontal polarization along B_V, denoted as $\parallel$, while $(\phi_1 + \phi_3)/\sqrt{2}$ represents vertical polarization, denoted as $\perp$.

Similarly, the emission intensity in a given polarization is determined by the absolute value squared of the projection of $\Psi(t)$ onto the corresponding polarized state.

In the experiments, the intensities in the σ^+, σ^-, $\parallel$, and $\perp$ polarizations are measured after σ^+-polarized excitation and are given by:

$$I^{\sigma^+}_{\sigma^+} = \left| \sum_i a^2_{i,1} \exp(-i\omega_i t) \right|^2, \tag{3.113}$$

$$I^{\sigma^+}_{\sigma^-} = \left| \sum_i a_{i,1} a_{i,3} \exp(-i\omega_i t) \right|^2, \tag{3.114}$$

$$I^{\sigma^+}_{\parallel} = \left| \sum_i \left(a^2_{i,1} + a_{i,1} a_{i,3} \right) \exp(-i\omega_i t) \right|^2, \tag{3.115}$$

$$I^{\sigma^+}_{\perp} = \left| \sum_i \left(a^2_{i,1} - a_{i,1} a_{i,3} \right) \exp(-i\omega_i t) \right|^2. \tag{3.116}$$

In general, the calculated intensities presented in Figure 3.8 exhibit a complex oscillatory time dependence, which arises from the superposition of quantum beats with frequencies determined by Equations (3.105)–(3.108).

For the beats in circular polarization, simplified analytical expressions can be derived in the limit of negligible exchange interaction, $\Delta_{\text{exch,e-h}} \to 0$. In this case

$$I^{\sigma^+}_{\sigma^+} - I^{\sigma^+}_{\sigma^-} \propto \cos(\omega_{\text{L,e}} t) + \cos(\omega_{\text{L,h}} t), \tag{3.117}$$

where $\omega_{\text{L,e}}(h) = g_{\text{e(h)}} \mu_\text{B} B_\text{V}/\hbar$ denotes the Larmor precession frequencies of electrons and holes.

In the absence of exchange interaction ($\Delta_{\text{exch,e-h}} \to 0$), excitonic effects do not contribute, and the observed spin precessions correspond to those of electron and hole spins with the respective Larmor frequencies. This result is in agreement with the numerical data presented in Figure 3.8b. This situation can be observed in the case of the long-living time-resolved photoluminescence (TRPL) signal, which is attributed to unbound electrons and holes.

If the exchange splitting exceeds the Zeeman splitting, i.e., $\Delta_{\text{exch,e-h}} > \hbar\omega_{\text{L,X}}$, the signal of the singlet exciton state can be neglected. In this regime, the spin beats of the triplet states can be analyzed using the Zeeman Hamiltonian

$$H_3 = \frac{1}{2}\mu_{\text{B}} g_{\text{V,X}} B_{\text{V}} \hat{L}_x, \tag{3.118}$$

where $\hat{L}_x$ represents the matrix of the x-component of the angular momentum for a system with total angular momentum $J = 1$.

Under these conditions, the exciton pseudospin precesses with the frequency $\omega_{\text{L,X}}/2 = \mu_{\text{B}} g_{\text{V,X}} B_{\text{V}}/(2\hbar)$, leading to

$$I^{\sigma^+}_{\sigma^+} - I^{\sigma^+}_{\sigma^-} \propto \cos\left(\omega_{\text{L,X}} t/2\right), \tag{3.119}$$

which is consistent with the numerically computed beats shown in Figure 3.8e for weak magnetic fields.

For strong exchange splitting, the oscillation of $I^{\sigma^+}_{\sigma^+} - I^{\sigma^+}_{\sigma^-}$ occurs at half the Larmor frequency of the Zeeman splitting of the bright exciton, $\omega_{\text{L,X}}/2$.

Similarly, in the limit of weak exchange interaction, the beats in linear polarization are described by

$$I^{\sigma^+}_{\perp} \propto 1 + \cos\left[\left(\omega_{\text{L,e}} + \omega_{\text{L,h}}\right) t\right], \qquad I^{\sigma^+}_{\parallel} \propto 1 + \cos\left[\left(\omega_{\text{L,e}} - \omega_{\text{L,h}}\right) t\right]. \tag{3.120}$$

The vertically linearly polarized PL component oscillates with the Larmor frequency of the bright exciton, while the horizontally linearly polarized component oscillates with the Larmor frequency of the dark exciton. As a result, the signal $I^{\sigma^+}_{\perp} - I^{\sigma^+}_{\parallel}$ contains two oscillatory contributions at the frequencies $\omega_{\text{L,e}} + \omega_{\text{L,h}}$ and $\omega_{\text{L,e}} - \omega_{\text{L,h}}$, as shown in Figure 3.8c.

For strong exchange interaction, the analysis based on the Hamiltonian (3.118) leads to the beat pattern

$$I^{\sigma^+}_{\perp} \propto 0.5(1 + \cos\left[\omega_{\text{L,X}} t\right]), \qquad I^{\sigma^+}_{\parallel} \propto 1, \tag{3.121}$$

which agrees with the numerical calculations.

The expressions describing the temporal evolution of the intensities are derived within a fully coherent framework, neglecting exciton spin relaxation and population relaxation. These relaxation effects can be phenomenologically incorporated through exponential decay terms $\exp(-t/\tau_{\text{X}})$ for exciton recombination and $\exp(-t/\tau_{\text{s}})$ for spin relaxation.

The model presented above is applicable to both the fast dynamics of excitons with large exchange splitting and the dynamics of charge carriers with negligible exchange interaction. Exciton dynamics primarily occur on the exciton radiative lifetime scale, governed by exchange and Zeeman interactions. In contrast, the long-lived dynamics of electrons and holes are determined by the Zeeman splittings of the individual charge carriers. [72]

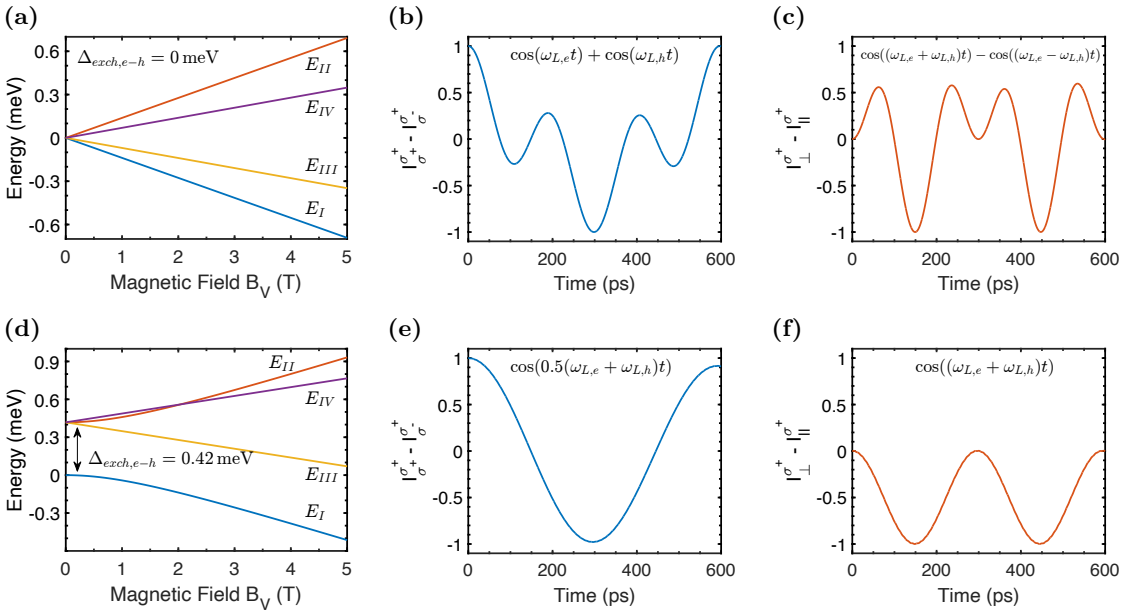

Figure 3.8: The Figures in the top row 3.8a, 3.8b and 3.8c are showing the calculated energy levels of the excitons as a function of the magnetic field B_V, the dynamics of $I^{\sigma^+}_{\sigma^+} - I^{\sigma^+}_{\sigma^-}$ and the dynamics of $I^{\sigma^+}_{\perp} - I^{\sigma^+}_{\parallel}$ for $\Delta_{\mathrm{exch,e\text{-}h}} = 0\,\mathrm{meV}$. The Figures in the bottom row 3.8a, 3.8b and 3.8c show the calculations for $\Delta_{\mathrm{exch,e\text{-}h}} = 0.42\,\mathrm{meV}$. The dynamics are calculated with $g_{\mathrm{e,V}} = +3.48$, $g_{\mathrm{h,V}} = -1.15$, $B_\mathrm{V} = 0.1\,\mathrm{T}$. [72]

Part II

Experimental Methods

4 Samples

This chapter is about the samples that are investigated in the experimental parts, and their composition and structures. The hybrid FM-semiconductor structures with magnetite and nickel ferrite used to study the proximity effect are described in Section 4.1.

The $MoSe_2$ monolayer TMD hybrid structure is described in Section 4.2 where EuS was expected to give FM effects to investigate the magnetic proximity but did not work and spin relaxation was studied.

Section 4.3 discusses the growing technique and some characteristics of the $FA_{0.9}Cs_{0.1}PbI_{2.8}Br_{0.2}$ crystal and $MAPbI_3$ microcrystal lead halide perovskite where the spin dynamics of excitons and charge carriers is investigated.

4.1 Hybrid Ferrimagnetic-Quantum Well Semiconductor Structures

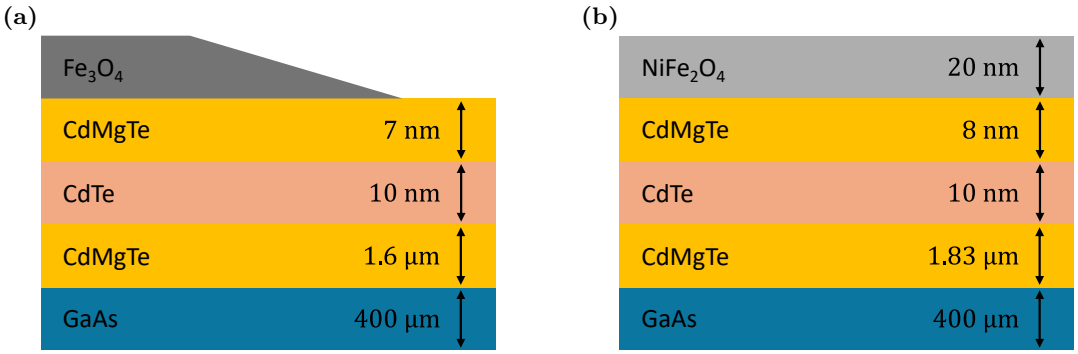

Figure 4.1: A schematic representation of hybrid semiconductor structures is given, illustrating two different configurations. The structure of the ferrimagnet hybrid sample with a gradient in the thickness of the magnetite (Fe_3O_4) layer is shown in Figure 4.1a, while the structure of the nickel ferrite ($NiFe_2O_4$) hybrid sample is shown in Figure 4.1b. Both sample designs share a common architecture, consisting of a GaAs substrate, a CdMgTe buffer layer, and a CdTe quantum well. In the first configuration, a gradient layer of Fe_3O_4 is deposited on top, while in the second configuration a $NiFe_2O_4$ layer is used instead.

In previous studies hybrid structures with Cobalt (Co) and Iron (Fe) as ferromagnetic top layer were used. Here different FM layers are investigated to extend the properties of long-range proximity and find its universal character. The schematic representation of the studied ferrimagnetic-semiconductor hybrid structures are shown in Figure 4.1 with magnetite (Fe_3O_4) in Figure 4.1a and nickel ferrite ($NiFe_2O_4$) in Figure 4.1b.

For the magnetite-based hybrid sample the semiconductor CdTe/(Cd,Mg)Te quantum well (QW) structure is grown by molecular beam epitaxy on a 400 µm semi-insulating GaAs (100) substrate. The QW comprises a 3 µm CdTe buffer layer, followed by an 1.6 µm $Cd_{0.6}Mg_{0.4}Te$ barrier, a 10 nm CdTe quantum well, and a 7 nm $Cd_{0.6}Mg_{0.4}Te$ cap.

To protect the structure from oxidation, a 20 nm protective Te layer is deposited on top and stored in a nitrogen atmosphere.

The protective Te layer is subsequently removed by annealing the sample at 200 °C for 20 min at a background pressure of $1 \cdot 10^{-6}$ mbar. The Fe_3O_4 film is grown on the structure using pulsed laser deposition at an oxygen pressure of $2 \cdot 10^{-6}$ mbar, with a laser fluence of 1.5 J/cm^2 and a laser repetition rate of 5 Hz. Ionized particles are generated from a rotating Fe_2O_3 target. The growth temperature is maintained at 300 °C, which is sufficient to form a single crystalline Fe_3O_4 phase without impacting the underlying semiconductor structure. [103, 104, 105, 106, 107]

During deposition, a shutter is used to cover one half of the sample. Positioned at a specific distance from the sample, the shutter creates a gradient in the magnetite film thickness, ranging from 0 nm (bare QW) to 15 nm over a distance of 1 cm in the direction perpendicular to the shutter edge. This results in regions of the structure with and without magnetite.

The nickel ferrite ($NiFe_2O_4$) hybrid-structure is analogous to the magnetite-based configuration described above. It comprises a 400 µm GaAs (100) substrate, an 1.83 µm (Cd,Mg)Te buffer layer, a 10 nm CdTe layer, and an 8 nm (Cd,Mg)Te cap. The structure is initially covered with a 35 nm thick protective Te layer and stored in a nitrogen atmosphere to prevent oxidation of the Te surface.

In the subsequent processing stage, the sample is annealed in a vacuum for 44 min at 260 °C to remove the protective Te layer. Following this, a 20 nm thick $NiFe_2O_4$ film is deposited by laser molecular beam epitaxy. The deposition is carried out in an Ar atmosphere at a pressure of $5 \cdot 10^{-3}$ mbar and a temperature of 260 °C by ablating a $NiFe_2O_4$ target.

4.2 Two-Dimensional van der Waals Monolayer Hybrid Structure

The sample under investigation consists of a monolayer of molybdenum diselenide ($MoSe_2$) deposited on a 10 nm Europium(II) sulfide (EuS) layer, which in turn is grown on a dielectric distributed Bragg reflector (DBR). The EuS layer is deposited by electron-beam evaporation onto a silicon dioxide (SiO_2) film that serves as the top layer of the DBR. The EuS film is ferromagnetic but there is no proximity effect. The carriers do not interact directly with the magnetization of FM. This happens possibly to the oxidation of EuS film at the surface. While the EuS film exhibit ferromagnetic behavior, but shows no direct interaction with the $MoSe_2$ monolayer, it acts as an electron donor to the $MoSe_2$ monolayer, providing a carrier density below $n_e \approx 10^{12}\,\mathrm{cm}^{-2}$. [19]

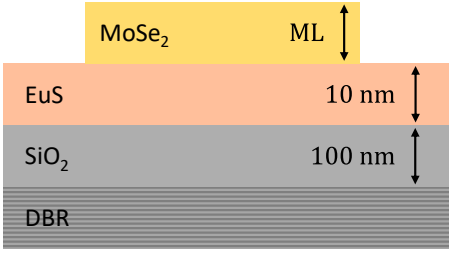

Figure 4.2: Schematic drawing of the TMD hybrid structure with the monolayer (ML) $MoSe_2$ on a 10 nm EuS layer grown on 100 nm SiO_2 as top layer on a DBR structure.

4.3 Lead Halide Perovskite Semiconductors

The basic principle for growing perovskite single crystals is based on the technique of inverse temperature crystallization (ITC). In this process, all the necessary reagents, such as a lead salt and an organic cation salt or a caesium salt are dissolved in a polar solvent such as γ-butyrolactone (GBL), an aprotic polar solvent. Once the reagents are completely dissolved, the resulting mixture, known as the precursor solution, is carefully filtered and transferred to a crystallization vessel.

The crystallization vessel is then heated in a water bath. As the temperature rises, the solubility of the precursors decreases, which leads to the precipitation of perovskite crystals. This temperature-induced precipitation occurs because the solubility product of the perovskite material is reduced at higher temperatures, which promotes crystal formation.

These adjustments will be discussed in detail in the subsequent sections, as referenced in [108, 109].

4.3.1 $FA_{0.9}Cs_{0.1}PbI_{2.8}Br_{0.2}$ Bulk Crystal

The growth process for α-phase $FA_{0.9}Cs_{0.1}PbI_{2.8}Br_{0.2}$ crystals is described in detail in Reference [108]. The procedure involves mixing all the required salts, such as CsI, FAI, PbI_2, and $PbBr_2$, as described previously. Cs and Br in small content were added in order to increase the stability of the crystal. Crystallization occurs at a temperature of 130 °C using the inverse temperature crystallization (ITC) technique.

The resulting crystals have a deep black color and a structure size of about 2 mm × 2 mm × 3 mm. Although the outer surfaces of the crystal have rhombic and trapezoidal shapes, the internal symmetry is cubic. The facets of the crystal are aligned along the inclined directions of the cubic unit cell, e.g. along the diagonal [110] direction.

4.3.2 $MAPbI_3$ Microcrystal

The inverse temperature crystallization (ITC) method was modified to facilitate the growth of $MAPbI_3$ single crystals. In this case, the precursor salts were dissolved in a mixture of γ-butyrolactone (GBL) with the addition of various alcohols. Specifically, the incorporation of 1-propanol, 1-butanol, 1-pentanol, or 1-hexanol enabled precise control over the solvent polarity, thereby reducing the crystallization temperature.

However, this modification comes with the potential drawback of increased dissolution time for the salts, although this effect was not thoroughly investigated. The crystallization of $MAPbI_3$ was successfully achieved at a lower temperature of 85 °C, in contrast to the typical higher temperatures required for such processes.

The resulting crystal morphology is similar to that of $FA_{0.9}Cs_{0.1}PbI_{2.8}Br_{0.2}$, with predominantly rhombic and trapezoidal facets. While $MAPbI_3$ exhibits a tetragonal phase at room temperature, it assumes a cubic phase at the crystallization temperature.

The studied $MAPbI_3$ single microcrystal was syntesized from the $MAPbI_3$ perovskite precursors that was injected between two polytetrafluoroethylene coated glasses and slowly heated to 120 °C. The measured $MAPbI_3$ is a single microcrystal with a tetragonal crystal structure at room temperature and out of plane tetragonal [001] axis. The sample has sizes of 2 mm × 2 mm × 0.02 mm. The geometry with the light wave vector $k \parallel [001]$ was used in all optical experiments.

5 Magneto-Optical Spectroscopy

This chapter gives an overview about the used magneto-optical spectroscopy techniques. The used setups are shown schematically and discussed. Most of the measurements in this thesis were performed with the polarization resolved photoluminescence spectroscopy described in Section 5.1. A pulsed laser with tunable wavelength and characterized beam in power and polarization with retarder and polarizer is used to excite the sample placed in a magneto-optical cryostat. The outcoming photoluminescence is collimated and characterized by retarder and polarizer before it is detected by a CCD or streak camera attached to a spectrometer. Thus spin dynamics of exciton and charge carriers can be investigated time-integrated and time-resolved. Additional the reflected laser beam from the sample can be detected with a photodiode for magneto-optical Kerr effect measurements and single beam pump-probe experiments. Section 5.2 presents the time resolution principle of a streak camera and how the axis are calibrated. In Section 5.3 the evaluation of MOKE is discussed. Further, the single beam optical technique is presented in Section 5.4.

5.1 Polarization Resolved Photoluminescence Spectroscopy

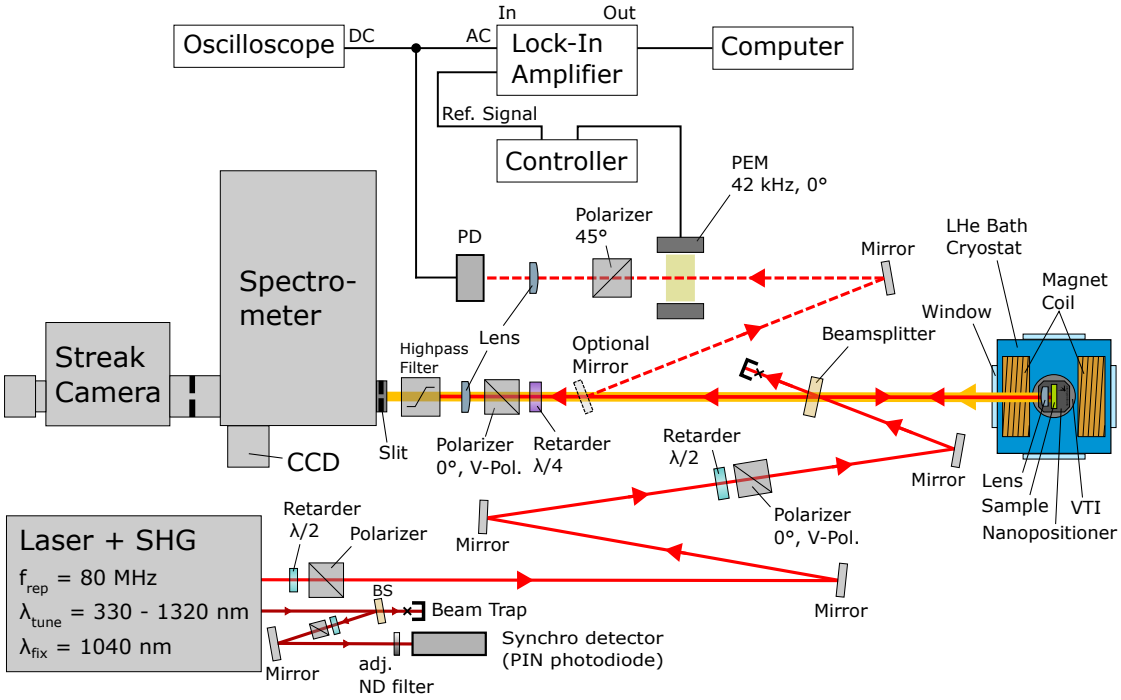

Figure 5.1: Schematic drawing of the photoluminescence spectroscopy setup with laser system, consisting of a pulsed laser and second harmonic generator (SHG), magneto-optical liquid helium bath cryostat with variable temperature insert (VTI) and superconductive split-coil magnet pairs, spectrometer with attached CCD and streak camera for time integrated and time-resolved measurements. An optional mirror in the detection path leads the reflected laser beam from the sample to the magnetic-optical Kerr effect setup with photoelastic modulator (PEM), polarizer and photodiode (PD) connected to a lock-in amplifier with the PEM frequency as reference frequency. The beam path with the fixed laser output is indicated with dark red solid lines, the tunable laser beam in red solid lines, the photoluminescence beam and detection beam path in orange solid lines and the optional MOKE beam path in dashed red lines.

The schematic drawing of the polarization resolved photoluminescence spectroscopy setup is shown in Figure 5.1. The laser system consist of a pulsed laser and second harmonic generator (SHG). The laser has a tunable and fixed wavelength output and repetition rate of 80 MHz and pulse width of 200 fs with a spectral width of about 10 meV. The adjustable output beam of the laser is used with the SHG, that makes a gapless wavelength range from 330 to 1320 nm usable. The excitation laser beam is characterized by retarder and polarizer optics in excitation power and polarization, and directed with a beam splitter to the sample. The used beam splitter is a beam sampler with small wedge angle of 0.5° and anti-reflective (AR) coating at the back surface to minimize ghosting. For focussing the excitation beam and collimating the reflected beam or photoluminescence (PL) a lens is used.

The sample is inside the variable temperature insert (VTI) of a liquid helium bath cryostat with superconductive split coil magnets with up to $B = \pm 5\,\mathrm{T}$ and is surrounded by superfluid liquid helium in measurements below 4.2 K and helium exchange gas at 4.2–300 K. The cryostat and sample are rotated by 90° to change the direction of applied magnetic field and use the same excitation and detection beam path as shown. In the

detection is a spectrometer with a triple turret and dispersion gratings for spectral resolution. The spectrometer has in the one exit a LN_2 cooled CCD for time integrated measurements and in the other exit a streak camera for time-resolved measurements (see Section 5.2).

The polarization of the photoluminescence in the detection beam path is analyzed by the combination of a $\lambda/4$-retarder and a polarizer. The retarder is placed in a motorized rotary mount to select between left and right circular polarization. The polarizer is set to 0° for the transmission and to select vertical linear polarized light. The analyzed beam is focused with an achromatic lens (AR coated, $f = 150\,\text{mm}$, $d = 50\,\text{mm}$) to the entrance slit of the spectrometer. A long pass filter in front of the slit is used to cut out laser signals from the photoluminescence and protect the sensitive CCD devices.

The description above is for the detection of circular polarization that is done with a linear polarized excitation beam and selecting in circular polarization detection by rotating the retarder. To resolve the optical orientation a $\lambda/4$-retarder is placed in the excitation path behind the polarizer and the detection beam path is analyzing the circular polarization same as in the circular polarization detection. For optical alignment measurements the excitation beam is set to linear polarization and the motorized retarder in detection is changed to a $\lambda/2$-retarder to select between vertical and horizontal linear polarization.

An optional mirror in the detection can be used to lead the reflected laser beam from the sample to the MOKE detection. The MOKE detection consist of a photoelastic modulator (PEM) with 42 kHz at 0°, polarizer in 45°, lens and photodiode (PD) connected to a lock-in amplifier with the first harmonic of the PEM frequency as reference signal.

The laser beam from the fixed wavelength output is decreased in power by a $\lambda/2$-retarder and polarizer, detected by a PIN diode and used as frequency signal source for the streak camera in synchroscan operate mode for time-resolved photoluminescence spectroscopy measurements (see Section 5.2).

One special in the shown setup above is the lens in front of the sample inside the VTI to focus and collimate the excitation and detection beam. The achromatic lens has a diameter of $d = 8\,\text{mm}$ and focus length of $f = 10\,\text{mm}$ that leads to a numeric aperture of NA = 0.54 and enables a focussed spot size of 4 µm. The lens and sample are placed on a sample holder with nanopositioner where the lens position is fixed and the sample position can be moved in xyz-direction that allows microscopy with the magneto-optical liquid helium bath cryostat.

If the microscopy is not needed, an achromatic lens with the diameter of $d = 50\,\text{mm}$ and focus length $f = 250\,\text{mm}$ placed on a xyz-stage in front of the cryostat is used. The spot size on the sample with this lens is around 100 µm. Both lenses are used with anti-reflective coating for the needed range.

For all measurements and type of sample holder a temperature and Hall sensor is placed close to the sample.

5.2 Time-Resolved Photoluminescence Spectroscopy

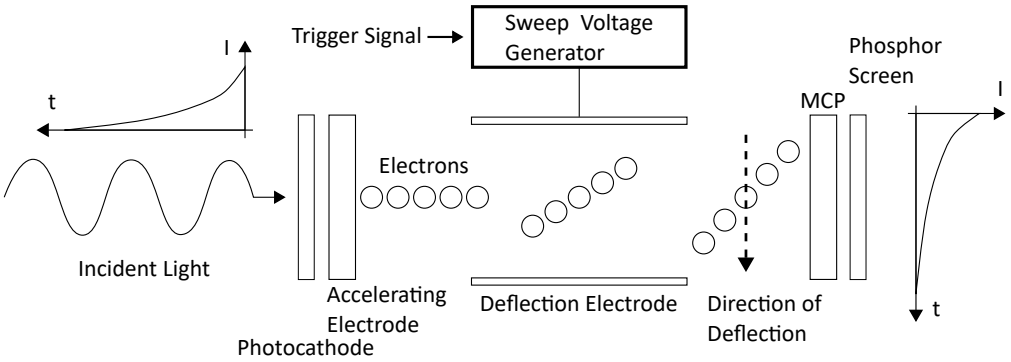

Figure 5.2: Operating Principle of the streak camera. The incident light is converted to electrons by a photocathode and accelerated within the streak tube. The electrons are deflected by a pair of deflection plates with an applied sinusoidal wave sweep voltage, which results in the time-dependent deflection of the electron beam. The deflection occurs in a specific direction, typically from top to bottom, as the electrons pass through a microchannel plate (MCP). The electrons from the MCP are hitting a phosphor screen that converts the electrons back into photons and a CCD camera records the occuring streak image. [110]

Figure 5.2 illustrates the fundamental operating principle of the streak camera. The streak camera operates on the principle of an electron tube, referred to as the streak tube. Incident light is converted into photoelectrons by a photocathode, and these photoelectrons are then accelerated by an accelerating electrode.

The accelerated electrons are directed through a pair of deflection plates, where a high-speed sinusoidal sweep voltage, applied by the synchroscan unit in operate mode, enables temporal resolution. The deflected photoelectrons are swept from the top to the bottom and further multiplied by a microchannel plate (MCP), which enhances the electron signal by a multiplication process. Upon exiting the MCP, the electrons strike a phosphor screen, where they are reconverted into an optical image.

This optical image is referred to as the streak image and is subsequently recorded by a high-speed CCD camera. The temporal resolution of the light signal is mapped onto the spatial axis in the vertical direction. When a spectrometer is placed in front of the streak camera, the photon energy distribution is mapped onto the horizontal spatial axis, with wavelengths increasing from left to right. Thus, the streak image displays time resolution along the vertical axis and spectral resolution along the horizontal axis, with the intensity of the signal proportional to the photoluminescence intensity of the incident light.

The streak image can be obtained using either the analog integration method or the photon counting method, the latter is described in detail in Section 5.2.1.

A PIN diode is used to measure the laser signal and for optical triggering the sweep voltage of the streak camera, ensuring accurate synchronization for the start time of the measurements. The PIN diode averages over 100 pulses to compensate for jitter in the laser pulses and ensure precise time referencing. The synchroscan unit of the streak camera offers four distinct time ranges, each with a different time window.

The high-speed CCD camera has a resolution of 1280×1024 pixels (horizontal $\times$ vertical), but for the measurements, the pixels were binned 2×2, resulting in a streak image resolution of 640×512 pixels. In operate mode of the synchroscan unit, the

time resolution is mapped onto the vertical axis, with 512 pixels offering a temporal resolution of approximately 10 ps by usage of the spectrometer. The spectral resolution is determined by the horizontal axis with 640 pixels, which is defined by the grating used in the spectrometer. [110]

The calibration of both the time and spectral axes is described in Section 5.2.2.

Prior to each measurement, the signal on the streak camera is optimized using live mode image acquisition. The adjustment of the intensity signal is first performed in focus mode, where the intensity maximum is centered on the streak camera display. Once the intensity is properly centered, operate mode is used to position the signal in the upper part of the image, approximately 10 % from the top edge of the streak image, with the decay direction oriented from top to bottom by adjusting the delay time. Afterward, the photon counting routine is initiated to set up the background and threshold.

Most of the time-resolved measurements presented in this work have been performed using photon counting mode, which offers enhanced sensitivity for capturing low-intensity signals.

5.2.1 Principle of Photon Counting

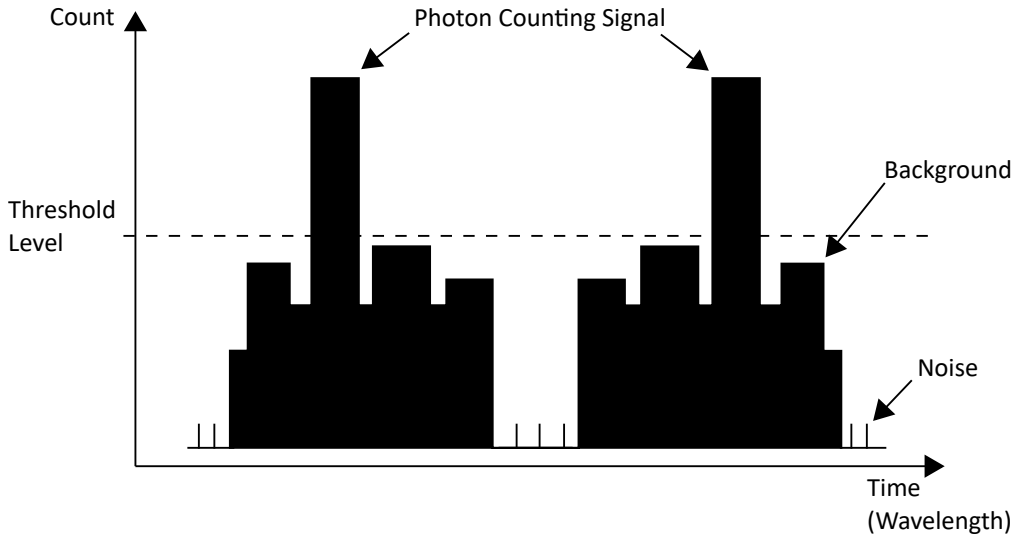

Figure 5.3: Principle of the photon counting for a technically measured signal in dependence of the time or wavelength with peaks in the intensity signal and noise in the background. A threshold level value is set to measure photoelectrons above this level and separate from background signal. [110]

Photon counting is an image acquisition mode of the streak camera to measure low signals and count photons. In this mode the acquisition parameter photon counting threshold, exposure time, number of acquisition for integration and MCP gain is adjustable. Figure 5.3 shows the schematic spectrum of a technically measured intensity signal in dependence of the time or wavelength on a CCD with peaks in the intensity signal and noise in the background. A threshold level value is used to cut out background signal and measure only signals exceeding the threshold level. During a measurement in photon counting mode a region of interest is specified in the streak image and the current percentage of pixel above the threshold level is measured. It is recommended to keep the threshold above value below 5 % by adjusting the MCP gain value to avoid overlapping photon

signals and reduce counting error. Thus a high signal-to-noise ratio is achieved. [110, 111]

5.2.2 Calibration of Streak Camera Axis

The information about spectral and time calibration of the streak image axis are useful and needed for measurements. Changes in laser system, spectrometer or streak camera system in the experimental setup a recalibration is needed. By using a spectrometer in front of the streak camera as described in Section 5.1 the spectral calibration has to be checked. The use of a new laser system and adjusting the synchroscan unit to the laser frequency makes recalibration of the time axis calibration mandatory.

Spectral Axis

The spectral axis of the streak image is the horizontal axis. Due the usage of a spectrometer with diffraction grating in front of the streak camera a calibration of the spectral resolution is needed. Thus a Neon-Argon (Ne-Ar) calibration lamp was used that was mounted in front of the entrance of the spectrometer. An image was taken with the LN_2 cooled CCD and with the CCD of the streak camera in focus mode (no time resolution) for each grating for a fixed centered wavelength close to the region of interest for later measurements. In the following the procedure for the $300\,\mathrm{mm}^{-1}$ grating will be discussed.

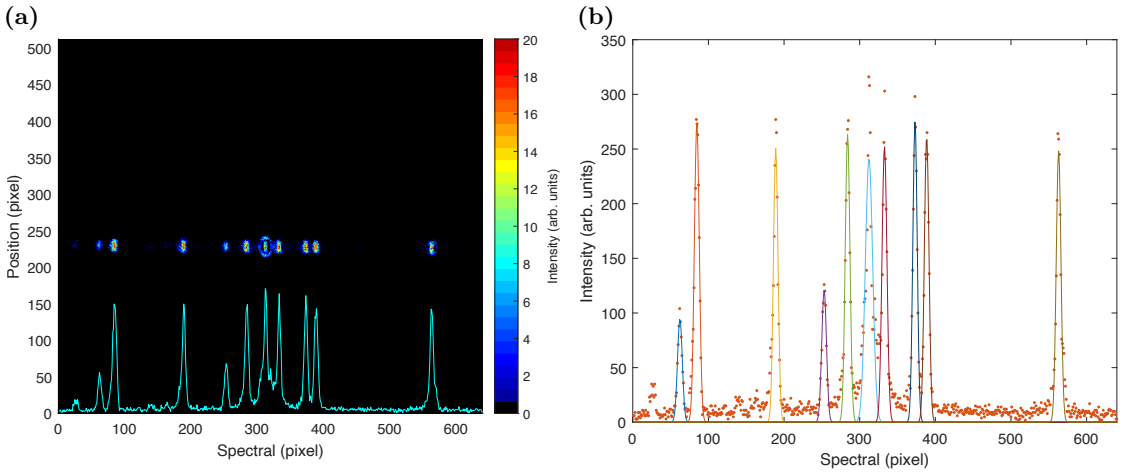

Figure 5.4: Intensity signal of the Ne-Ar calibration lamp measured with the streak camera attached to a spectrometer with the grating set to $g = 300\,\mathrm{mm}^{-1}$ centered to the wavelength $\lambda_c = 750\,\mathrm{nm}$. Figure 5.4a shows the streak image in focus mode. The vertical position on the CCD and horizontal spectral resolved axis are in units of pixel. The cyan solid line plot at the horizontal axis shows the time integrated and spectrally resolved intensity signal obtained from the streak image. Figure 5.4b the spectral resolved intensity signal (red, dotted) spectrum with Gaussian fit (different colored solid lines) for each spectral peak to find the central peak position x_c in the intensity signal.

Figure 5.4a shows the streak image of the Ne-Ar calibration lamp for grating $g = 300\,\mathrm{mm}^{-1}$ with centered wavelength $\lambda_c = 750\,\mathrm{nm}$. The streak image shows the position of the intensity signal on the CCD in the vertical axis and spectral resolved signal in the

horizontal axis in units of pixel. The integrated and spectral resolved intensity signal is shown as cyan solid line curve at the horizontal axis on the streak image. This signal is used to achieve the peak position of the intensity signal with a Gaussian fit

$$y = Ae^{-\left(\frac{x-x_c}{w}\right)^2} \tag{5.1}$$

with the amplitude A, x_c the peak position center and w the related peak width. Figure 5.4b shows the intensity signal with Gaussian fit for the peaks in the intensity spectrum.

The intensity peaks from the calibration lamp with characteristic wavelength in nm can be plotted as function of the peak position x_c and fitted linearly with the equation

$$\lambda(x) = m \cdot x + (\lambda_c - \lambda_0) \tag{5.2}$$

that calculates the wavelength in dependence of the pixel position $\lambda(x)$ with the slope m for a centered wavelength λ_c of the grating with an offset λ_0 as intercept. Thus the independent parameter to find with the fit are the slope m and intercept λ_0. The intercept λ_0 is needed to set the centered wavelength λ_c of the grating to the center of the streak image. That means $2 \cdot \lambda_0$ is the spectral range of a grating on the streak camera image.

The corresponding wavelength versus peak position with resulting fit from Equation (5.2) is shown in Figure 5.5a. The calibration equation for the streak camera to calculate from position in pixel to wavelength in nm for the triple grating are

$$\begin{aligned}
\lambda_{300}(x) &= 0.0525\,\text{nm/pixel} \cdot x + (\lambda_c - 16.032\,\text{nm}) \\
\lambda_{600}(x) &= 0.0253\,\text{nm/pixel} \cdot x + (\lambda_c - 7.794\,\text{nm}) \\
\lambda_{1200}(x) &= 0.011\,\text{nm/pixel} \cdot x + (\lambda_c - 3.377\,\text{nm})
\end{aligned}$$

with the indicated grating number in mm^{-1}. A comparison of the calibration on the grating $g = 300\,\text{mm}^{-1}$ for the Ne-Ar spectral lamp intensity spectrum between the CCD after the spectrometer and the streak camera is shown in Figure 5.5b. It shows that the measured intensity spectra and their peak positions from streak (blue) and spectrometer (red) CCD match to each other and the calibration fits well.

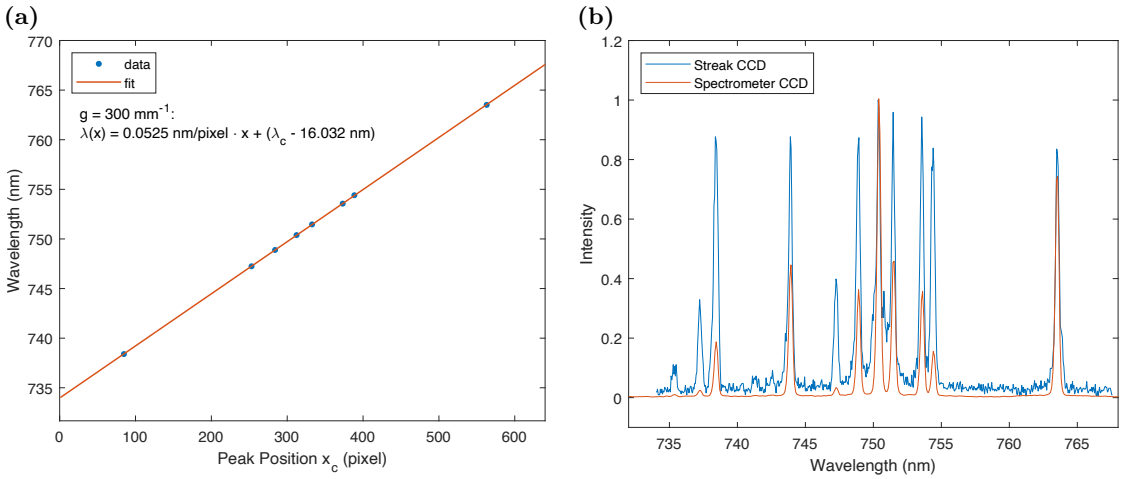

Figure 5.5: Fit results of the streak image with calibration lamp for the grating with $g = 300\,\mathrm{mm}^{-1}$ centered to the wavelength $\lambda_c = 750\,\mathrm{nm}$. Figure 5.4a Wavelength peak position of the spectral lamp as function of the peak position x_c (blue dots) with linear fit (5.2) (red solid line). Figure 5.5b Comparison of the calibration with the Ne-Ar spectral lamp intensity in dependence of the wavelength measured between the CCD behind the spectrometer (red curve) and streak camera (blue curve) shown within the region of the streak camera CCD range.

Time Axis Calibration

The time axis in the streak image is the vertical axis and given in pixel that has to calibrated into ps for each time range of the synchroscan sweep unit. The calibration is done in operate mode where a sine wave sweep voltage is applied to the deflective plates and phase locked with the delay unit (time-resolved, locked) and with a laser beam at the wavelength 735 nm with an optical delay line and the grating $300\,\mathrm{mm}^{-1}$ inside the spectrometer centered to the laser wavelength. The optical delay line has a delay time of 6.67 ps per 1 mm movement and is moved several numbers of equally fixed steps with taking streak images. The measurement of each of the four time ranges of the streak camera begins in the upper range of the streak image that correspondents to smaller times as first step and reaches the end of the time range window for the last step. The taken steps on the optical delay line for the time ranges 1 to 4 are 5 mm, 10 mm, 15 mm and 30 mm. By reaching the end of the time range window the delay line is moved back to the start position at the upper range of the streak camera to check a shift in time and thus the stability of the measurement series.

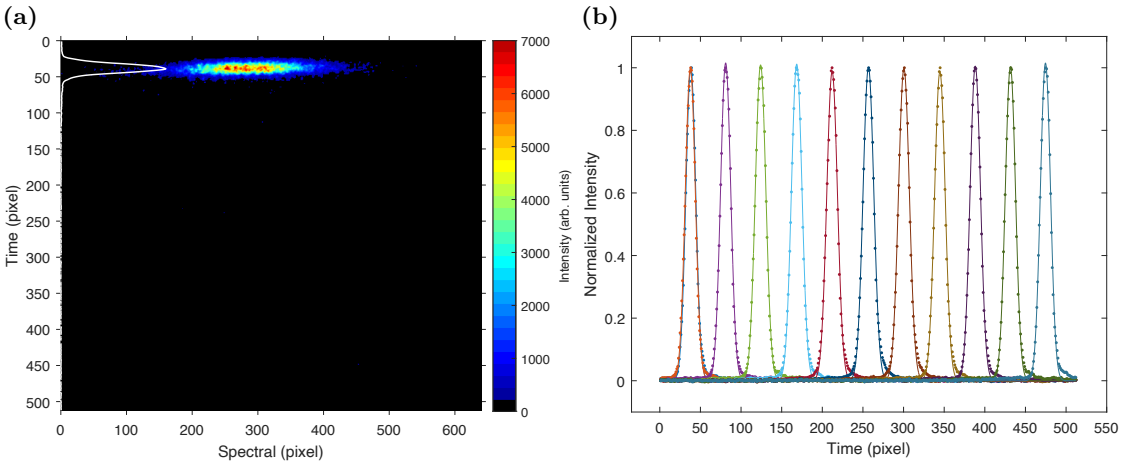

Figure 5.6: Time-resolved intensity signal in units of pixel measured with the streak camera in time range 3. Figure 5.6a shows the time and spectral resolved streak image of the laser in time range 3 at the first delay step. The vertical time axis and horizontal spectral axis are in units of pixel. The white line at the time axis shows the time-resolved intensity and is integrated over the spectral axis. Figure 5.6b shows the time-resolved intensity at different time position on the streak camera in units of pixel for different delay time steps shown as dotted curves and their corresponding Gaussian fits shown as solid line curve in the same color. At the first time position at 40 pixel are two curves, one from the first measurement at the beginning (blue) and one from the last measurement in the end (orange) to check the stability of the measurement series over the time.

Figure 5.6a shows the first taken time-resolved light signal at the upper range of the streak image in time range 3. The vertical time axis and horizontal spectral axis are in the units of pixel. The white curve at the left time axis shows the time-resolved intensity in pixel units integrated over the horizontal axis. This signal is used to achieve the peak position x_c of the intensity signal with a Gaussian fit (5.1). The measured time-resolved intensities for different delay times and thus times on the streak image are shown Figure 5.6b. The dotted points indicates the measured data and the solid lines in the same color show the Gaussian fit for each time position.
To achieve the time axis calibration in units of ps/pixel the delay time in ps against the peak position in pixel can be fitted with a linear equation

$$t(x) = m \cdot x + b \tag{5.3}$$

where m is the slope with the unit ps/pixel and the intercept b. The slope in the linear equation is the time axis calibration on the streak camera. The intercept is not need for the time axis calibration, but it is needed for fitting and analysis due to the first peak is set as reference time zero, but was nonzero at the position on the streak image. The delay time versus peak position in pixel with the fit Equation (5.3) is shown in Figure 5.7. The time axis calibration values for the different time ranges 1 to 4 of the streak camera are $0.41, 1.56, 2.28$ and 4.2 ps/pixel and shown in Table 5.1 with their time window. The time window is the maximum time range achieved by multiplying the time axis calibration with the number of 512 vertical pixels for the time resolution and it follows approximately $210, 790, 1170$ and 2150 ps.

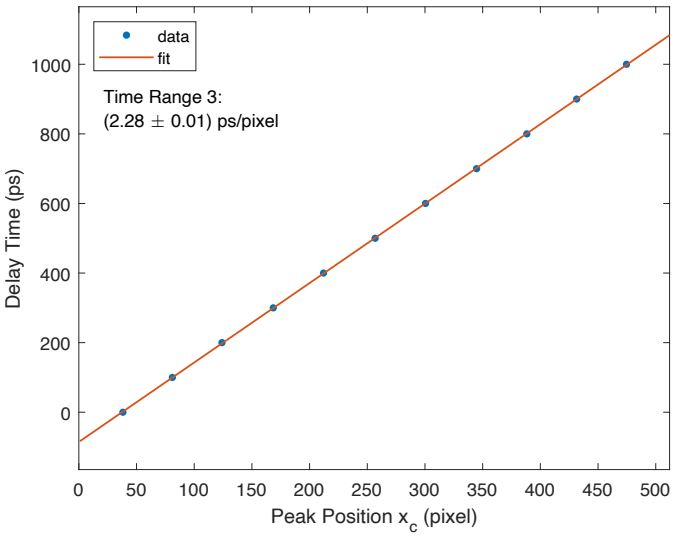

Figure 5.7: Delay time as function of peak position x_c from Gaussian fit (5.1) curve fitted with a linear fit curve (5.3). The first peak position is set to zero delay time and used as reference time $t = 0$. The slope from the linear fit is the time calibration for the corresponding time range. The intercept is needed to find the correct fit and slope, but not needed further to use for calibration of the time axis. Time range 3 has a slope of 2.28 ps/pixel and a time window of 1170 ps.

Table 5.1: Time axis calibration and maximum time limit for different time ranges of the streak camera in the synchroscan operate mode.

Time Range	**Calibration (ps/pixel)**	**Time Window (ps)**
1	0.41	210
2	1.56	790
3	2.28	1170
4	4.2	2150

5.3 Evaluation of MOKE

The experimental setup for MOKE studies the polarization state of light for the reflected light from a magnetized material. PMOKE is measured in Faraday geometry where the applied magnetic field orientation is parallel to the incident (reflected) light and normal to the sample surface. PMOKE signal is proportional to the out-of-plane magnetization of the magnetic film. In addition, longitudinal MOKE is measured in Voigt geometry with incident light close to normal incidence giving access to the in-plane component of magnetization.

The excitation beam was vertically linear polarized. The reflected beam was modulated by a photoelastic modulator (PEM) at a frequency of $f = 42\,\mathrm{kHz}$ in $\lambda/2$ mode. The modulated beam is analyzed by a polarizer at 45°. The analyzed light is detected by a photodiode (PD). The signal goes to a lock-in amplifier with the PEM signal as reference and is measured by a computer. Lock-in measurements at f and $2f$ reference frequencies give access to circular and linear polarization of reflected beam, respectively. From these data ellipticity and angle of rotation of polarization plane are evaluated. The MCD was calculated by

$$MCD = \frac{V_{1f}}{V_{\mathrm{DC}}}. \tag{5.4}$$

The Kerr-Rotation can be calculated by

$$\theta_{\mathrm{K}} = \frac{\sqrt{2}}{4J_2}\frac{V_{2f}}{V_{\mathrm{DC}}} \tag{5.5}$$

and the ellipticity [112]

$$\epsilon_{\mathrm{K}} = \frac{\sqrt{2}}{4J_1}\frac{V_{1f}}{V_{\mathrm{DC}}} \tag{5.6}$$

Here, V_{1f} and V_{2f} are the first and second harmonic signals from the lock-in, V_{DC} the DC voltage signal and J_n the n-th order Bessel function. In our case the Kerr-Rotation is

$$\boxed{\theta_{\mathrm{K}} = \frac{1}{2 \cdot 0.97} \cdot \frac{V_{2f}}{V_{\mathrm{DC}}}} \tag{5.7}$$

and the ellipticity

$$\epsilon_{\mathrm{K}} = \frac{1}{2 \cdot 1.14}\frac{V_{1f}}{V_{\mathrm{DC}}}. \tag{5.8}$$

5.4 Single Beam Optical Technique

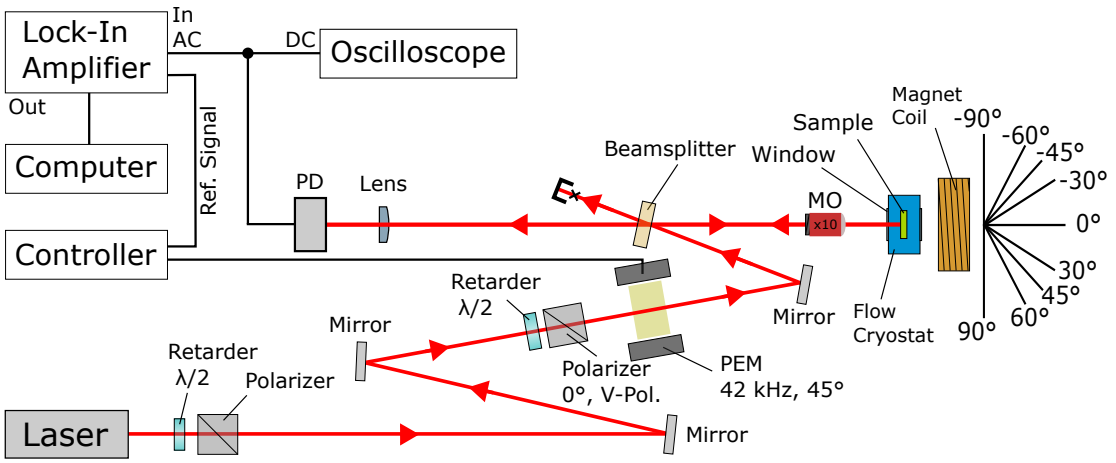

Figure 5.8: Schematic drawing of the experimental setup of the single beam experiment. The sample is excited resonantly by a pulsed laser with modulated polarization by a photoelastic modulator (PEM). A microscope objective (MO) is used to focus and collimate the laser beam. The reflected beam is detected by a photodiode (PD) connected to a lock-in amplifier (LIA) with the PEM frequency as reference. The LIA is connected to a computer and measures the AC signal of the PD while the DC signal is measured by an oscilloscope. The sample is in a bath cryostat with VTI or flow cryostat. A single coil magnet oriented in an angle around the sample surface plane and laser beam direction is used to apply magnetic fields.

In Figure 5.8 is the schematic setup of the single beam setup shown. The single beam setup alignment is used for measurements of Hanle and polarization recovery effects. It is similar to the MOKE setup with changed position of the PEM from detection into excitation of the beam. Thus the differential reflectivity $\Delta R/R$ between the circular and linear polarized excitation is measured in the double frequency that is proportional to the resident electron spin density S_z (see Section 3.5). The previous LHe magneto-optical bath cryostat is changed to an optical LHe bath cryostat with thin circumstance around the VTI or a helium flow cryostat with cold finger. That allows the usage of a microscope objective with magnitude of factor ten (NA = 0.26) in front of the sample for excitation and collimation of the laser beam. Additionally the use of a single coil electromagnet is possible that can be placed in different angle to the sample surface plane and laser beam direction. The angle is defined as laser beam direction to magnetic field direction thus $\pm 90°$ is the Hanle effect and $0°$ is polarization recovery effect. The laser is a pulsed laser with a repetition rate of 80 MHz and 1 GHz, respectively. The beam polarization and excitation power is adjusted with a $\lambda/2$ retarder and polarizer and then modulated by a PEM with the frequency $f_{\mathrm{PEM}} = 42\,\mathrm{kHz}$ in 45° from σ^+ over π to σ^- and back. The excitation energy is set to the resonant position of the QW. The laser beam signal is detected by a photodiode with lock-in amplifier (LIA) connected to a computer and PEM frequency is used as reference signal where the $2f$ signal is measured in single beam for the differential reflectivity $\Delta R/R$. The DC signal of the PD is measured with an oscilloscope.

Part III

Experimental Results

6 Magnetic Proximity Effect in Semiconductor Hybrid Structure

This part of the work about the magnetic proximity effect starts with the sample characterization of the magnetite-based hybrid structure in Section 6.1 and the demonstration of the magnetic proximity effect in magnetite-based hybrid structures with time-integrated measurements in Section 6.2. In Section 6.3 the absence of the proximity effect for conduction band electrons and valence band holes is demonstrated via pump-probe Kerr rotation.

Next, to explore the dynamics of the proximity effect, time-resolved PL measurements techniques are used. The investigation of the population dynamics in Section 6.4 allows to evaluate the characteristic lifetimes of photoexcited carriers from the decay of the total PL intensity. By investigating of the optical orientation dynamics of photoexcited carriers in Section 6.5 the spin relaxation times of photoexcited carriers from the decay of the circular polarization of the PL under circularly polarized excitation is evaluated. The dynamics of the proximity effect in Section 6.6 is studied by the dynamics of the magnetic field induced circular polarization of the PL (MCPL), which includes the contribution from the magnetized FM layer. Since the spin relaxation times of holes and electrons differ strongly, time-resolved studies make it possible to distinguish between the spin polarizations of electrons and holes bound to acceptors.

Further, the magnetic proximity effect in nickel ferrite is demonstrated in Section 6.7. Finally, the mechanism of the long-range proximity effect, the phonon Stark effect, is described in Section 6.8.1 and the conclusion are drawn in 6.8.2.

This part of the thesis is based on the work [102].

6.1 Sample Characterization

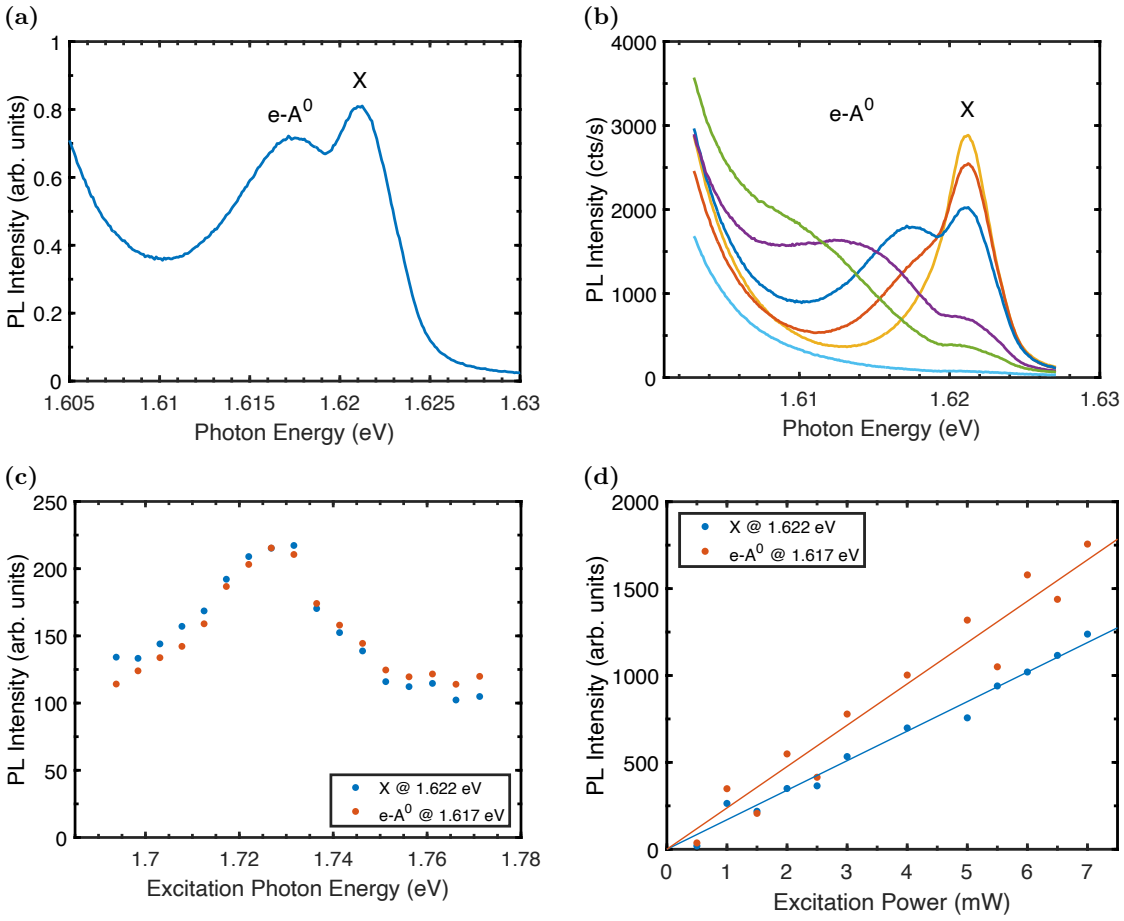

Figure 6.1: Photoluminescence (PL) spectra of the magnetite-based hybrid sample: dependencies on magnetite thickness, excitation photon energy, and power. Figure 6.1a presents the PL intensity spectrum measured at $T = 2\,\mathrm{K}$, $B = 0\,\mathrm{T}$, and an excitation photon energy of $h\nu_{\mathrm{exc}} = 1.727\,\mathrm{eV}$. The spectrum shows the exciton (X) signal at $1.622\,\mathrm{eV}$ and the acceptor-bound hole (e-A^0 optical transition) signal at $h\nu = 1.617\,\mathrm{eV}$. Figure 6.1b shows the PL intensity spectrum for varying magnetite layer thicknesses, increasing thickness from top (yellow) to bottom (bright blue) following the decreasing PL intensity of X order. Figure 6.1c illustrates the PL intensity as a function of the excitation photon energy for X and e-A^0, with the PL intensity maximum occurring at $h\nu = 1.727\,\mathrm{eV}$. Figure 6.1d depicts the PL intensity as a function of the excitation power for the exciton and acceptor-bound hole (blue dots and red dots, respectively) with a linear fit (solid line).

Figure 6.1a shows a typical photoluminescence (PL) spectrum measured at a temperature of $T = 2\,\mathrm{K}$ and an excitation photon energy of $h\nu_{\mathrm{exc}} = 1.727\,\mathrm{eV}$ in the magnetite-based structure for an intermediate thickness of the magnetite layer. The PL spectrum features an exciton (X) peak at $h\nu = 1.622\,\mathrm{eV}$ and the radiative recombination of photoexcited electrons with holes bound to acceptors (e-A^0 optical transition) in the QW at $h\nu = 1.617\,\mathrm{eV}$. The tail at lower energies, around $1.595\,\mathrm{eV}$, corresponds to the PL intensity arising from the radiative recombination of electron-hole pairs in the CdTe

buffer layer.

Figure 6.1b shows the PL intensity spectrum of the e-A^0 and X transition for different magnetite layer thicknesses, increasing thickness from top (yellow) to bottom (bright blue) following the decreasing PL intensity of X order. The e-A^0 transition becomes more pronounced and shifts to lower photon energies in regions of the sample covered with a thicker magnetite layer. The reduction in PL intensity with increasing magnetite thickness indicates the involvement of nonradiative recombination channels for electron-hole pairs.

Figures 6.1c and 6.1d present the PL intensity of the exciton X and e-A^0 transitions as a function of excitation photon energy and power, respectively. The excitation energy, measured in the range from 1.69 eV to 1.775 eV, shows maximum PL intensity at 1.727 eV. The PL intensity increases linearly with excitation power over the measured range from 0.5 mW to 7 mW. Consequently, the excitation for the time-resolved investigation is performed at the excitation photon energy corresponding to maximum intensity and at an excitation power of 1 mW. With a spot size on the sample of $d = 100\,\mu\text{m}$ the excitation power density is below $15\,\text{W}\,\text{cm}^{-2}$.

6.2 Magnetic Proximity Effect in Faraday Geometry

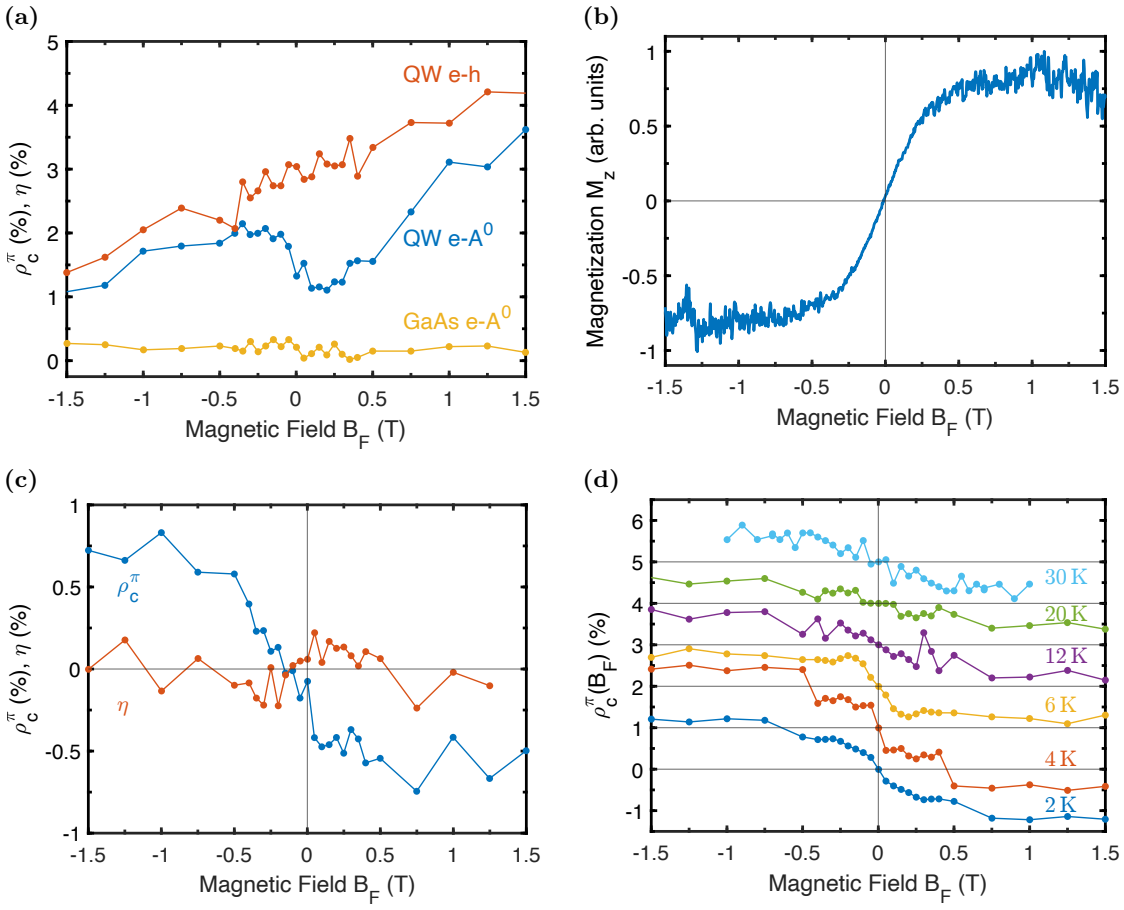

Figure 6.2: Figure 6.2a shows the magnetic field dependence of the circular polarization degree $\rho_c^\pi(B)$ under quasi-resonant linearly polarized excitation at $h\nu_{exc} = 1.629\,\text{eV}$. The measurement of $\rho_c^\pi(B)$ is done at photon energies of $h\nu = 1.618\,\text{eV}$ (e-A^0, blue dots) and $h\nu = 1.626\,\text{eV}$ (e-h, red dots), corresponding to the recombination of free electron-hole pairs. The yellow dots represent the intensity modulation parameter η of the e-A^0 transition in the GaAs substrate, measured at the photon energy $h\nu = 1.490\,\text{eV}$. The solid lines serve as guide for the eyes. Figure 6.2b illustrates the out-of-plane magnetization $M_z(B)$ of the magnetic layer as a function of the Faraday magnetic field B_F. It is measured at a temperature of $T = 2\,\text{K}$ and a photon energy of $h\nu = 1.24\,\text{eV}$. Figure 6.2c shows the intensity modulation parameter $\eta(B)$ (red dots) and the circular polarization degree $\rho_c^\pi(B)$ (blue dots) as a function of the magnetic field for the e-A^0 optical transition at $h\nu_{exc} = 1.618\,\text{eV}$ after subtracting the linear contribution. The linear contribution arises from the conventional Zeeman effect. The excitation photon energy is $h\nu_{exc} = 1.698\,\text{eV}$. Figure 6.2d shows a stacked plot with the temperature dependence of $\rho_c^\pi(B)$ as a function of the magnetic field under excitation at a photon energy of $h\nu_{exc} = 1.664\,\text{eV}$ for the e-A^0 optical transition. The horizontal grey lines indicate the zero values of each stacked curve at $B_F = 0$.

The spin polarization of photoexcited carriers can be evaluated from the circular polarization degree ρ_c^π of the photoluminescence (PL) under linearly polarized excitation (π

light). It is defined as:

$$\rho_c^\pi = \frac{I_{\sigma^+}^\pi - I_{\sigma^-}^\pi}{I_{\sigma^+}^\pi + I_{\sigma^-}^\pi}, \tag{6.1}$$

where $I_{\sigma^+}^\pi$ and $I_{\sigma^-}^\pi$ represent the PL intensities detected in σ^+ and σ^- polarizations, respectively. Figure 6.2a shows the magnetic field dependence of the circular polarization degree $\rho_c^\pi(B)$, measured under quasi-resonant excitation at $h\nu_{exc} = 1.629\,\text{eV}$, which is approximately 7 meV above the exciton resonance (X peak). The analyzed photon energies correspond to the e-A^0 optical transition (1.618 eV) and the radiative recombination of free conduction band electrons with valence band holes (e-h, 1.626 eV), which is 4 meV above the exciton transition.

The e-h recombination exhibits a linear magnetic field dependence, attributed to the equilibrium population of the Zeeman-split spin levels of the photoexcited carriers. In contrast, the acceptor band shows a nonmonotonic behavior, indicating the presence of a magnetic proximity effect, i.e., ferromagnetism (FM)-induced spin polarization of holes bound to acceptors, which is absent for free electrons and holes.

Figure 6.2b presents the FM magnetization curve, proportional to the Kerr rotation angle of the polarization plane of light with photon energy $h\nu = 1.24\,\text{eV}$, reflected from the sample and measured by the polar magneto-optical Kerr effect (PMOKE). The saturation of the magnetization corresponds to a rotation angle of 0.2 mrad. The magnetic field dependence of the circular polarization $\rho_c^\pi(B)$ at the e-A^0 transition in the CdTe QW correlates with the FM magnetization curve.

After the subtraction of the linear contribution due to the conventional Zeeman effect, the $\bar{\rho_c^\pi}(B)$ dependence (Figure 6.2c) reproduces the shape of the magnetization curve, with the saturation field $4\pi M \approx 0.6\,\text{T}$, consistent with the value reported for the Fe_3O_4 film [113]. This result indicates that the magnetic proximity effect is induced by the magnetite film itself, whereas in metal-based systems, it is induced by the interfacial FM layer [9, 15].

Magnetic circular dichroism refers to the difference in absorption coefficients for σ^+ and σ^- polarized light in the FM layer. To assess its contribution to the $\rho_c^\pi(B)$ dependence, the intensity modulation parameter η is measured, defined as:

$$\eta = \frac{I^{\sigma^+} - I^{\sigma^-}}{I^{\sigma^+} + I^{\sigma^-}}, \tag{6.2}$$

where I^{σ^+} and I^{σ^-} are the total PL intensities detected under σ^+ and σ^- polarized laser light excitation. Figure 6.2a (yellow dots) shows that the intensity modulation parameter, corresponding to the PL from the GaAs substrate ($h\nu = 1.490\,\text{eV}$), is close to zero. Therefore, the nonmonotonic $\rho_c^\pi(B)$ dependence cannot be attributed to magnetic circular dichroism through excitation and detection via the FM layer.

Additionally, the modulation parameter η, measured at the e-A^0 band in the CdTe QW, is also close to zero and remains unaffected by the magnetic field, as shown in Figure 6.2c (red dots). This confirms that the observed magnetic proximity effect is not related to the spin-dependent capture of photoexcited carriers into the FM layer [7].

This behavior is consistent with expectations for the long-range proximity effect, as the thickness of the (Cd,Mg)Te layer between the QW and the FM is 7 nm, which is significantly larger than the penetration length ($< 1\,\text{nm}$) of the carrier wave function into the (Cd,Mg)Te barrier [9].

The characteristic feature of the proximity effect is further evidenced by its resonant nature: valence band holes do not interact with the FM, whereas holes bound to acceptors do.

The temperature dependence of the polarization curves $\bar{\rho}_c^{\pi}(B)$ enables the separation of contributions from the magnetite layer and magnetic clusters. Magnetic clusters exhibit paramagnetic behavior, making the shape and saturation field of the polarization curve highly sensitive to temperature increases. In the case of the FM-induced proximity effect, the polarization curves remain unchanged, as observed in the experiment, as shown in Figure 6.2d.

6.3 Larmor Precession of Photoexcited Carriers evaluated from Pump-Probe Kerr-Rotation

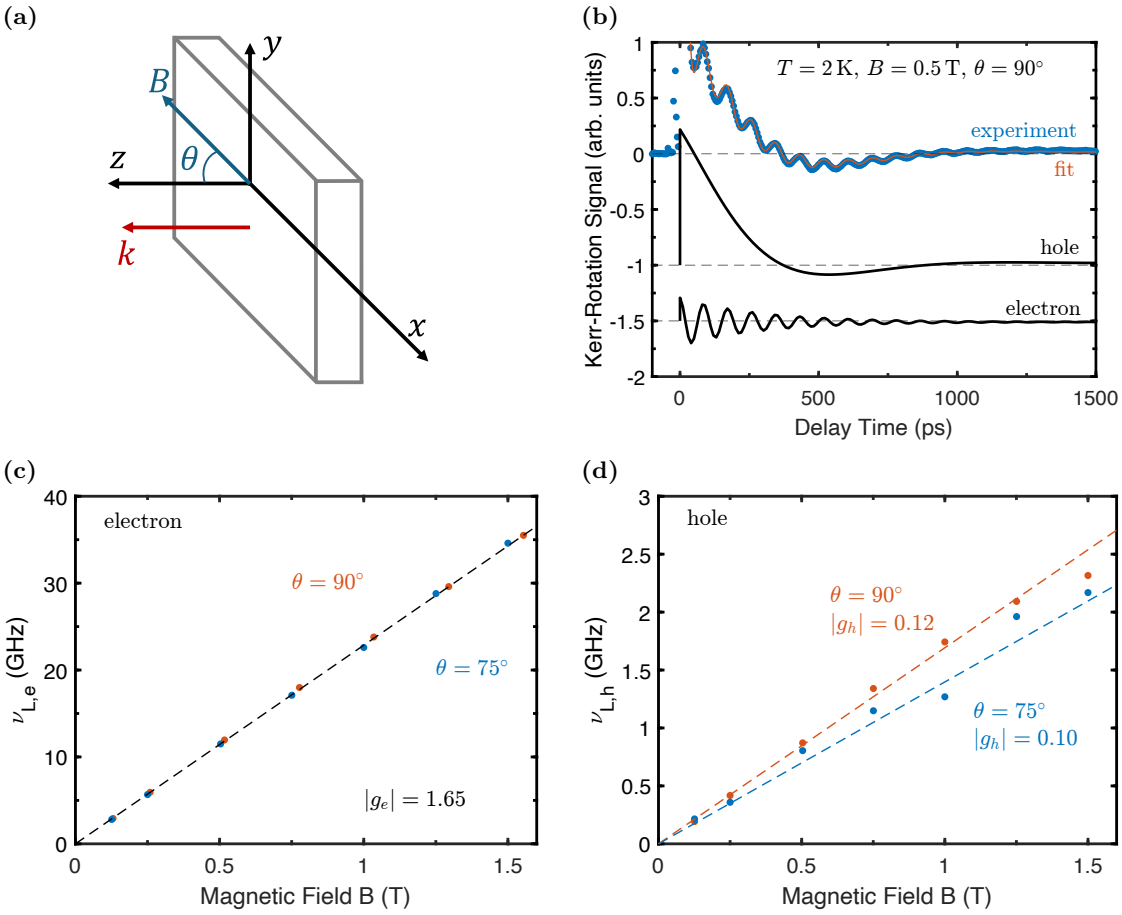

Figure 6.3: Figure 6.3a shows the experimental geometry, where the magnetic field orientation relative to the z-axis is defined by the angle θ. Figure 6.3b shows the time-resolved pump-probe Kerr rotation signal measured in Voigt geometry ($\theta = 90°$) at $B = 0.5\,\mathrm{T}$ and $T = 2\,\mathrm{K}$. The experimental data and the corresponding fit, based on the Equation (6.3) with $C = 0$, are represented by the blue dots and red solid curve, respectively. Contributions from electrons and holes are included in the fit and are represented by black solid curves. Dashed horizontal lines indicate the zero-level signal. For the fitting parameters, the electron values are $K_\mathrm{e} = 2.2$, $T^*_{2,\mathrm{e}} = 290\,\mathrm{ps}$, and $\nu_{\mathrm{L,e}} = 11.5\,\mathrm{GHz}$, while the hole values are $K_\mathrm{h} = 12.2$, $T^*_{2,\mathrm{h}} = 240\,\mathrm{ps}$ and $\nu_{\mathrm{L,h}} = 0.77\,\mathrm{GHz}$. Figures 6.3c and 6.3d show the magnetic field dependence of the Larmor frequency for conduction band electrons and valence band holes, respectively, measured at $\theta = 90°$ (red circles) and $\theta = 75°$ (blue dots), with linear fits as dashed lines. The g-factors are determined from the slopes of these linear fits.

Time-resolved studies allow detailed access to the dynamics of the proximity effect. In particular, the use of a transient pump-probe technique based on detection via the magneto-optical Kerr effect enables an investigation of the charge carrier spin dynamics. [87, 114]. A crucial parameter that can be extracted from pump-probe transients is the Larmor precession frequency of the photoexcited or resident charge carriers, denoted

by ν_L. The magnetic field dependence $h\nu_\mathrm{L} = g\mu_\mathrm{B}B + \Delta_\mathrm{exch}$ provides a method for determining the energy of exchange splitting Δ_exch, for electrons or holes as a result of their exchange interaction with the ferromagnetic (FM) layer. This exchange splitting is expressed by an effective exchange field $B_\mathrm{exch} = \Delta_\mathrm{exch}/(g\mu_\mathrm{B})$ which is induced by the FM layer. Here g stands for the Landé factor of the carrier, μ_B for the Bohr magneton and h for Planck's constant.

The value of B_exch is determined by extrapolating the linear dependence in the limit of small magnetic fields, as shown in previous studies on conduction band electrons in (Ga,Mn)As/GaAs/(In,Ga)As hybrid structures [7]. In this study, the samples are positioned in a vector magnet system consisting of three orthogonally aligned superconducting coils. This arrangement allows the measurement of the Kerr rotation signal under different magnetic field orientations defined by the angle θ relative to the z-axis, without having to adjust the optical alignment of the sample or the detection method.

The exact values of the magnetic field components in the Faraday (z-axis) and Voigt geometry (x- and y-axis) are determined using three Hall sensors positioned near the sample. The measurements are performed at a temperature of $T = 2\,\mathrm{K}$ and in magnetic fields up to $B = 1.5\,\mathrm{T}$. For sample excitation and initialization of the photoexcited electron (or hole) spin along the z-axis, circularly polarized pump pulses of 1.5 ps duration (spectral width approximately 1 meV) are generated by a mode-locked Ti:sapphire laser operating at a repetition rate of 75.7 MHz (repetition period $T_\mathrm{R} = 13.2\,\mathrm{ns}$). The helicity of the pump pulses is modulated between σ^+ and σ^- polarizations at a frequency of 50 kHz with a photoelastic modulator. This ensures that the sample is irradiated uniformly and without intensity fluctuations with left- and right-circularly polarized pump pulses.

The excited sample region is investigated with linearly polarized pulses in reflection geometry. The photon energies of both the pump and probe pulses are tuned to resonate with the free exciton in the CdTe QW $h\nu_\mathrm{exc} = 1.621\,\mathrm{eV}$, which enables a degenerate pump-probe scheme. The pump power ranges from 0.3 to $10\,\mathrm{W\,cm^{-2}}$, while the probe power is about $0.15\,\mathrm{W\,cm^{-2}}$. The spot size of the pump beam on the sample is about 300 µm, whereas the probe beam has a slightly smaller spot size. The Kerr rotation signal, which is proportional to the rotation angle of the linear polarization plane of the probe pulse, is measured as a function of the time delay between the pump pulse and the probe pulse with a symmetrical detector coupled to a lock-in amplifier. A double modulation detection method is used in which the intensity of the probe beam is modulated at a frequency of 84 kHz.

An example of a pump-probe transient measured in a magnetic field of 0.5 T in Voigt geometry, where the magnetic field B is parallel to the sample plane ($B \parallel x$) and perpendicular to the optical axis, is shown in Figure 6.3b. For the extraction of parameters such as the spin dephasing time, the relative amplitudes and Larmor precession frequencies for electrons and holes, the transients are fitted with the following function:

$$\begin{aligned} K(t) = {} & K_\mathrm{e}\cos\left(2\pi\nu_\mathrm{L,e}t + \phi\right)\exp\left(-\frac{t}{T^*_\mathrm{2,e}}\right) \\ & + K_\mathrm{h}\cos\left(2\pi\nu_\mathrm{L,h}t + \psi\right)\exp\left(-\frac{t}{T^*_\mathrm{2,h}}\right) + C\exp\left(-\frac{t}{\tau_\mathrm{nos}}\right). \end{aligned} \tag{6.3}$$

Here K_e (K_h), $T^*_\mathrm{2,e}$ ($T^*_\mathrm{2,h}$), $\nu_\mathrm{L,e}$ ($\nu_\mathrm{L,h}$), and ϕ (ψ) denote the amplitude, the dephasing time, the Larmor precession frequency and the initial phase of the fast (slow) oscillating components of the Kerr rotation signal, which are assigned to the conduction band

electrons or the valence band holes. The terms C and τ_{nos} represent the amplitude and decay time of the non-oscillating component that occurs when the magnetic field has a component unequal to the z-axis.

The magnetic field dependences of the Larmor precession frequencies for electrons and holes are shown in Figures 6.3c and 6.3d. Only the Larmor precession frequencies of conduction band electrons and valence band holes are accessible, since the efficient optical orientation of photoexcited carriers under circularly polarized excitation is achieved by resonant exciton pumping, which has a much larger oscillator strength than that of excitons bound to acceptors. The dependencies for electrons Figure 6.3c and holes Figure 6.3d are shown for the Voigt field orientation ($\theta = 90°$, red dots) and oblique geometry ($\theta = 75°$, blue dots). All dependencies are well described by a linear slope of the Larmor precession frequency, where the slope is defined by the g-factors of the photoexcited charge carriers. For electrons, the g-factor is approximately isotropic with a value of $|g_{\mathrm{e}}| = 1.65$, which agrees well with previous results in comparable CdTe-QW structures [115, 89]. For holes, the magnitude of the g-factor $|g_{\mathrm{h}}| \approx 0.1$.

In cases where FM-induced exchange splitting of spin levels occurs, an additional offset in the $\nu_{\mathrm{L}}(B)$ dependence is expected. For the long-range interaction mediated by elliptically polarized phonons, the proximity effect requires a magnetization component along the z-axis M_z, as $\Delta_{\mathrm{exch}} \sim M_z$ [9]. It is therefore essential to evaluate the $\nu_{\mathrm{L}}(B)$ dependence under oblique magnetic fields. However, no measurable offset is observed in the $\nu_{\mathrm{L}}(B)$ dependencies for each θ in Figure 6.3. This confirms that, in contrast to holes bound to acceptors, neither valence band holes nor conduction band electrons are affected by the effective exchange magnetic field induced by the FM layer (Section 6.2). For electrons, the interaction with the FM is significantly weaker due to the limited spin-orbit coupling, while for valence band electrons the splitting between heavy and light holes ($\sim 20\,\mathrm{meV}$) far exceeds the characteristic energy of elliptically polarized phonons ($\sim 1\,\mathrm{meV}$). This result is also consistent with previous studies of the long-range proximity effect in Co/(Cd,Mg)Te/CdTe QW structures, where a similar behavior was observed [14].

6.4 Population Dynamics of Photoexcited Electrons and Holes

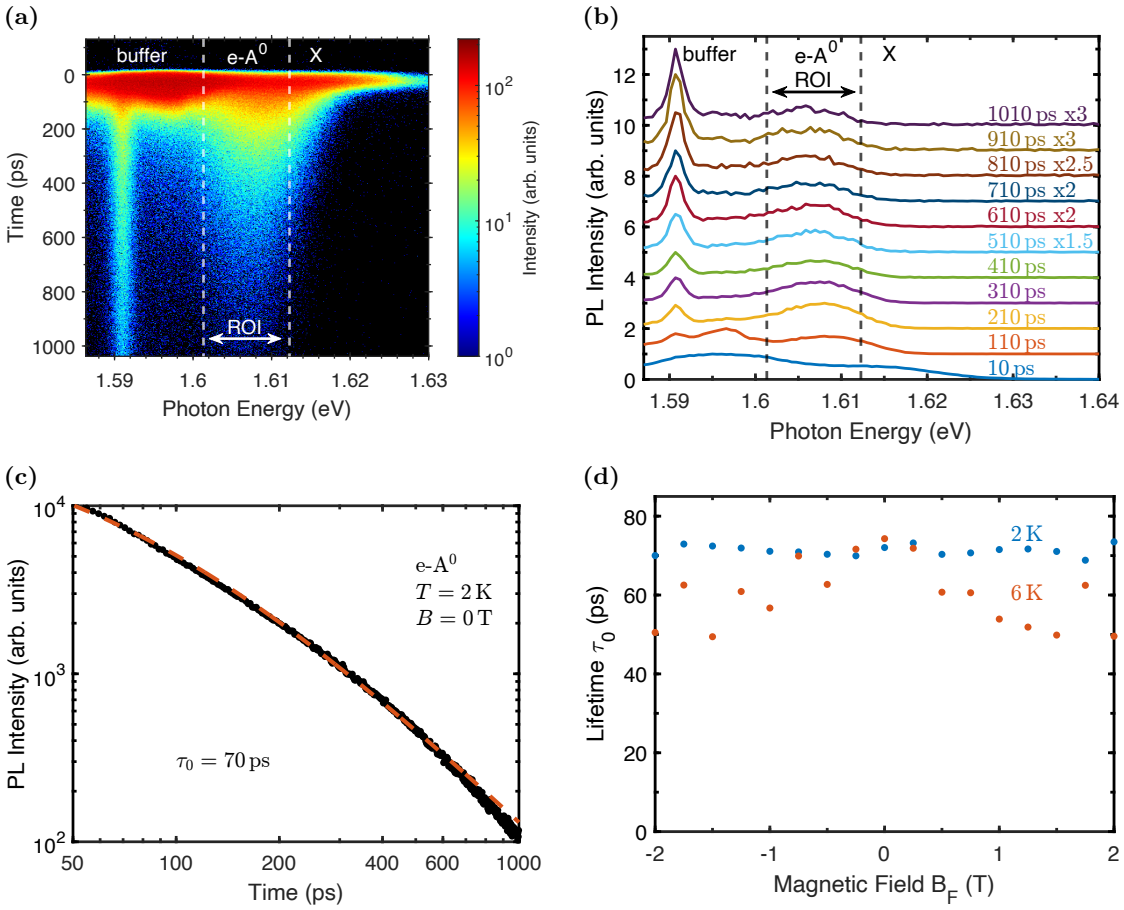

Figure 6.4: Population dynamics of electrons and holes. Figure 6.4a shows a streak image of time versus photon energy, with a colorbar representing the total photoluminescence (PL) intensity with signals originating from the buffer layer at 1.595 eV, the e-A^0 transition at 1.607 eV, and the e-h recombination at 1.62 eV. The streak image is measured at $T = 2\,\mathrm{K}$, $B = 0\,\mathrm{T}$, and excitation photon energy $h\nu_{\mathrm{exc}} = 1.727\,\mathrm{eV}$. The region of interest (ROI) is indicated by vertical dashed lines and spans 11 meV, centered at the maximum of the e-A^0 signal. Figure 6.4b illustrates the stacked plot of the temporal evolution of the PL decay. The signal from the buffer layer significantly interferes with the intensity of the e-A^0 signal in the quantum well (QW) up to 200 ps. Therefore, the QW signal for $t > 200\,\mathrm{ps}$ is used for analysis. Figure 6.4c shows the PL intensity decay of the e-A^0 optical transition (black dots) and the corresponding fit (red dashed line) to determine the lifetime τ_0 at $B = 0\,\mathrm{T}$ and $T = 2\,\mathrm{K}$. The PL intensity and fit are displayed logarithmic scales on both axes. Figure 6.4d presents the lifetime $\tau_0(B)$ as a function of the Faraday magnetic field B_{F}.

The main results of the population dynamics of the photoexcited carriers are summarized in Figure 6.4.

A streak image of the total photoluminescence (PL) intensity plotted against time and photon energy is presented in Figure 6.4a. It is measured at $T = 2\,\mathrm{K}$, $B = 0\,\mathrm{T}$, and an excitation photon energy of $h\nu_{\mathrm{exc}} = 1.727\,\mathrm{eV}$ in the absence of a magnetic field and shows

signals originating from the buffer layer at 1.595 eV, the e-A^0 transition at 1.607 eV, and the e-h recombination at 1.62 eV.

Figure 6.4b depicts the time evolution of the PL spectrum from bottom to top. Immediately after excitation (blue line at the bottom, $t = 10$ ps after the laser pulse), the spectrum is broad and comprises both primary contributions: a rapid decay on the timescale of several tens of picoseconds from the radiative recombination of excitons in the CdTe quantum well (QW) at a photon energy around 1.62 eV and the PL from the CdTe buffer layer centered around 1.595 eV. Starting from 100 ps after the laser excitation pulse, a prominent e-A^0 band, attributed to the recombination of thermalized electrons with holes bound to acceptors, appears centered around 1.607 eV. The peak at 1.591 eV is attributed to the recombination of excitons bound to impurities in the CdTe buffer [116].

In the subsequent analysis, the PL signal related to the e-A^0 optical transition is defined as the region of interest (ROI). The vertical dashed lines indicate the ROI, which is centered at the maximum of the e-A^0 band with a width of $\Delta_{\mathrm{ROI}} = 11$ meV, integrated to obtain time-resolved intensity data. The PL signal is evaluated in the time range from 500 to 1000 ps. The signal maximum in the ROI at zero magnetic field is located at 1.607 eV (vertical dashed lines in Figures 6.4a and 6.4b). The signal shifts to 1.609 eV in a Faraday magnetic field of 2 T due to a diamagnetic shift.

Figure 6.4c shows the analyzed temporal evolution of the PL signal on a log-log scale. Due to the PL intensity contribution from the CdTe buffer layer at short time delays, the signal before $t = 50$ ps is excluded from the analysis. The decay is non-exponential, and the recombination follows bimolecular recombination behavior, described by Equation (3.93) in Section 3.7.2 with $I(t) = \frac{n_0}{\tau_0} \frac{1}{(1+t/\tau_0)^2}$, which typically occurs in intrinsic semiconductors. Here, n_0 represents the density of electron-hole pairs, and τ_0 is their characteristic instantaneous lifetime at the moment of excitation. For $T = 2$ K and $B = 0$, the lifetime is determined to be $\tau_0 = 70$ ps from fitting the data using this equation.

Figure 6.4d presents $\tau_0(B)$ as a function of the Faraday magnetic field at $T = 2$ K and 6 K. The lifetime of $\tau_0 = 70$ ps at $T = 2$ K (blue dots) is independent of B and decreases slightly at $T = 6$ K. Therefore, the instantaneous lifetime remains approximately the same for different Faraday magnetic fields and temperatures.

6.5 Optical Orientation of Photoexcited Carriers

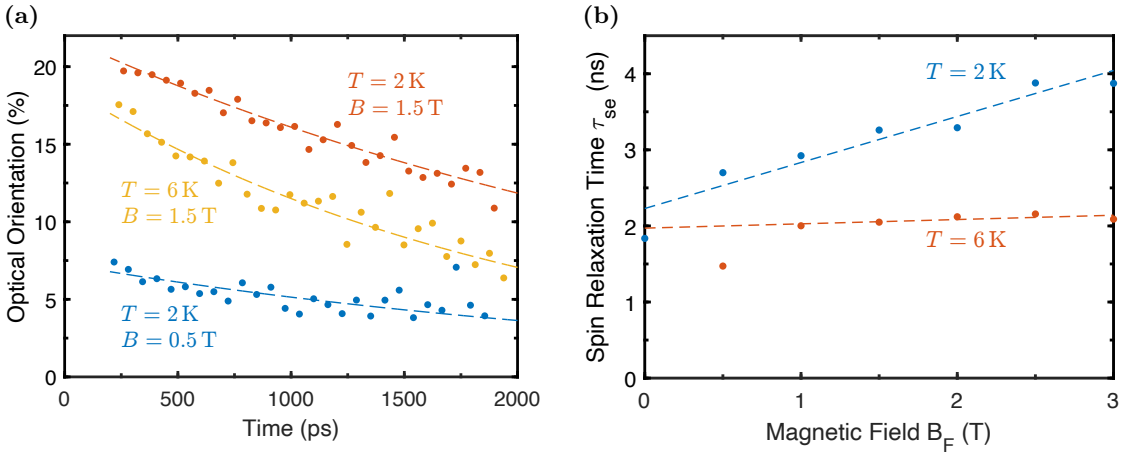

Figure 6.5: The dynamics of the optical orientation transients $\rho_c^c(t)$ at different temperatures and Faraday magnetic fields are presented. The dashed lines in Figure 6.5a represent exponential fits based on Equation (6.6). The magnetic field dependence of the spin relaxation time $\tau_{se}(B)$, evaluated from these exponential fits for $T = 2$ K and 6 K, is shown in Figure 6.5b. The dashed lines serve as visual guides.

To determine the spin relaxation times of photoexcited carriers, their optical orientation is measured, where circularly polarized excitation results in spin-polarized electrons and holes. The spin polarization is detected through the degree of photoluminescence (PL) circular polarization, defined as:

$$\rho_c^{\sigma^+} = \frac{I_{\sigma^+}^{\sigma^+} - I_{\sigma^-}^{\sigma^+}}{I_{\sigma^+}^{\sigma^+} + I_{\sigma^-}^{\sigma^+}}, \tag{6.4}$$

where $I_{\sigma^+}^{\sigma^+}$ and $I_{\sigma^-}^{\sigma^+}$ represent the PL intensities detected in σ^+ and σ^- polarizations, respectively, under σ^+ polarized light excitation. In an external magnetic field applied in the Faraday geometry ($B \parallel z$), an additional contribution due to carrier thermalization between spin levels, known as magnetic circular polarization of luminescence (MCPL), is present. To exclude this MCPL effect, the symmetric part of the circular polarization degree with respect to the excitation helicity is analyzed:

$$\rho_c^c(B) = \frac{\rho_c^{\sigma^+}(B) + \rho_c^{\sigma^-}(B)}{2}. \tag{6.5}$$

The excitation photon energy is approximately 100 meV above the exciton transition energy, suggesting rapid spin relaxation of holes due to the complex valence band structure [42]. Therefore, the optical orientation signal $\rho_c^c(t)$ is predominantly determined by the spin polarization of photoexcited electrons, which decays exponentially from its initial value $P_e(0)$ with the electron spin relaxation time τ_{se}, described by:

$$P_e(t) = P_e(0) \exp\left(-\frac{t}{\tau_{se}}\right). \tag{6.6}$$

The results of the optical orientation measurements are summarized in Figure 6.5. Examples of $\rho_c^c(t)$ transients are shown in Figure 6.5a for $B = 0.5$ T and 1.5 T at two

different temperatures, $T = 2\,\mathrm{K}$ and $T = 6\,\mathrm{K}$. The temporal dependencies are well described by the exponential decay given in Equation (6.6), which is used to evaluate the spin relaxation time τ_{se} and the initial spin polarization $P_{\mathrm{e}}(0)$.

The evaluated spin relaxation times and their dependence on the magnetic field for $T = 2\,\mathrm{K}$ and $T = 6\,\mathrm{K}$ are presented in Figure 6.5b. At $T = 2\,\mathrm{K}$, the spin relaxation time increases from 2 ns in the absence of a magnetic field to 4 ns at a magnetic field of 3 T. At a higher temperature of 6 K, the dependence of $\tau_{\mathrm{se}}(B)$ remains nearly constant at 2 ns.

6.6 Dynamics of the Magnetic Proximity Effect

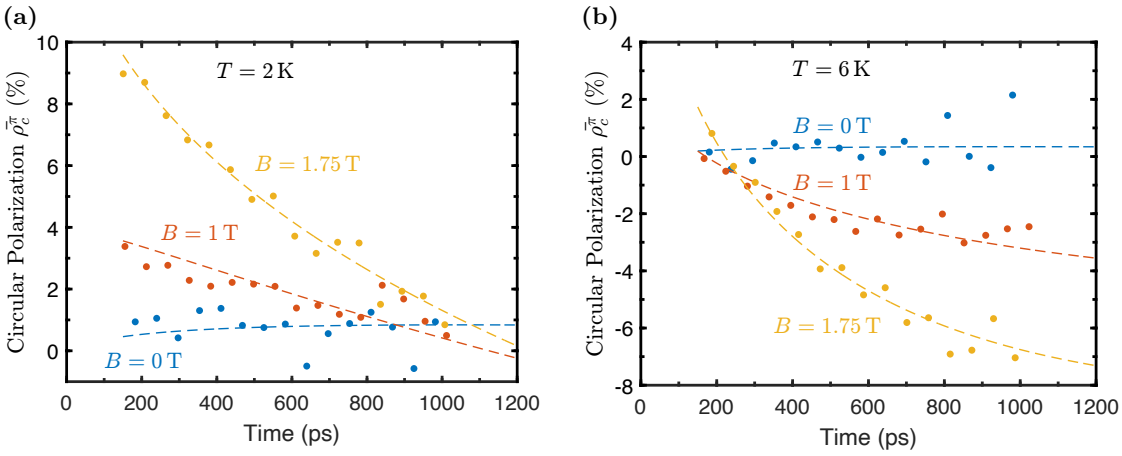

Figure 6.6: The dynamics of the magnetic proximity effect are analyzed through the temporal dependence of the circular polarization $\bar{\rho}_{\mathrm{c}}^{\pi}$ for various Faraday magnetic fields, measured at $T = 2\,\mathrm{K}$ (Figure 6.6a) and $T = 6\,\mathrm{K}$ (Figure 6.6b). The dashed lines represent fits of the circular polarization degree using Equation (3.97).

The dynamics of the proximity effect are investigated by analyzing the temporal dependence of the magnetic field-induced circular polarization, $\rho_{\mathrm{c}}^{\pi}(B)$, under excitation with linearly polarized light. In this scenario, non-polarized electrons and holes are generated. The degree of magnetic circular polarization of luminescence (MCPL) is determined similarly to the continuous wave (cw) experiment Equation (6.1). For $B > 0$, the polarization initially starts at a positive value and gradually decreases over time. Applying the magnetic field in the opposite direction ($B < 0$) reverses the polarization relative to zero. This is a characteristic behavior of MCPL, as expressed by

$$\rho_{\mathrm{c}}^{\pi}(-B) = -\rho_{\mathrm{c}}^{\pi}(+B). \tag{6.7}$$

Figure 6.6 presents the temporal dependence of the circular polarization antisymmetrized with respect to the magnetic field,

$$\bar{\rho}_{\mathrm{c}}^{\pi}(t) = \frac{\rho_{\mathrm{c}}^{\pi}(+B) - \rho_{\mathrm{c}}^{\pi}(-B)}{2}, \tag{6.8}$$

for Faraday magnetic fields $B = 0$, 1, and 1.75 T, measured at $T = 2\,\mathrm{K}$ (Figure 6.6a) and $T = 6\,\mathrm{K}$ (Figure 6.6b). While $\bar{\rho}_{\mathrm{c}}^{\pi}(t)$ remains positive at $T = 2\,\mathrm{K}$, it changes sign around

200 ps at $T = 6$ K. The initial value of $\bar{\rho}_c^{\pi}$ for $t < 100$ ps is attributed to the equilibrium spin polarization of the acceptor-bound holes,

$$P_h = -\frac{g_A \mu_B B_{eff}}{2k_B T}. \tag{6.9}$$

This value appears almost immediately (~ 20 ps) after excitation with a laser pulse due to the short spin relaxation time of holes (compared to 2 ns for electrons). Here, g_A denotes the g-factor of the acceptor-bound holes. It should be noted that B_{eff} represents the effective magnetic field, which includes contributions from both the external field B and the ferromagnetic (FM) exchange field B_{exch}, such that

$$B_{eff} = B + B_{exch}. \tag{6.10}$$

The subsequent dynamics of $\bar{\rho}_c^{\pi}$ are governed by the spin polarization P_e of electrons, which tend to reach their thermal equilibrium spin polarization

$$P_e^{eq} = -\frac{g_e \mu_B B}{2k_B T} \tag{6.11}$$

within the spin relaxation time τ_{se}. Consequently, the temporal evolution of MCPL can be approximated using the expression:

$$\bar{\rho}_c^{\pi}(t) = P_h - P_e(t) \tag{6.12}$$

$$= P_h - P_e^{eq}\left(1 - \exp\left(-\frac{t}{\tau_{se}}\right)\right). \tag{6.13}$$

From the temporal dependence of $\bar{\rho}_c^{\pi}(t)$ in Figure 6.6, both P_h and P_e^{eq} are observed to be positive, indicating that the g-factors of the carriers involved in recombination, g_A and g_e, are negative. While the g-factor $g_e = -1.64$ for electrons is known from the literature [115], the sign of the g-factor for acceptor-bound holes has not yet been established.

It is important to note that the MCPL dynamics for the magnetite-based hybrid structures differ significantly from those observed in Co-based structures, where the spin relaxation time of acceptor-bound holes ($\tau_{sh} = 2$ ns) is substantially longer [9]. Initially, the experimental data in Figure 6.6 (dots) are fitted using Equation (6.13), which enables the determination of the equilibrium spin polarization of electrons, P_e^{eq}, and of acceptor-bound holes, g_h. However, it is found that the parameter P_e^{eq} does not scale linearly with the magnetic field but rather follows the magnetization curve of the magnetite film.

In Sections 6.2 and 6.3, it is demonstrated that there is no exchange interaction between conduction band electrons and the FM. The non-linear magnetic field dependence of P_e^{eq} is attributed to the recombination-induced dynamical polarization of electrons, which becomes significant when $\tau_{sh} < \tau_0 \ll \tau_{se}$. This results in an additional term in Equation (6.13) that describes the recombination-related orientation of the electrons and leads to Equation (3.97) in Section 3.7.2

$$\rho_c(t) = P_h - P_e^{eq}\left(1 - \exp\left(-\frac{t}{\tau_{se}}\right)\right) - \tilde{P}_h \exp\left(-\frac{t}{\tau_{se}}\right) \int_0^{\frac{t}{\tau_{se}}} \frac{e^x}{x+\alpha}\, dx\,,$$

with $\alpha = \frac{\tau_0}{\tau_{se}}$ is the ratio of the electron lifetime at the moment of excitation to the ratio of the electron spin relaxation time and $\tilde{P}_h$ is the recombination-induced dynamic spin polarization. This equation is used to fit the experimental data and discussed in the

following. The only free fitting parameter are the initial polarization degree P_h at $t = 0$ and the recombination-induced dynamic spin polarization $\tilde{P}_\mathrm{h}$. The other variables are evaluated from measurements shown in the section before: the lifetime τ was evaluated in Section 6.4, the spin relaxation time τ_se in Section 6.5 and the equilibrium spin polarization of electrons P_e^eq can be calculated with the g-factor of Section 6.3.

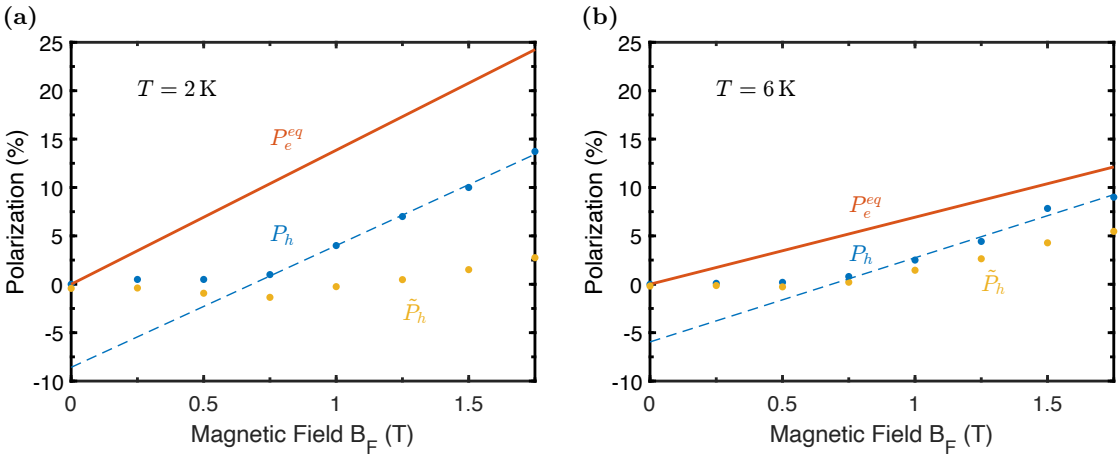

Figure 6.7: The equilibrium spin polarization of holes (P_h) and the recombination-induced dynamical polarization of electrons ($\tilde{P}_\mathrm{h}$) are shown as functions of the magnetic field at $T = 2\,\mathrm{K}$ in Figure 6.7a and at $T = 6\,\mathrm{K}$ in Figure 6.7b. The polarization data are extracted from the MCPL transients in Figure 6.6 using Equation (3.97) as the fit function. The equilibrium spin polarization of electrons (red lines) is described by $P_\mathrm{e}^\mathrm{eq} = -g_\mathrm{e}\mu_\mathrm{B}B/(2k_\mathrm{B}T_\mathrm{c})$, with $g_\mathrm{e} = -1.65$ and $T_\mathrm{c} = T + 2\,\mathrm{K}$. The blue dashed lines represent linear fits using Equation (6.14).

Figure 6.7 presents the fitting parameters P_h and $\tilde{P}_\mathrm{h}$, along with the calculated equilibrium electron spin polarization P_e^eq for $T = 2\,\mathrm{K}$ and $6\,\mathrm{K}$. The magnetic field dependence of P_h exhibits a nonlinear behavior (shown by the blue dots in Figure 6.7). It remains close to zero at low magnetic fields ($B < 0.5\,\mathrm{T}$), where the contribution from the proximity effect-induced ferromagnetic (FM) splitting is comparable in magnitude but opposite in direction to that of the external magnetic field. As the magnetization of the FM layer reaches saturation, the hole spin polarization P_h becomes positive and increases linearly with the magnetic field. The overall magnetic field dependence of $P_\mathrm{h}(B)$ can be described by the equation:

$$P_\mathrm{h}(B) = -\frac{\mu_\mathrm{B} g_\mathrm{A} B + \Delta_\mathrm{exch}(B)}{2k_\mathrm{B}T_\mathrm{c}}\,, \tag{6.14}$$

where the exchange splitting $\Delta_\mathrm{exch}(B)$ follows the magnetization of the FM film. At high magnetic fields ($B > 0.5\,\mathrm{T}$), where Δ_exch reaches saturation, a linear fit based on Equation (6.14) (dashed lines in Figure 6.7) is applied, yielding $g_\mathrm{A} = -1.8$ and a saturation value of $\Delta_\mathrm{exch} = 70\,\mu\mathrm{eV}$. Such a behavior indicates the presence of long-range magnetic proximity effect. These values are comparable to those observed in Co- and Fe-based hybrid structures [9, 16]. The parameter $\tilde{P}_\mathrm{h}$ follows a similar trend but has a lower absolute value than P_h, which aligns with theoretical expectations (see Section 3.7.1).

6.7 Magnetic Proximity Effect in Nickel Ferrite Hybrid Structure

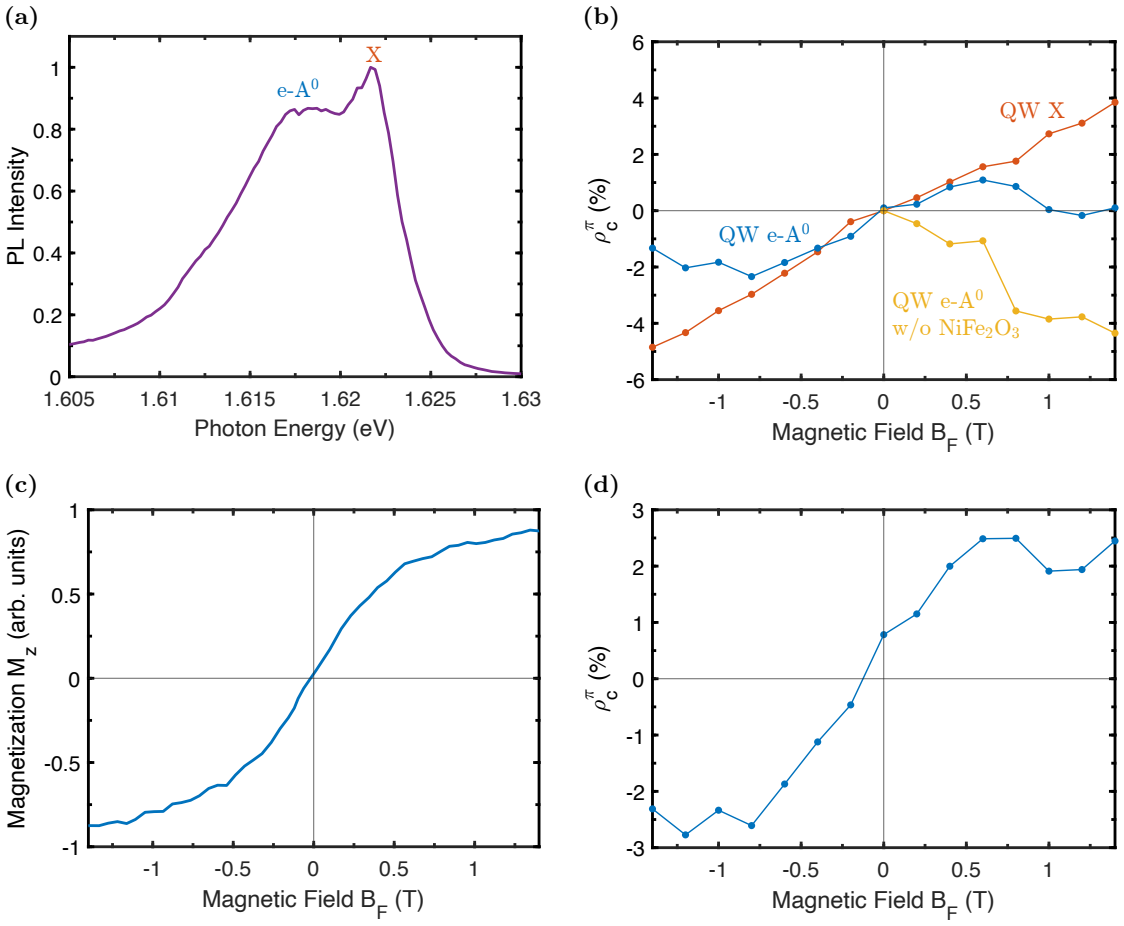

Figure 6.8: Magnetic proximity effect in nickel ferrite based hybrid structure. Figure 6.8a shows the photoluminescence (PL) spectrum measured under excitation with photon energy $h\nu_{\mathrm{exc}} = 1.696\,\mathrm{eV}$ at a temperature of $T = 2\,\mathrm{K}$. The exciton (X) peak and the e-A^0 shoulder correspond to the radiative recombination of the exciton and the electron with a hole bound to the acceptor, respectively. Figure 6.8b presents the magnetic field dependencies of the circular polarization degree under linearly polarized excitation, $\rho_{\mathrm{c}}^{\pi}(B)$, measured at photon energies of $h\nu = 1.6145\,\mathrm{eV}$ (e-A^0 in QW, blue dots for the sample with nickel ferrite, yellow dots for the sample without nickel ferrite) and $h\nu = 1.625\,\mathrm{eV}$ (X in QW, red dots) under excitation at $h\nu_{\mathrm{exc}} = 1.696\,\mathrm{eV}$. Figure 6.8c shows the magnetic field dependence of the out-of-plane magnetization $M_z(B)$ of the nickel ferrite film that is measured using polar magneto-optical Kerr effect (PMOKE). Figure 6.8d presents the dependence of $\rho_{\mathrm{c}}^{\pi}(B)$ for the e-A^0 line from Figure 6.8b after the subtraction of the linear contribution due to the conventional Zeeman effect.

Figure 6.8a presents a typical photoluminescence (PL) spectrum measured at low temperature of $T = 2\,\mathrm{K}$ under non-resonant excitation with energy $h\nu_{exc} = 1.696\,\mathrm{eV}$ in the nickel ferrite semiconductor quantum well (QW) hybrid structure. The PL spectrum is similar to that of the magnetite-based hybrid structure (Figure 6.1a), showing the exciton (X) line at $h\nu = 1.622\,\mathrm{eV}$ and the electron-acceptor bound holes band (e-A^0) centered at $h\nu = 1.617\,\mathrm{eV}$.

The dependencies of PL circular polarization under linearly polarized excitation on the Faraday magnetic field $\rho_c^{\pi}(B)$ are shown in Figure 6.8b. Here, the detection is performed at photon energies corresponding to the e-A^0 transition ($h\nu = 1.6145\,\text{eV}$, blue dots) and the exciton transition ($h\nu = 1.625\,\text{eV}$, red dots) in the CdTe QW. These detection energies are selected not at the peak maxima to prevent mutual interference of PL polarization caused by the overlap of the PL transitions.

For the QW situated 8 nm away from the ferromagnetic (FM) layer, the circular polarization degree $\rho_c^{\pi}(B)$ of the e-A^0 band exhibits a nonmonotonic behavior with saturation at higher magnetic fields (blue dots in Figure 6.8b). In contrast, for the QW not covered by the nickel ferrite layer (yellow dots in Figure 6.8b), the $\rho_c^{\pi}(B)$ dependence is linear. This indicates that the nonlinear contribution to $\rho_c^{\pi}(B)$, which saturates at high B, is attributed to the influence of the adjacent FM film, i.e., the ferromagnetic proximity effect.

The magnetic field dependence for excitons is linear, which is attributed to the equilibrium polarization resulting from the Zeeman splitting of the exciton spin sublevels. A comparison of the effects on the e-A^0 band and on the exciton suggests that only holes bound to acceptors interact with the FM. After subtracting the linear contribution from the conventional Zeeman effect, the $\rho_c^{\pi}(B)$ dependence (Figure 6.8d) precisely mirrors the nickel ferrite magnetization curve (Figure 6.8c), with a saturation field of approximately 1 T. This similarity indicates that the magnetic proximity effect is induced by the nickel ferrite film itself.

Thus, it is demonstrated that the long-range magnetic proximity effect for holes bound to acceptors in CdTe QWs within nickel ferrite based hybrid structures is analogous to that observed in magnetite-based hybrid structures.

6.8 Summary and Discussion

6.8.1 Phonon Stark Effect

The long-range proximity effect in the magnetite- and nickel ferrite-based hybrid structures is demonstrated in this work. The effect involves the effective p-d exchange interaction of acceptor-bound holes in the quantum well (QW) with d-electrons of the ferromagnet (FM), without their wave functions overlapping. In Reference [9], it is proposed that this long-range exchange interaction is mediated by elliptically polarized acoustic phonons, referred to as the phonon Stark effect. The current research confirms the validity of this mechanism and highlights its universal behavior.

The key principles underlying the phonon Stark effect are as follows:
1. In the FM, near the magnon-phonon resonance (approximately 1 meV), there is strong coupling between spin waves (magnons) and transverse acoustic phonons propagating along the magnetization direction. Only the phonon mode with a polarization vector rotating in the same direction as the magnetization vector in the spin wave participates in this coupling, leading to elliptical polarization of the phonons. [101]
2. Transverse acoustic phonons cross the interface between the FM and semiconductor with minimal damping. [117]
3. There is a significant spin-phonon coupling (Bir-Pikus interaction) in the semiconductor valence band due to large strain constants (on the order of $\sim 10\,\text{eV}$). (Reference [118]) Even a small deformation (on the order of $\sim 10^{-5}$) causes a shift in hole energy levels by $\sim 0.1\,\text{meV}$.
4. In the QW, the ground state of shallow acceptors is split into two doublets with angular momentum projections of $\pm 3/2$ and $\pm 1/2$ along the structure growth direction. The characteristic splitting energy $\Delta_{\text{lh}} \approx 1\,\text{meV}$ (Reference [119]) is close to the energy of the magnon-phonon resonance and, thus, to the energy of elliptically polarized phonons.

These factors result in the chiral phonon-mediated p-d exchange interaction. Elliptically polarized phonons generated in the FM with energy $\Delta_{\text{ph}} \sim 1\,\text{meV}$ penetrate the nonmagnetic barrier and enter the QW. In the QW, they couple with acceptor-bound holes via spin-phonon interaction. For instance, if the phonons are predominantly σ^+ polarized, angular momentum conservation leads to the coupling of the ground state $-3/2$ with the excited state $-1/2$. This coupling results in an energy shift of these levels, analogous to the optical ac Stark effect. The shift has a dispersion-like behavior: it becomes stronger as the phonon energy approaches the initial splitting Δ_{lh} of the acceptor states and vanishes when $\Delta_{\text{ph}} = \Delta_{\text{lh}}$. The sign of the shift depends on whether Δ_{ph} is smaller or larger than Δ_{lh}. The other pair of levels ($+3/2$ and $+1/2$) remains unaffected, lifting the degeneracy of the $\pm 3/2$ doublet in the absence of an external magnetic field. The splitting between the $\pm 3/2$ hole states, referred to as exchange splitting ($\Delta_{\text{exch}} \sim 0.1\,\text{meV}$), leads to equilibrium spin polarization of the holes, which manifests in the circular polarization of photoluminescence (PL) in the e-A^0 line (Section 6.2).

As expected, the long-range s-d exchange interaction is not observed for conduction band electrons (Section 6.3) due to the weaker spin-orbit interaction in the conduction band compared to the valence band. Valence band holes are similarly unaffected by elliptically polarized phonons because their $\Delta_{\text{lh}} \approx 10\,\text{meV}$ splitting is an order of magnitude larger than the phonon energy.

It is concluded that the long-range exchange is universal, occurring not only in metal-based hybrid systems but also in systems comprising semimetal or dielectric FMs. The exchange constant $\Delta_{\text{exch}} = 70\,\mu\text{eV}$ for the magnetite-based hybrid structure (Section 6.6)

is comparable to the $\Delta_{\text{exch}} = 50\,\mu\text{eV}$ reported for the Co-based structure in Reference [14]. The universality of the long-range exchange interaction is attributed to the universality of the phononic mechanism. First, the energy of the magnon-phonon resonance, and consequently the energy of elliptically polarized acoustic phonons, is close to 1 meV for many common ferro- and ferrimagnetic materials. [101] Second, despite variations in structure thickness and potential barrier heights for charge carriers, these barriers do not hinder sound waves. As a result, phonons propagate into the semiconductor over distances far exceeding the charge carrier wave function overlap with the FM.

6.8.2 Conclusions

In this chapter the long-range proximity effect in hybrid structures consisting of a FM layer (magnetite, nickel ferrite) and a semiconductor CdTe QW, separated by a thin nonmagnetic (Cd,Mg)Te barrier was demonstrated.

The effect consists in the effective p-d exchange interaction of acceptor-bound holes in the QW with d-electrons of the FM without overlap of their wave functions. This shows the universal behavior of the long-range exchange interaction for a wide range of ferromagnetic components with metals (Fe, Co), semimetals (magnetite), dielectrics (nickel ferrite), and for various potential barriers for charge carriers with different heights ($Cd_{0.6}Mg_{0.4}Te$ and $Cd_{0.8}Mg_{0.2}Te$) and different thicknesses in the range from 1 nm to 40 nm. [9, 12, 14, 15, 16]

The ubiquity of the magnetic proximity effect is attributed to the universal nature of the phononic mechanism. Moreover, the long-range exchange mechanism mediated by elliptically polarized phonons does not impose stringent requirements on the quality of interfaces. However, the non-metal systems investigated in this study exhibit different properties.

First, in contrast to metal-based hybrid structures, the proximity effect in non-metallic systems is caused by the magnetic material itself (e.g. magnetite or nickel ferrite) and not by a ferromagnetic interface. Second, the dynamics of the proximity effect in non-metal hybrid structures is not monotonic and differs significantly from that observed in metal-based structures, where the spin relaxation time of the acceptor-bound holes is much longer.

This complex dynamic behavior can be explained by considering the additional recombination-induced dynamic polarization of electrons in the quantum well (QW). It is shown that this mechanism becomes significant when the spin relaxation time of the electrons is much longer than their lifetime. Despite the lack of a long-range s-d exchange interaction for conduction band electrons, they are therefore indirectly influenced by the ferromagnet through recombination with polarized holes.

7 Spin Dynamics of Resident Electrons in Monolayer $MoSe_2$

At the beginning of the chapter the sample is characterized in its optical properties for further investigation. In the Section 7.1 the PL and reflectivity spectra are presented. The sample is characterized in its amplitude and half-width at half-maximum magnetic field dependence in excitation power and temperature by applying an external magnetic field and using the single beam optical technique. In Section 7.2 the Hanle and polarization recovery curves effects are presented and discussed.

The results of this chapter are published in [120].

7.1 Optical Properties

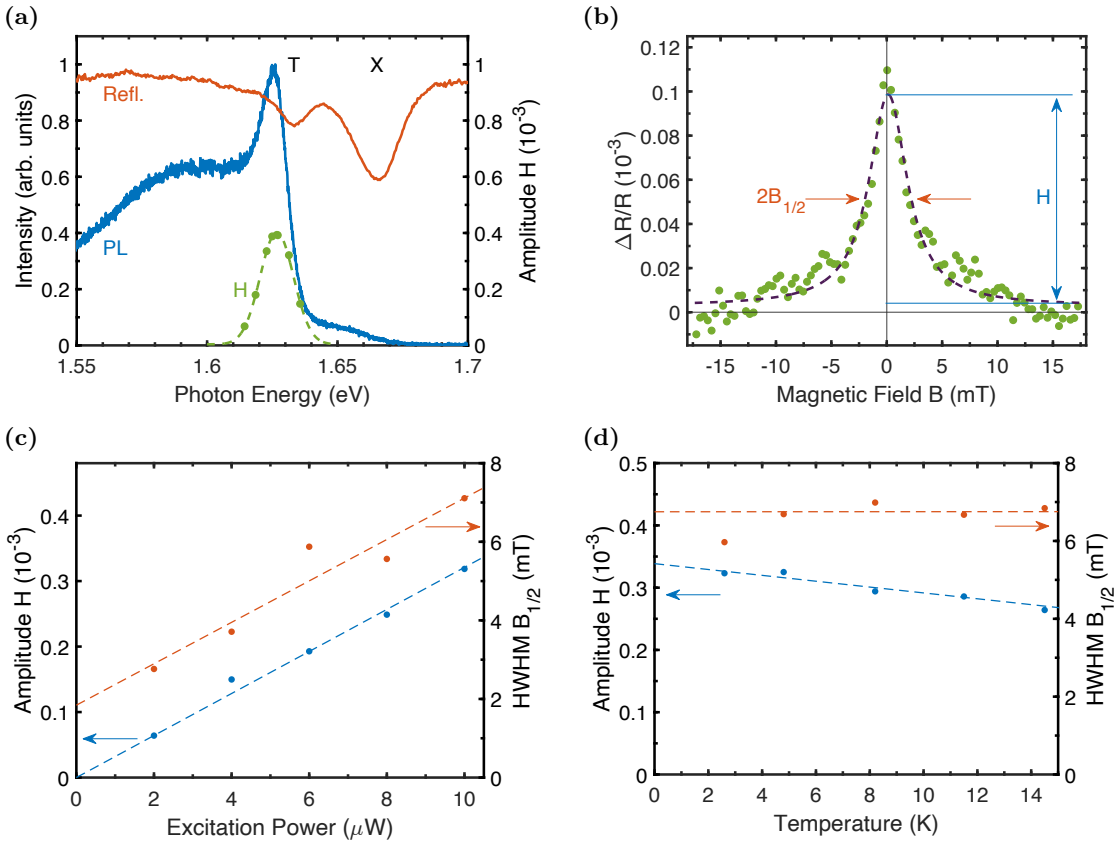

Figure 7.1: Optical properties of the TMD monolayer $MoSe_2$ on EuS. Figure 7.1a shows the photoluminescence (PL, blue solid line) and reflectivity (Refl., red solid line) intensity spectra at zero magnetic field, together with the amplitude H of the Hanle curve derived from a single Lorentzian fit as a function of excitation energy (green dots, dashed line serves as a guide for the eye). The reflectivity spectrum shows signals corresponding to the exciton (X) and trion (T), while the PL intensity spectrum shows the trion signal with a Stokes shift of 7 meV. The excitation energy reaches a maximum at 1.625 eV, which corresponds to the peak position of the trion PL intensity. Figure 7.1b shows a Hanle curve fitted with a single Lorentzian function, characterized by the amplitude parameter H and the half-width at half-maximum (HWHM) $B_{1/2}$. Figure 7.1c shows the amplitude and HWHM resulting from the single Lorentzian fit as a function of excitation power. Both parameters increase linearly with rising excitation power up to 10 µW. Figure 7.1d shows the amplitude and HWHM as a function of temperature, with no significant variation observed up to 15 K.

Figure 7.1 presents the optical properties of the TMD monolayer $MoSe_2$ on the EuS sample, including the PL and reflectivity intensity spectra shown in Figure 7.1a, a description of the Lorentzian fit to the Hanle curve and its parameters in Figure 7.1b, and the dependencies of the Hanle effect on excitation photon energy E_{exc}, excitation power P_{exc} (Figure 7.1c), and temperature T (Figure 7.1d). When these dependencies are not being measured, the experiments are conducted with $E_{\mathrm{exc}} = 1.625\,\mathrm{eV}$, $P_{\mathrm{exc}} = 10\,\mu\mathrm{W}$, and $T = 2\,\mathrm{K}$. The PL spectrum is recorded at $T = 6\,\mathrm{K}$ with an excitation photon energy

of $E_{\mathrm{exc}} = 1.823\,\mathrm{eV}$ and an excitation power of $P_{\mathrm{exc}} = 10\,\mu\mathrm{W}$.

The reflectivity (Refl., red solid line) spectrum exhibits trion (T) resonances at photon energies of 1.633 eV and exciton (X) resonances at 1.665 eV. The photoluminescence (PL) spectrum shows a trion peak at 1.625 eV with a Stokes shift of approximately 7 meV and a broader emission band at a lower energy of around 1.58 eV, indicating the presence of localized states in the $MoSe_2$ monolayer. The Fermi level of the resident electrons is estimated to be about $E_{\mathrm{F}} \approx 5\,\mathrm{meV}$ above the conduction band minimum [19], which is smaller than the spin-orbit splitting of the conduction band states with opposite spins, $\Omega_{\mathrm{SO}} = 23\,\mathrm{meV}$ [121].

The Hanle curve is measured with the magnetic field aligned at $\alpha = 90^\circ$ to the incident light direction under pulsed excitation at $f = 80\,\mathrm{MHz}$ with a photon energy of $\hbar\omega = 1.631\,\mathrm{eV}$ and a light intensity of $P_{\mathrm{exc}} = 8\,\mu\mathrm{W}$. The depolarization of resident electron spins (reduction of S_z) is described by a Lorentzian curve with an amplitude H at $B = 0$ and a half-width at half-maximum (HWHM) of $B_{1/2} = 2.1\,\mathrm{mT}$.

The Hanle effect is observed in proximity to the trion resonance, as indicated by its spectral dependence shown in Figure 7.1a, and is attributed to spin-selective absorption during the probing process of the spin density S_z [94]. Both the amplitude H and the HWHM $B_{1/2}$ increase linearly with the excitation power P_{exc}.

This behavior is explained by two factors: first, the light absorption at the trion resonance in the linear regime, where the density of excited trions is significantly lower than the carrier spin density n_{e} and $\Delta R \propto S_z$; and second, the reduction in the resident electron spin lifetime due to trion excitation. In the low-power limit, the value of $B_{1/2} \approx 1.9\,\mathrm{mT}$ corresponds to the intrinsic spin relaxation time, which is comparable to values reported for electrons in MoS_2, WS_2, and WSe_2 monolayers [24, 25].

Increasing the temperature to $T = 15\,\mathrm{K}$ does not significantly alter the parameters of the Hanle curve.

7.2 Hanle And Polarization Recovery Effects

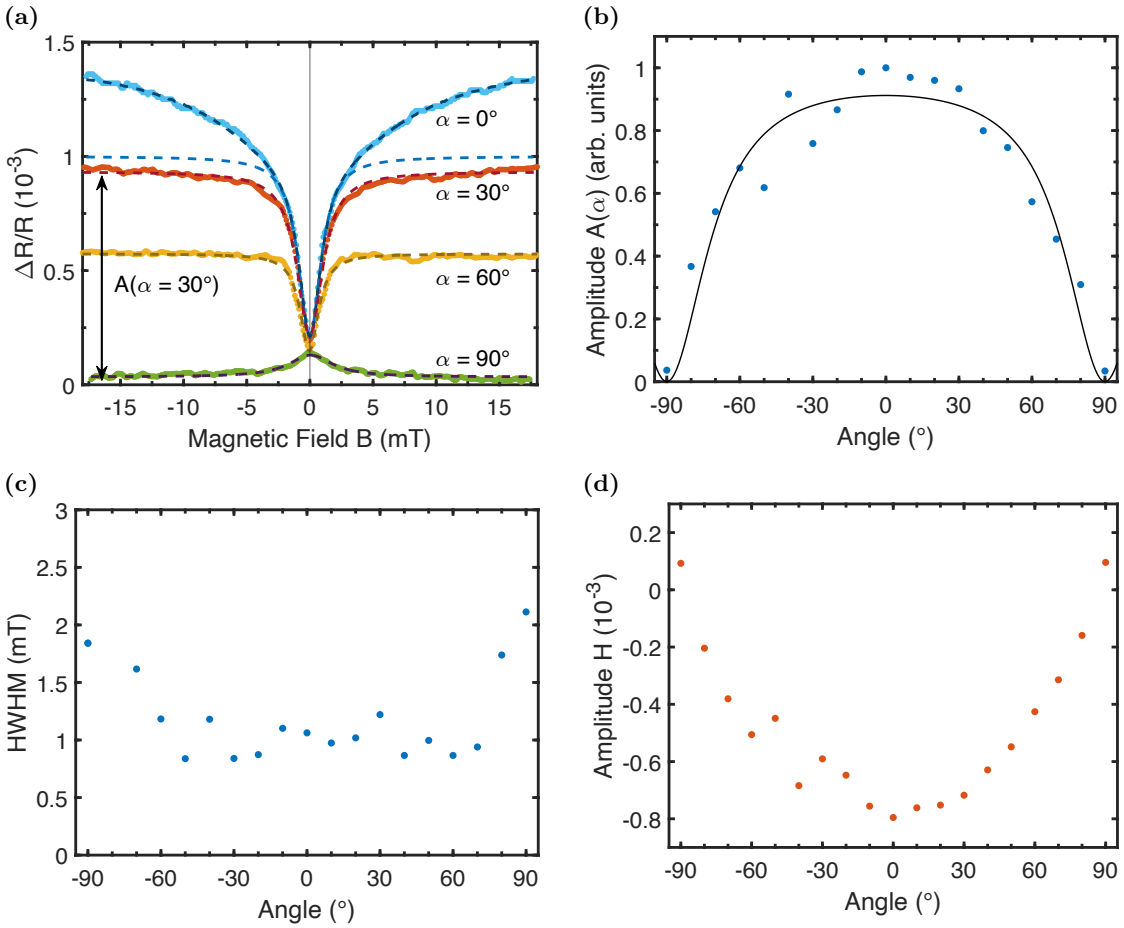

Figure 7.2: The Hanle curve and the polarization recovery curve (PRC) are measured in oblique magnetic fields at $T = 5\,\mathrm{K}$ with an excitation photon energy of $E_{\mathrm{exc}} = 1.625\,\mathrm{eV}$, an excitation power of $P_{\mathrm{exc}} = 4\,\mu\mathrm{W}$, and a repetition rate of $f_{\mathrm{rep}} = 1\,\mathrm{GHz}$. Figure 7.2a shows the differential reflectivity $\Delta R/R$ as a function of the magnetic field for angles of 0°, 30°, 60° and 90°. The angle-dependent amplitude $A(\alpha)$, which represents the offset of the Lorentz curve, shows the change in polarization between zero magnetic field and saturation polarization. Figure 7.2b shows the angular dependence of the amplitude as a function of the magnetic field angle relative to the surface plane (black dots), together with the fitted function (black line). For the half-width at half-maximum (HWHM), the ratio is $a = 3$. Figure 7.2c shows the HWHM as a function of the magnetic field angle relative to the surface plane (blue dots). The data show a ratio of $a = 3$ between the HWHM values at $\alpha = 0$ and $\alpha = \pm 90°$. Figure 7.2d shows the amplitude H as a function of the magnetic field angle relative to the surface plane (red dots).

Figure 7.2a displays the differential reflectivity $\Delta R/R$ as a function of the magnetic field for different applied angles: 0°, 30°, 60°, and 90°. Depolarization is observed at 0° in the Voigt geometry, while polarization recovery occurs at 90° in the Faraday geometry and in oblique magnetic fields. The differential reflectivity $\Delta R/R$ is proportional to the spin polarization S_z and increases and saturates during polarization recovery when the external magnetic field B_{ext} increases.

For angles $\alpha > 30°$ the data can be fitted with a single Lorentzian function, resulting in a half-width at half-maximum (HWHM) $B_{1/2}$ of a few mT. However, for angles $\alpha \leq 30°$, an additional contribution to polarization recovery is observed, which can be described with a double Lorentzian function (see blue and dark blue dashed lines for $\alpha = 0$ in Figure 7.2a). This additional contribution has a larger HWHM of approximately 15 mT, and it is possibly attributed to higher-energy electrons, which spin relaxation is suppressed by Zeeman splitting in a longitudinal magnetic field [28]. In the following analysis, the focus is on the narrow dip in the magnetic field dependence, while the broader polarization recovery is excluded from further consideration.

The Lorentzian fit offset, defined as the amplitude $A(\alpha)$, is shown in Figure 7.2b (black dots), along with the fit function (red line) described by Equation (3.50), which yields an anisotropy ratio $a = 3$ for the HWHM (Figure 7.2c). The amplitude $A(\alpha)$ reaches its maximum at $\alpha = 0°$ (Faraday geometry) and its minimum at $\alpha = 90°$ (Voigt geometry). The amplitude H of the polarization recovery is ten times greater than that of the Hanle effect depolarization.

In two-dimensional semiconductors, a strong out-of-plane spin-orbit field Ω_{SO} is present. This field is aligned along the z-axis and does not induce relaxation of the z-component of the electron spin. Therefore, the magnetic field in the Faraday geometry is not expected to influence the spin dynamics.

Spin depolarization of electrons in a weak transverse magnetic field has been observed with $B_{1/2} \approx 10\,\mathrm{mT}$ for AB_2 monolayers (A = Mo or W, and B = Se or S) [24, 25]. This phenomenon, combined with the absence of Larmor spin precession, has been attributed to anisotropic spin relaxation rates, $\gamma_x = \gamma_y = \gamma_s + 2\Gamma_v$ and $\gamma_z = \gamma_s$, where $\Gamma_v = \Omega_{\mathrm{SO}}^2/(4\gamma_v)$, γ_v is the spin-conserving intervalley scattering rate, and γ_s is the spin relaxation rate within the same valley [122]. This mechanism requires $E_{\mathrm{F}} > \Omega_{\mathrm{SO}}$, which is not the case here, and it neglects intervalley spin relaxation γ_{sv} (see Figure 3.4a).

The suppression of spin relaxation and dephasing by an external magnetic field suggests a different mechanism. An increase in the spin polarization of electrons localized on shallow donors in external magnetic fields of approximately 5 mT has been observed in bulk GaAs [123]. In this case, the spin of a localized electron precesses in random nuclear fields due to hyperfine interactions. A longitudinal magnetic field greater than the characteristic value of the random field, $B_{\mathrm{f}} \approx 5\,\mathrm{mT}$, suppresses the precession of the spin z-component and restores its orientation (polarization recovery), whereas a transverse magnetic field stronger than B_{f} causes electron depolarization (Hanle effect). In the $MoSe_2$/EuS heterostructure, random magnetic fields can also arise from exchange interactions with the magnetic atoms in EuS. The applied model incorporating these random fields is discussed phenomenologically in Section 3.6.

The HWHM shown in Figure 7.2b results in a ratio for the anisotropy of $a = 3$, in accordance with the predictions of the Equations (3.49) and (3.73): $\gamma_{\parallel} g_z \approx 9\gamma_{\perp} g_x$ and $\Omega_0^{\mathrm{F}} \approx \frac{\Omega_0^{\mathrm{V}}}{3}$. The HWHM in Faraday geometry is 2–3 times smaller than in Voigt geometry.

An upper limit of $\gamma_{\perp}$ is estimated from the HWHM of the polarization recovery curve in Faraday geometry at $B_{1/2}^{\mathrm{F}} = 1\,\mathrm{mT}$. Using a g-factor of $g_z = 3.68$ for the lower-energy conduction state of $MoSe_2$, determined from exciton reflectivity spectra in high magnetic fields [124], it follows that $\gamma_{\perp} < g_z \mu_{\mathrm{B}} B_{1/2}^{\mathrm{F}} \approx 0.2\,\mu\mathrm{eV}$, which corresponds to a spin relaxation time of $\hbar/\gamma_{\perp} \gtrsim 3.3\,\mathrm{ns}$.

The degree of anisotropic spin relaxation can be estimated from the ratio between amplitudes H in the Voigt and Faraday geometries, $C = H^{\mathrm{F}}/H^{\mathrm{V}} \approx 10$ (Figure 7.2d). From this, it is deduced that $\gamma_{\perp} \gtrsim 5\gamma_{\parallel}$.

Based on the above analysis, the transverse g-factor is estimated as $|g_x| \leq \sqrt{\frac{2}{C}}\frac{g_z}{a} \approx 0.15$, with $g_x \ll g_z$. It is reasonable to assume that the dispersion of the transverse g-factor δg_x due to inhomogeneities within the excitation spot is comparable to its magnitude, which could lead to suppression of oscillations in spin transients.

This suppression is corroborated by the absence of oscillatory behavior in time-resolved pump-probe Kerr rotation experiments in the Voigt geometry at $B = 0.5\,\mathrm{T}$, as shown in Figure 7.3. In this case, it is not necessary to satisfy the additional condition for the absence of Larmor precession, $|g_x\Omega_0| < |\gamma_\perp - \gamma_\parallel|$, which would require a small $|g_x| < 10^{-2}$ and an extremely long spin relaxation time of $\hbar/\gamma_\parallel \approx 150\,\mu\mathrm{s}$ [24, 25, 122]. For a realistic spin relaxation time of $\hbar/\gamma_\parallel \approx 1\,\mu\mathrm{s}$, it is estimated that $|g_x| \approx \delta g_x \approx 0.1$.

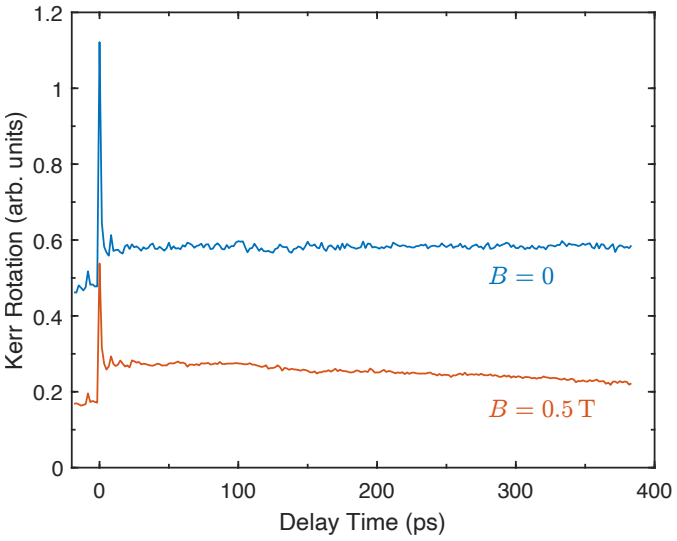

Figure 7.3: Time-resolved Kerr rotation measurements are performed in the Voigt geometry for $B = 0$ and 0.5 T. The circularly polarized pump beam has a photon energy of $\hbar\omega_{\mathrm{pump}} = 1.675\,\mathrm{eV}$, while the linearly polarized probe beam has a photon energy of $\hbar\omega_{\mathrm{probe}} = 1.636\,\mathrm{eV}$. The Kerr rotation angle of the probe beam is measured using balanced detection with a photodiode.

7.3 Summary

The spin dynamics in weak magnetic fields is governed by localized resident electrons, as evidenced by data analysis and supported by several factors. Despite the strong spin-orbit splitting, equivalent to an effective magnetic field of approximately 100 T acting on the electrons, a small external magnetic field of just 1 mT is sufficient to induce depolarization or polarization recovery of resident electron spins.

Spin-conserving intervalley scattering is suppressed because the electrons do not occupy the higher-energy states $K\downarrow$ and $K'\uparrow$, thereby precluding their involvement in the dynamical averaging of Ω_{SO}. The observation that the Hanle and polarization recovery curves exhibit comparable widths is similar to the behavior of donor-bound electrons in bulk GaAs, where spin relaxation is dominated by random nuclear fields [123].

In 2D monolayers, the g-factor and spin relaxation are highly anisotropic compared to bulk semiconductors. The model necessitates a non-zero intervalley in-plane g-factor for the electrons, which is achievable if they are localized within the layer. Localization reduces the spatial symmetry and induces mixing between the $K\uparrow$ and $K'\uparrow$ states, as well as between the $K\downarrow$ and $K'\downarrow$ states. This symmetry breaking is random, causing significant fluctuations in the magnitude of the in-plane g-factor, which manifests as spin dephasing without Larmor spin precession in pump-probe experiments.

The single-laser beam technique is used to study the spin dynamics in transition metal dichalcogenides and shows that localized electrons significantly influence the spin behavior

in 2D monolayers. In the investigated $MoSe_2$/EuS structure, spin relaxation is driven by random effective fields due to contact spin interactions, such as hyperfine interactions with the nuclei in $MoSe_2$ or exchange interactions with the magnetic ions of EuS.

These localized electrons exhibit not only anisotropic spin relaxation but also a nonzero out-of-plane g-factor due to the mixing of split-off bands with identical spins. The in-plane g-factor fluctuates significantly, comparable in magnitude to its mean value, accounting for the absence of oscillatory behavior in the spin dynamics transients. Further research is necessary to determine the precise origin and magnitude of these random fields.

8 Spin Dynamics of Excitons and Charge Carrier in Lead Halide Perovskite Semiconductors

This chapter is about the optical orientation of excitons and charge carriers in $FA_{0.9}Cs_{0.1}PbI_{2.8}Br_{0.2}$ and $MAPbI_3$ bulk lead halide perovskites. The samples are investigated by photoluminescence spectroscopy with time resolution described in Section 5.1, where streak image with time and spectral resolution gives access to the exciton signal. The optical properties are presented in Section 8.1.1 for $FA_{0.9}Cs_{0.1}PbI_{2.8}Br_{0.2}$ and 8.2.1 for $MAPbI_3$. The photoluminescence measured time-integrated and time-resolved regimes and the reflectivity spectrum shows the exciton absorption resonance. The spectrally resolved image from the streak camera allows the isolation of the exciton signal. The exciton recombination time is analyzed from the PL dynamics. The dynamics of the optical orientation of exciton spins in $FA_{0.9}Cs_{0.1}PbI_{2.8}Br_{0.2}$ and its dependence on excitation photon energy (energy detuning), temperature and transverse magnetic field is presented in Section 8.1.2. The dependence of the optical orientation on the excitation power is discussed in Section 8.1.3. The magneto-induced polarization of excitons in longitudinal magnetic fields is presented in 8.1.4 and the Landé factor $g_{F,X}$ is evaluated from the spectral shift of the exciton PL in magnetic field. The spin coherence of excitons in $FA_{0.9}Cs_{0.1}PbI_{2.8}Br_{0.2}$ is studied in transverse magnetic field, showing pronounced spin precession of excitons, electrons and holes, as shown in Section 8.1.5. By this method the g-factor of the exciton and charge carriers is evaluated.

For $MAPbI_3$, optical orientation degree is presented in Section 8.2.2 and the dependence of the optical orientation degree on excitation photon energy, power, temperature and transverse magnetic field in Section 8.2.3. The exciton spin polarization in longitudinal magnetic fields is presented in 8.2.4, where the Landé factor for $g_{F,X}$ is evaluated. The spin precession in magnetic field is analyzed in Section 8.2.5. It is measured by the optical orientation and gives access to the g-factor of electron and hole in transverse magnetic fields, and by exciting with circular polarized light and linear polarization detection with access to exciton g-factor in longitudinal and transverse magnetic fields.

The conclusion and summary is presented in Section 8.3.

The results of this chapter are published in [72], [125] and [126].

8.1 Spin Dynamics of Excitons in $FA_{0.9}Cs_{0.1}PbI_{2.8}Br_{0.2}$ Bulk Crystal

8.1.1 Optical Properties

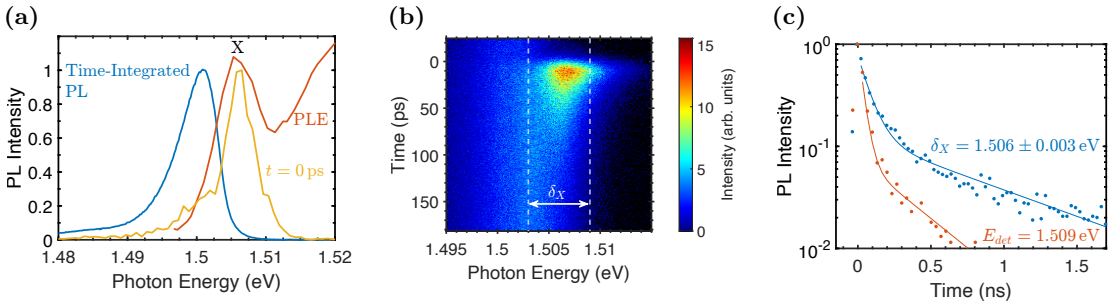

Figure 8.1: The photoluminescence (PL) spectrum, streak image, and PL dynamics in bulk $FA_{0.9}Cs_{0.1}PbI_{2.8}Br_{0.2}$ crystal are presented. Figure 8.1a shows the time-integrated photoluminescence spectrum (blue line) with excitation photon energy at $E_{exc} = 1.669\,eV$, using a laser excitation power of $P_{exc} = 0.1\,mW$ and the temperature of $T = 1.6\,K$. The photoluminescence excitation spectrum (red line) is detected at $E_{det} = 1.496\,eV$. The exciton resonance is denoted by X. The PL spectrum at the moment of excitation ($t = 0\,ps$) for pulsed excitation is shown by the yellow line. A streak image of time-resolved photoluminescence with the exciton ROI δ_X is shown in Figure 8.1b, excited by 200 fs laser pulses. In Figure 8.1c the recombination dynamics is shown. They are detected at $E_{det} = 1.509\,eV$ (red) and integrated over the spectral range from 1.503 eV to 1.509 eV around the exciton line maximum at $E_X = 1.506\,eV$ (blue). The lines represent bi-exponential fits with decay times of $\tau_{R1} = 55\,ps$ and $\tau_{R2} = 840\,ps$ for $E_{det} = 1.506\,eV$, and $\tau_{R1} = 35\,ps$ and $\tau_{R2} = 380\,ps$ for $E_{det} = 1.509\,eV$.

In this study, a bulk single crystal of $FA_{0.9}Cs_{0.1}PbI_{2.8}Br_{0.2}$ hybrid organic-inorganic lead halide perovskite is selected due to its high structural quality and minimal inhomogeneous broadening of the exciton resonance. The crystal maintains cubic lattice symmetry even at cryogenic temperatures, as confirmed by the isotropic electron and hole g-factors measured at $T = 1.6\,K$ [49].

The optical properties of the crystal are illustrated in Figure 8.1, with additional details provided in the References [49, 51, 52, 127]. At $T = 1.6\,K$, the exciton resonance is observed at 1.506 eV in the photoluminescence excitation (PLE) spectrum (red line). The exciton binding energy is expected to be close to 14 meV for $FAPbI_3$ [128], resulting in a bandgap energy of $E_g = 1.520\,eV$ for the studied crystal. The time-integrated photoluminescence (PL) spectrum (blue line) was measured under pulsed excitation by CCD with a single lens ($f = 250\,mm$) focussing the laser beam on the sample and collecting the outcoming PL (see Section 5.1) with an excitation power of 0.1 mW. The PL exhibits a peak at 1.501 eV with a full width at half maximum of 5 meV. The recombination dynamics measured in ns time-range by time-of-flight PC board span a broad temporal range from 700 ps to 44 µs with significant spectral dispersion [72, Supp. Inf., Section S3], suggesting the presence of multiple recombination processes, including those involving spatially separated charge carriers [51].

The coherent spin dynamics of resident electrons and holes, following their optical orientation, demonstrate nanosecond-scale spin dephasing times in such crystals [51]. In this study, the focus is on the spin properties of excitons with short recombination times.

Time-resolved photoluminescence (TRPL), recorded using a streak camera, is employed to isolate the exciton signals. The PL dynamics are displayed as streak image in Figure 8.1b time and spectral resolution. Immediately after photogeneration at $t = 0\,\mathrm{ps}$, the emission exhibits a spectral maximum at 1.506 eV, matching the exciton resonance X in the PLE spectrum at $E_\mathrm{X} = 1.506\,\mathrm{eV}$ (see Figure 8.1a, PLE red line, $I(t = 0)$ yellow line). The spectrally integrated exciton emission (blue line in Figure 8.1c) shows a double-exponential decay. The fast decay time, $\tau_\mathrm{R1} = 55\,\mathrm{ps}$, is attributed to exciton recombination, while the longer time, $\tau_\mathrm{R2} = 840\,\mathrm{ps}$, corresponds to the recombination of spatially separated electrons and holes. Decay times are evaluated from the PL dynamics of the total intensity (proportional to the population) with multiple recombination times ($\tau_{\mathrm{R}i}$):

$$I(t) = \sum_i I_i(0) \exp\left(-\frac{t}{\tau_{\mathrm{R}i}}\right) \tag{8.1}$$

where $I_i(0)$ is the initial population of each component.

It is characteristic of lead halide perovskites that multiple recombination processes overlap spectrally, complicating the interpretation of the recombination and spin dynamics [48, 51]. The assignment of the τ_R2 time to the recombination of separated electrons and holes is confirmed by results from coherent spin dynamics in a magnetic field, as measured by time-resolved Kerr rotation in Reference [51], and in this study by time-resolved polarized emission, shown in Figure 8.5a. The dependencies of the exciton and electron-hole pair recombination times on temperature and excitation power are discussed in Section 8.1.3. It is important to note that the excitation power of 0.1 mW corresponds to a relatively low exciton density of approximately $10^{13}\,\mathrm{cm}^{-3}$, ensuring that exciton-exciton interactions can be neglected.

The red line in Figure 8.1c shows the PL dynamics measured at 1.509 eV, corresponding to the high-energy wing of the exciton line. The dynamics at this energy, with values $\tau_\mathrm{R1} = 35\,\mathrm{ps}$ and $\tau_\mathrm{R2} = 380\,\mathrm{ps}$, are faster than those obtained by integrating over the exciton line, indicating that energy relaxation of excitons contributes to the spectral dependence of their dynamics. This behavior has been demonstrated recently for $FA_{0.9}Cs_{0.1}PbI_{2.8}Br_{0.2}$ crystals using transient photon echo spectroscopy [127]. The PL dynamics exhibit two contributions: one from exciton recombination and another from electron-hole pair recombination (Figure 8.1c). Although these contributions spectrally overlap, they can be distinguished in the time domain.

To focus on the exciton spin dynamics in polarization-resolved measurements, the recombination dynamics are integrated in the energy range of $\delta_\mathrm{X} = (1.506 \pm 0.003)\,\mathrm{eV}$ around the exciton line maximum at $E_\mathrm{X} = 1.506\,\mathrm{eV}$, using temporally and spectrally resolved PL (blue line in Figure 8.1c).

8.1.2 Optical Orientation of Exciton Spins

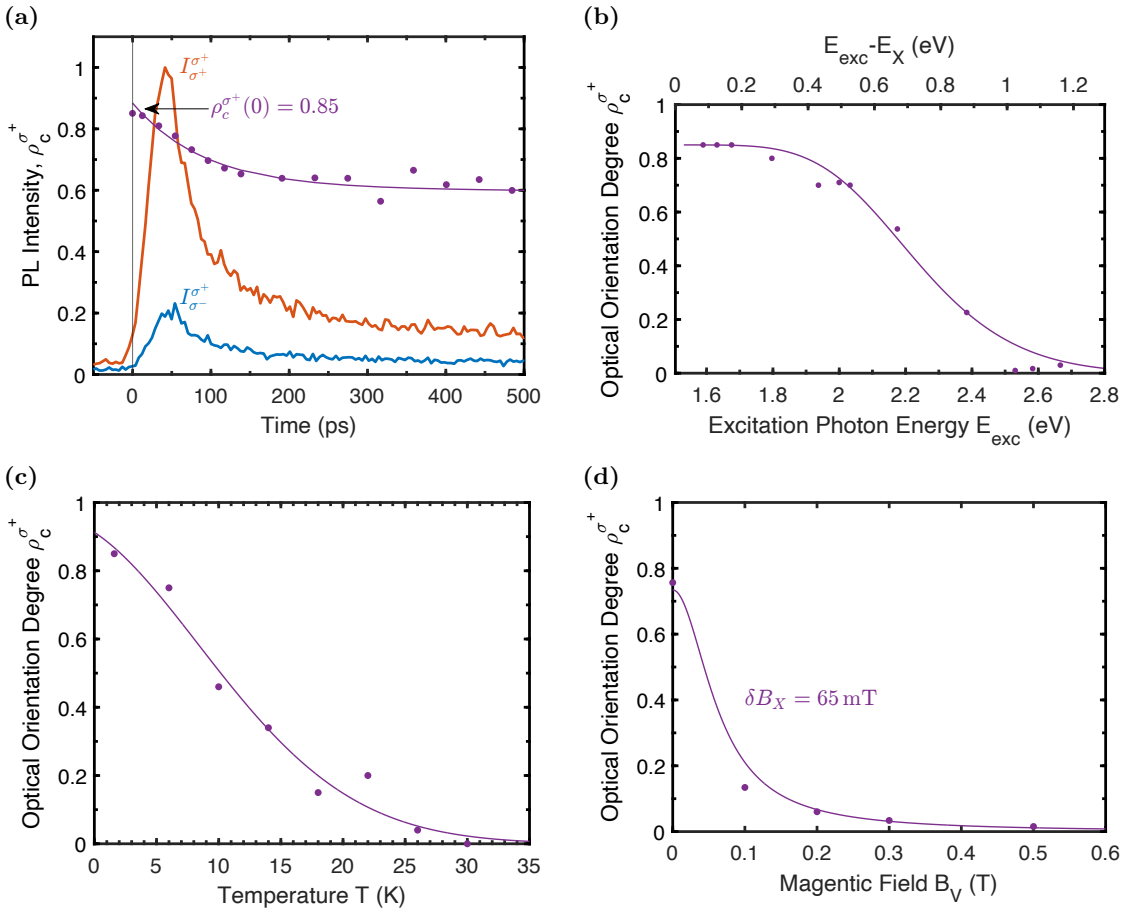

Figure 8.2: Optical orientation of exciton spins has been recorded at the exciton energy of 1.506 eV. Figure 8.2a shows the photoluminescence (PL) dynamics that is detected in σ^+ (red line) and σ^- (blue line) polarization under σ^+ excitation at $E_{\mathrm{exc}} = 1.669\,\mathrm{eV}$, with a laser excitation power of 0.1 mW at $T = 1.6\,\mathrm{K}$. The violet dots are showing the corresponding dynamics of the optical orientation degree $\rho_c^{\sigma^+}(t)$. An exponential fit (violet line) between the 0.85 and 0.60 levels yields a decay time of 100 ps. Figure 8.2b shows the dependence of $\rho_c^{\sigma^+}(t = 0)$ on the excitation energy E_{exc} (dots), with the upper axis showing the detuning from the exciton resonance, $E_{\mathrm{exc}} - E_{\mathrm{X}}$. The violet line shows the theoretical curve P^{SR}, calculated considering Elliott-Yafet spin relaxation due to interaction with longitudinal optical phonons [72, Supp. Inf.]. Figure 8.2c shows the temperature dependence of $\rho_c^{\sigma^+}(t = 0)$ (dots), with the line serving as a guide to the eye. Figure 8.2d shows the dependence of $\rho_c^{\sigma^+}$ on the magnetic field applied in Voigt geometry (B_{V}) for σ^+ excitation at $E_{\mathrm{exc}} = 1.675\,\mathrm{eV}$ with $P_{\mathrm{exc}} = 0.3\,\mathrm{mW}$ at $T = 1.6\,\mathrm{K}$. Each point is obtained by integrating the PL dynamics over 6 ps. The line represents a fit using Equation (8.3) with $\delta B_{\mathrm{X}} = 65\,\mathrm{mT}$.

The dynamics of the σ^+ and σ^- circularly polarized photoluminescence (PL) intensity excited with σ^+ polarized pulses and the optical orientation $\rho_c^{\sigma^+}$ (see Equation (6.4)) are shown in Figure 8.2a. The strong difference in their amplitudes, favoring the σ^+ polarized signal, reveals a large degree of optical orientation.

The initial value of $\rho_c^{\sigma^+}$ reaches 0.85 (85 %), dropping within the 100 ps to a saturation

level of 0.60 (60 %) with almost no further decay. Typically, the decay of $\rho_c^{\sigma^+}(t)$ is attributed to spin relaxation. In this case both excitons and electron-hole recombination contribute to $\rho_c^{\sigma^+}$, and the exciton spin relaxation time exceeds the exciton lifetime τ_X (detailed in Section 8.1.3). Initially, the contribution to $\rho_c^{\sigma^+}(t)$ comes primarily from excitons. Following exciton recombination, the PL signal is dominated by long-lived carriers with $\rho_c^{\sigma^+} = 0.60$. Therefore, the decay of $\rho_c^{\sigma^+}$ from 0.85 to 0.60 is determined by the exciton lifetime.

A detailed analysis of optical orientation for electrons and holes is provided in Reference [129]. Assuming, in agreement with the experiment, that the lifetime and spin relaxation time of electrons and holes far exceed the exciton lifetime, the limiting value of the circular polarization degree is given by (see Section 2.5, Equation (2.20))

$$\rho_c^{\sigma^+}(t \gg \tau_X, \tau_s) = \frac{\tau_s}{\tau_X + \tau_s} \rho_c^{\sigma^+}(t = 0) \tag{8.2}$$

where τ_s is the exciton spin relaxation time and τ_X is the exciton lifetime. The initial polarization value $\rho_c^{\sigma^+}(0)$ is limited by the maximum $\rho_{c,\max}^{\sigma^+} = 1$ (100 %), which is determined by the band structure for optical transitions at the absorption edge. Taking $\tau_X = \tau_{R1} = 55$ ps and $\rho_c^{\sigma^+} = 0.85$ from the experiment, the exciton spin relaxation time is estimated as $\tau_s = 220$ ps.

A high degree of initial optical orientation is also observed for a substantial detuning of the laser energy from the exciton resonance $E_{exc} - E_X = 0.163$ eV. This result is attributed to the strict selection rules for optical transitions between the involved bands, which exhibit low mixing and are not affected by the Dyakonov-Perel mechanism in the cubic crystal phase of the perovskite material. In contrast, in conventional III-V and II-VI semiconductors with zinc-blende crystal structures, a high $\rho_c^{\sigma^+}$ is observed only for resonant or near-resonant excitation due to: firstly, the fitting of strict selection rules caused by band mixing, and secondly, the effective Dyakonov-Perel mechanism, which accelerates spin relaxation in charge carriers with high kinetic energy [28, 42, 130].

The dependence of initial exciton spin polarization on excess energy in $CsPbBr_3$ nanoplatelets is reported in Reference [57] and attributed to spin relaxation effects. However, at low temperatures, size quantization of electrons and holes in nanoplatelets leads to fundamentally different spin relaxation mechanisms unrelated to spin-orbit interactions [42, 130]. At higher temperatures, spin relaxation is driven by interactions between charge carriers and phonons [131].

The excitation energy detuning of $\rho_c^{\sigma^+}(0)$ is presented for a wide range from 0.8 eV up to 1.2 eV in Figure 8.2b. The value of 0.85 is maintained up to a detuning of 0.3 eV that is decreasing to zero at 1.05 eV. These detunings are far greater than the exciton binding energy, so photogenerated electrons and holes rapidly separate due to their opposite momenta. Thus, direct formation of excitons from photogenerated electron-hole pairs is unlikely. Instead, the carriers relax within a few picoseconds to the conduction band minimum and the valence band maximum, where they may either form excitons or become localized, from which they recombine as spatially separated carriers at cryogenic temperatures.

The high value of $\rho_c^{\sigma^+}$ for excitons indicates three points: first, chiral selection rules are obeyed not only at the absorption edge but also for large detunings, second, carriers retain their spin polarization during energy relaxation, and third, when bound to an exciton near the bandgap, they exhibit negligible spin relaxation during the exciton lifetime at $T = 1.6$ K. The preservation of chiral selection rules and the absence of efficient spin-flip events in charge carriers are supported by atomistic modeling [72].

It is also noted that significant optical orientation implies not only strict selection rules but also suppressed spin relaxation, which indirectly suggests the presence of an inversion center of symmetry in the sample. Otherwise, momentum-dependent spin-orbit splitting associated with inversion asymmetry would cause efficient spin depolarization via the Dyakonov-Perel mechanism [42, 131].

The depolarization in a transverse magnetic field in Voigt geometry ($B_V \perp k$) via the Hanle effect (Figure 8.2d) yields a similar exciton spin relaxation time of 300 ps. The Hanle effect is analyzed by investigating the contributions of resident electrons and holes and excitons. The Hanle contribution of long-lived charge carriers can be described by established expressions, such as in [28, 130]. Given the long spin relaxation times of electrons and holes, their Hanle curves are extremely narrow with about 4 mT for electrons and 18 mT for holes [129]. The contribution of the free charge carriers to $\rho_c^{\sigma^+}(B_V)$ is not observable within the experimental magnetic field range up to 0.5 T.

To focus on the contribution of the excitons, the intensities $I_{\sigma^+}^{\sigma^+}$ and $I_{\sigma^-}^{\sigma^+}$ were integrated over a time scale up to 600 ps, which is beyond the exciton lifetime, but much shorter than the spin relaxation time of the charge carriers. This integration yielded $\rho_c^{\sigma^+}(B_V)$ values, which are shown in Figure 8.2d. It is assumed that the exchange interaction of the exciton is dominant within the relevant field range ($B_V \leq 100$ mT). The Hanle curve is can be expressed by combining equation of the Larmor precession (3.3) and steady-state polarization from Equation (3.8) in (3.9)

$$\rho_c^{\sigma^+}(B_V) = \frac{\tau_s}{\tau_X + \tau_s} \cdot \frac{\rho_c^{\sigma^+}(t=0)}{1 + \left(\mu_B g_{V,X} B_V \frac{T_s}{2\hbar}\right)^2}, \tag{8.3}$$

where T_s represents the exciton spin lifetime (see Equation (3.10)):

$$T_s = \frac{\tau_X \tau_s}{\tau_X + \tau_s}, \tag{8.4}$$

where τ_s is the spin relaxation time of the exciton and $\rho_c^{\sigma^+}(0)$ is the optical orientation degree in the zero field. This equation approximates the Hanle profile either for continuous wave excitation or for cases where T_s is significantly shorter than the integration time of the time-resolved photoluminescence signals (TRPL). In this scenario, the steady state $\rho_c^{\sigma^+}$ at zero magnetic field simplifies to Equation (8.2). By adjusting $\rho_c^{\sigma^+}(B_V)$ to Equation (8.3), a half-width at half-maximum (HWHM) of $\delta B_X = 65$ mT and an exciton spin lifetime $T_s = 150$ ps is obtained using $g_{V,X} = 2.3$. The estimation of T_s from the half-width of the Hanle curve is only approximate, since the expression assumes an experimental integration time which is much longer than the actual spin lifetime.

The Hanle curve width $\delta B_X = 65$ mT corresponds to $T_s = 75$ ps. With an exciton lifetime $\tau_X = 85$ ps, measured at an excitation power of $P_{exc} = 0.3$ mW, a carrier spin relaxation time of $\tau_s = 300$ ps is estimated. The essential value of $\rho_c^{\sigma^+} = 0.6$, which remains constant from 100 ps to 500 ps (and has been measured up to 2 ns), indicates remarkably long spin relaxation times for electrons and holes (at least for one type of carrier, probably for both). Using the lower limit of the electron-hole recombination time $\tau_{R2} = 840$ ps, the spin relaxation time of the charge carriers is set to $\tau_{s,e/h} \geq 1.5 \cdot \tau_{R2} = 1260$ ps.

Additionally, a strong temperature dependence of $\rho_c^{\sigma^+}$ is observed Figure 8.2c, with polarization disappearing at temperatures above 30 K, which is attributed to thermally activated spin relaxation of excitons and free carriers, and their interaction with phonons [51, 131, 132].

8.1.3 Effect of Excitation Power

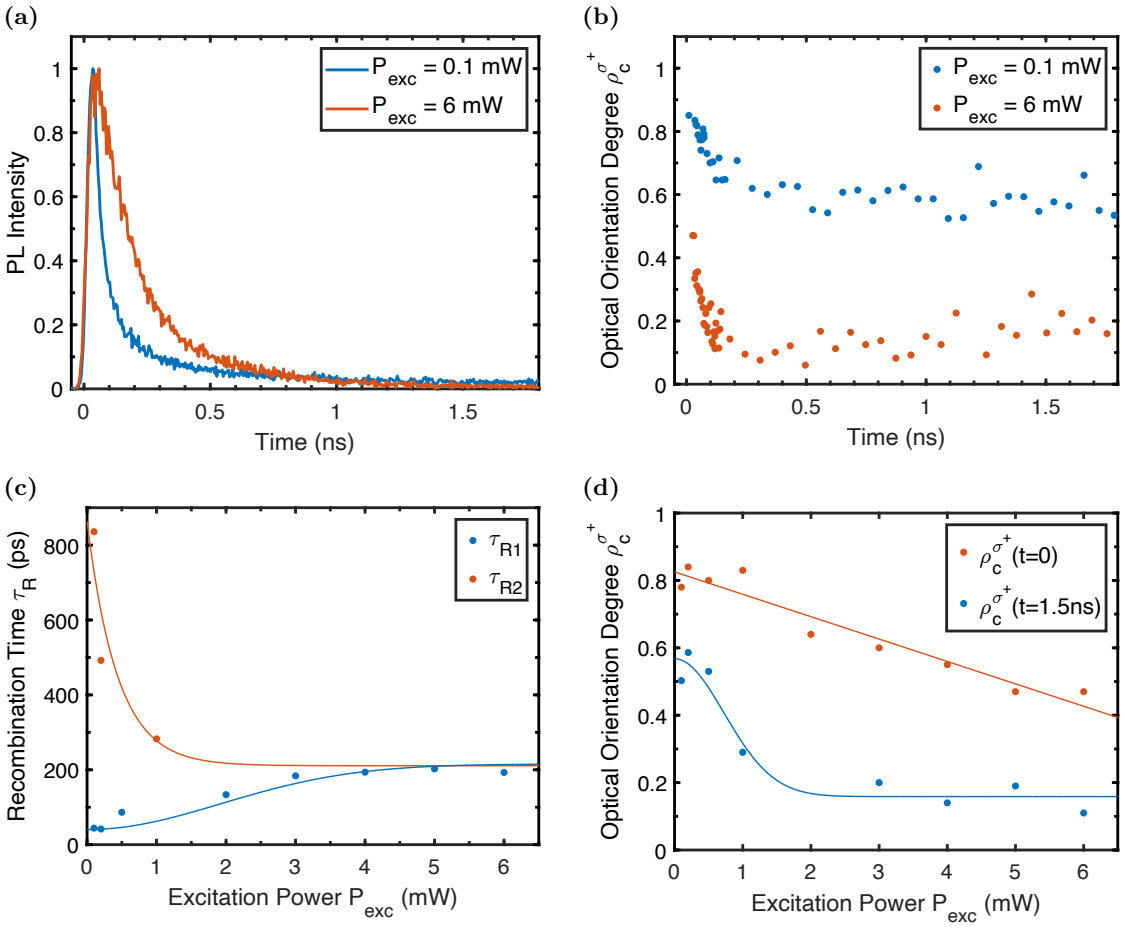

Figure 8.3: Figure 8.3a shows TRPL intensity signals measured for excitation power $P_{\mathrm{exc}} = 0.1\,\mathrm{mW}$ (blue line) and $P_{\mathrm{exc}} = 6\,\mathrm{mW}$ (red line), with conditions of $T = 1.6\,\mathrm{K}$, $E_{\mathrm{det}} = 1.506\,\mathrm{eV}$, and $E_{\mathrm{exc}} = 1.675\,\mathrm{eV}$. Figure 8.3b shows time-resolved $\rho_c^{\sigma^+}$ recorded for $P = 0.1\,\mathrm{mW}$ (blue dots) and $P = 6\,\mathrm{mW}$ (red dots). Figure 8.3c presents the dependence of τ_{R1} (blue dots) and τ_{R2} (red dots) on the excitation power, with lines serving as guides to the eye. Figure 8.3d shows the optical orientation of excitons (measured at $t = 0\,\mathrm{ns}$, blue dots) and localized carriers (measured at $t = 1.5\,\mathrm{ns}$, red dots) as a function of excitation power P_{exc}, with lines serving as guides to the eye.

Experimental results on the modification of recombination and spin dynamics of excitons and resident carriers with increasing excitation power are presented in Figure 8.3. These results provide insights into the interplay between exciton and carrier contributions to the emission at a spectral energy of 1.506 eV. It is shown that in this case the dynamics of the optical orientation degree is not determined by the spin relaxation time, as is typical when only a single recombination process is involved, but by the fast recombination of excitons. This situation is rather unusual in the context of semiconductor spin physics, and a corresponding discussion in the literature has not been found so far.

The excitation power of 0.1 mW corresponds to an exciton density of approximately $10^{13}\,\mathrm{cm}^{-3}$. At such low densities, the interaction between excitons can be neglected. The exciton-exciton interactions may become significant at higher excitation densities,

particularly in nanostructures [57, 133]. Results for recombination and $\rho_c^{\sigma^+}(t)$ dynamics, measured across a wide range of excitation power from 0.1 mW to 6 mW, are shown in Figure 8.3.

Figure 8.3a compares the recombination dynamics for excitation densities of 0.1 mW (blue line) and 6 mW (red line). With increasing excitation power the initial decay slows, and the decay time increases from 55 ps to 200 ps. The slow contribution to the dynamics accelerates, with the corresponding decay time decreasing from 840 ps to 200 ps. A redistribution of intensity between the fast and slow components is also observed. At $P_{\text{exc}} = 6$ mW the initial decay of PL intensity, approximately 95 %, becomes mono-exponential, with a decay time of 200 ps.

The dependencies of the recombination times τ_{R1} and τ_{R2} on excitation power P_{exc} are shown in Figure 8.3c. The longer recombination time, τ_{R2}, is attributed to the recombination of spatially separated electrons and holes. As the concentrations of these carriers increase at higher excitation densities, their separation reduces, leading to faster recombination. The increase in τ_{R1} with rising excitation power is proposed to indicate an increasing contribution of spatially separated electrons and holes compared to exciton recombination. At higher excitation densities, PL dynamics are predominantly associated with electron-hole recombination.

Figure 8.3b shows the dynamics of optical orientation degree $\rho_c^{\sigma^+}(t)$ measured at $P_{\text{exc}} = 0.1$ mW and 6 mW. The $\rho_c^{\sigma^+}(t)$ dependence at $P_{\text{exc}} = 0.1$ mW (blue dots) is the same as shown in 8.2a but extended to a longer time range up to 1.8 ns, demonstrating an almost negligible decay of polarization over the entire period. At the initial time after excitation, $\rho_c^{\sigma^+}(t = 0)$ reaches 0.85, then decreases and saturates at about 0.60. The transition takes approximately 55 ps, matching the exciton lifetime measured in the recombination dynamics $\tau_{\text{X}} = 55$ ps. The dynamics of $\rho_c^{\sigma^+}(t)$ reflect the recombination of excitons with a high optical orientation degree of 0.85, and at later times, the degree of orientation is determined by the smaller values typical for resident carriers. This is an unusual case in which the dynamics of $\rho_c^{\sigma^+}(t)$ is determined by the recombination time and not by the spin relaxation time.

At the maximum excitation power of $P_{\text{exc}} = 6$ mW, the initial optical orientation decreases to $\rho_c^{\sigma^+}(t = 0) = 0.50$. Over a time interval of 150 ps, the polarization drops to a saturation level of approximately 0.15 (red dots in Figure 8.3b). The power dependencies of $\rho_c^{\sigma^+}(t = 0)$ and $\rho_c^{\sigma^+}(t = 1.5\,\text{ns})$ are shown in Figure 8.3d. The initial degree of polarization decreases with increasing excitation power from 0.85 down to 0 while the degree at longer delays, which is attributed to resident carriers, exhibits the largest decrease from 0.60 to 0.20 up to excitation power of 0.1 mW. The reduction in the saturation level is related to the increase in the short exciton recombination time τ_{R1} according to Equation (8.2). At low excitation power, the factor $\nu = \tau_{\text{s}}/(\tau_{\text{X}} + \tau_{\text{s}}) \approx 0.8$ (from experimental data) is consistent with $\tau_{\text{X}} = \tau_{\text{R1}} = 55$ ps and $\tau_{\text{s}} = 220$ ps, as discussed in Section 8.1.2. This explains the reduction of $\rho_c^{\sigma^+}$ from 0.85 to 0.60, while at higher pump power, $\nu \approx 0.5$ corresponds to $\tau_{\text{X}} = \tau_{\text{R1}} = 200$ ps. Additional factors, such as a reduction in exciton spin relaxation time at higher excitation power, cannot be excluded.

The experiments are conducted with the sample in direct contact with superfluid liquid helium. It is expected that lattice heating effects are negligible across the entire power range used, although the exciton and carrier temperatures may be elevated. If the reduction of $\rho_c^{\sigma^+}$ at higher excitation power is due to local heating by the laser, then $\rho_c^{\sigma^+}(t = 0) = 0.5$ at 6 mW would correspond to a temperature of 10 K, based on the temperature dependence shown in Figure 8.2c. The exciton recombination time at 10 K does not increase compared to that at 1.6 K and remains around 60 ps. At 1.6 K and

6 mW, the recombination time is 200 ps. From this it can be concluded that the increase in pump fluence does not contribute significantly to sample heating. This observation is consistent with the absence of wave-vector-dependent Rashba and Dresselhaus term. Otherwise, an enhancement of spin relaxation with increasing temperature would be expected.

8.1.4 Polarization of Bright Excitons in Longitudinal Magnetic Field

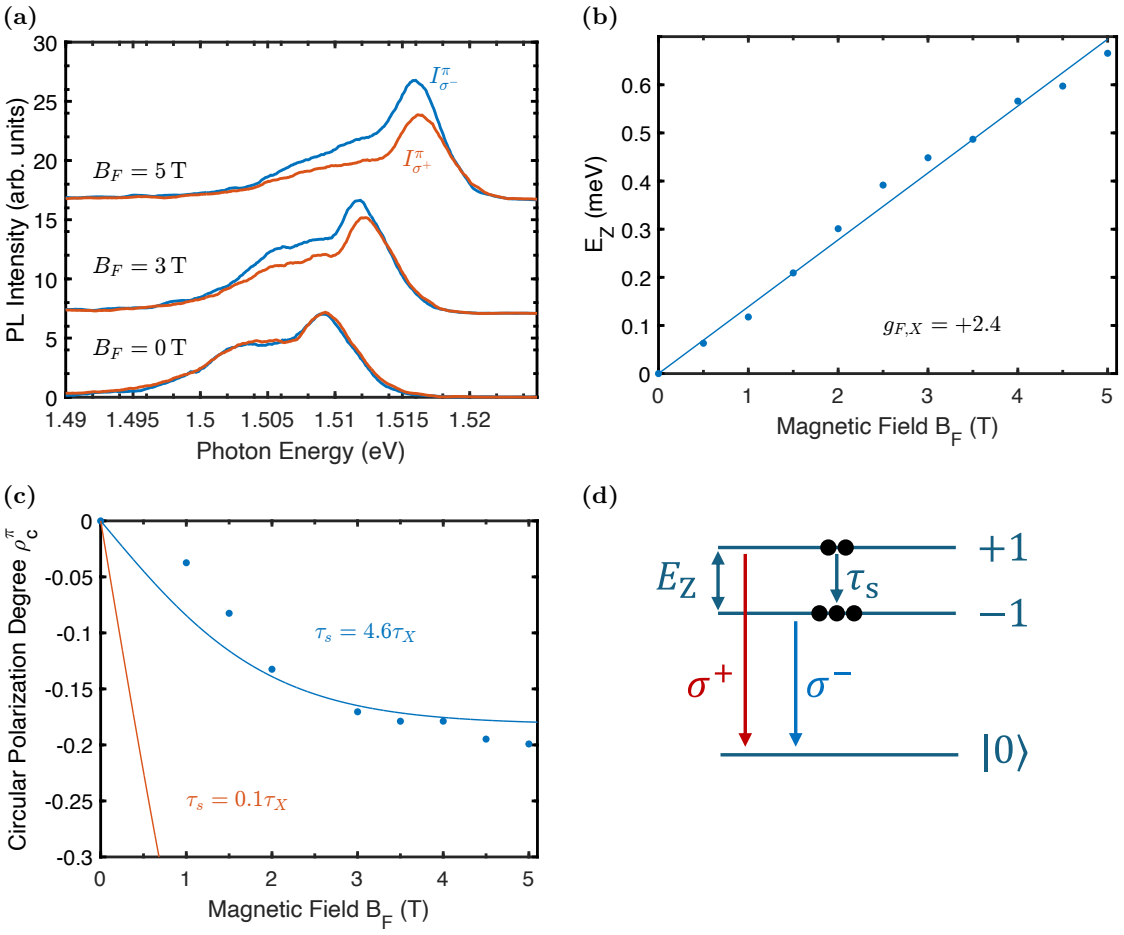

Figure 8.4: The exciton Zeeman splitting and polarization in a longitudinal magnetic field at $T = 1.6\,K$. Figure 8.4a shows the photoluminescence (PL) spectra integrated over the exciton lifetime τ_X for σ^+ (red) and σ^- (blue) polarizations in a longitudinal magnetic fields $B_F = 0\,T$, $3\,T$ and $5\,T$. The excitation is performed using a linearly polarized laser at $E_{exc} = 1.669\,eV$ with an excitation power of $P_{exc} = 0.1\,mW$. Figure 8.4b presents the exciton Zeeman splitting as a function of B_F (dots). A linear fit to the data gives a Landé factor of $g_{F,X} = +2.4$ (line). Figure 8.4c shows the degree of circular polarization as a function of B_F (blue dots). The blue line represents a fit using Equation (8.6) with $T = 1.6\,K$ and $\tau_s = 4.6\tau_X$. For comparison, the red line shows the calculated result for the condition $\tau_s = 0.1\tau_X$ at $T = 1.6\,K$. Figure 8.4d shows the schematically drawing of the population of the excitons on their Zeeman split spin sublevels and the resulting polarized emission. The crystal ground state is represented by $|0\rangle$.

To investigate the spin dynamics of excitons in their ground state, independently of the spin dynamics of carriers at higher energies, the degree of circular polarization induced by a magnetic field applied in the Faraday geometry $\rho_c^\pi(B_\mathrm{F})$ is analyzed under linearly polarized excitation. The polarized photoluminescence (PL) spectra as function of the photon energy, integrated over the exciton lifetime, are presented in Figure 8.4a. The exciton peak at 1.506 eV exhibits Zeeman splitting of the bright (optically active) exciton states with angular momentum z-components $J_z = \pm 1$ and can be expressed by combining Equation (3.2) and (3.3) as

$$E_\mathrm{Z} = \mu_\mathrm{B} g_\mathrm{X} B \tag{8.5}$$

where g_X is the exciton g-factor and μ_B is the Bohr magneton. The magnetic field dependence of the Zeeman splitting, shown in Figure 8.4b, yields a value of $g_\mathrm{F,X} = +2.4$, which is consistent with known values for $FA_{0.9}Cs_{0.1}PbI_{2.8}Br_{0.2}$ [52]. The positive sign of g_X corresponds to the lower-energy sublevel having σ^- polarization, as illustrated in Figure 8.4d. A detailed investigation of bright exciton g-factors in lead halide perovskites has been conducted in Reference [52] using magneto-reflectivity methods. The exciton g-factor is isotropic and remains relatively constant over a wide bandgap energy range from 1.5 to 3.2 eV.

Figure 8.4a shows the PL emission becomes circularly polarized in the presence of a magnetic field, with stronger emission in σ^- polarization for $B_\mathrm{F} > 0$, indicating a higher population of the lower-energy Zeeman sublevel (see Figure 8.4d). The circular polarization degree ρ_c^π is calculated as referred in Equation (6.1) in Section 6.2. The dependence of ρ_c^π on B_F is shown in Figure 8.4c. The magnitude of the circular polarization degree increases linearly at small magnetic fields and saturates at $\rho_c^\pi = -0.20$ at $B_\mathrm{F} = 5\,\mathrm{T}$. This behavior for the circular polarization degree is typical for excitons thermalizing between Zeeman sublevels and is described by (see Equation (3.17) in Section 3.4.1)

$$\rho_c^\pi(B_\mathrm{F}) = -\frac{\tau_\mathrm{X}}{\tau_\mathrm{X} + \tau_\mathrm{s}} \tanh\left(\frac{g_\mathrm{F,X}\mu_\mathrm{B}B_\mathrm{F}}{2k_\mathrm{B}T}\right). \tag{8.6}$$

The experimental data are fitted using this equation with $T = 1.6\,\mathrm{K}$ and $\tau_\mathrm{X} = 55\,\mathrm{ps}$, as shown by the blue line in Figure 8.4c. The fit yields a spin relaxation time of $\tau_\mathrm{s} = 4.6\tau_\mathrm{X} = 250\,\mathrm{ps}$, which is close to the $\tau_\mathrm{s} = 220\,\mathrm{ps}$ obtained from optical orientation measurements. Notably, the longer spin relaxation time relative to the exciton lifetime results in two key effects: first, a significant reduction in circular polarization degree ρ_c^π compared to the fully thermalized case ($\tau_\mathrm{s} \ll \tau_\mathrm{X}$), represented by the red line in Figure 8.4c, and second, higher values of optical orientation $\rho_c^{\sigma^+}$, as described by Equation (8.2).

8.1.5 Spin Precession in Transverse Magnetic Field

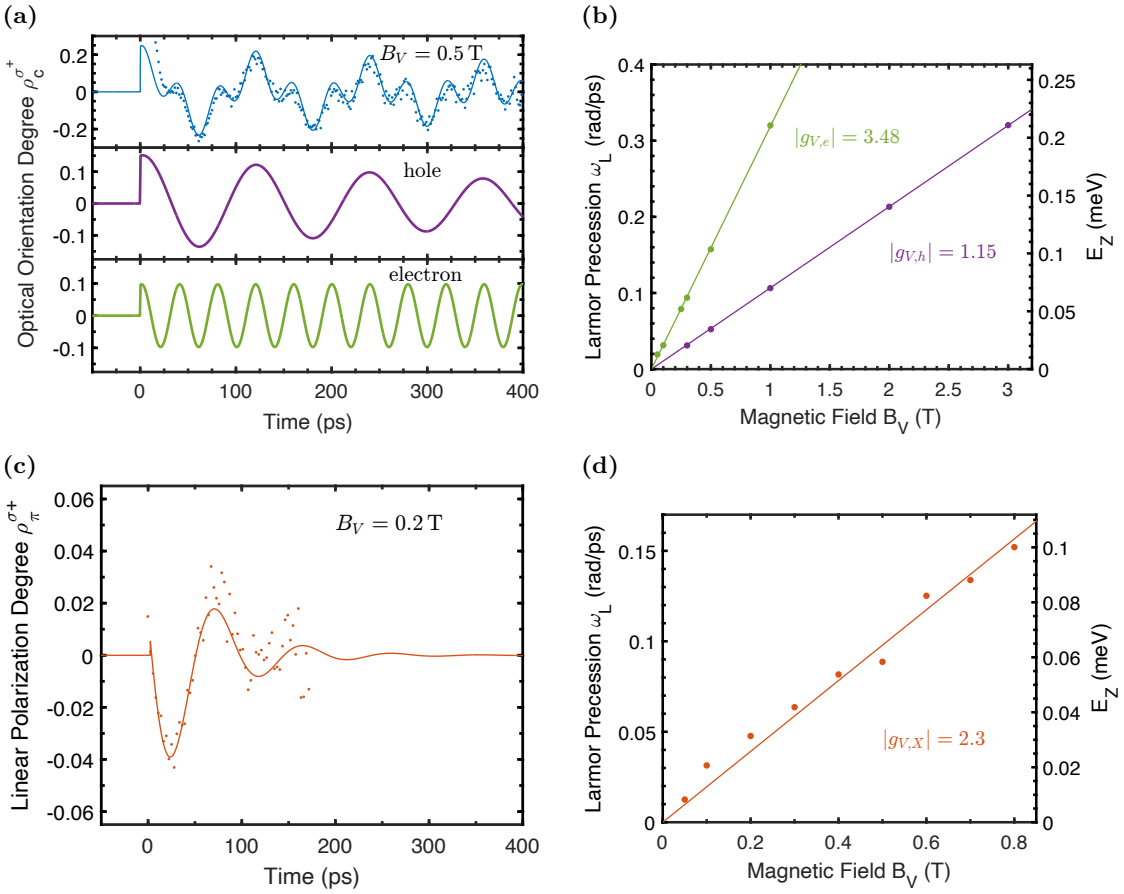

Figure 8.5: The spin precession of excitons and resident carriers in a magnetic field applied in Voigt geometry measured by time-resolved photoluminescence (TRPL) at $T = 1.6$ K. Figure 8.5a shows the dynamics of the optical orientation degree $\rho_c^{\sigma^+}(t)$ measured at $B_V = 0.5$ T using σ^+ excitation at $E_{exc} = 1.675$ eV with $P_{exc} = 0.3$ mW (dots), with detection at $E_{det} = E_X = 1.506$ eV. The blue line represents a fit using Equation (8.7), which includes contributions from both electrons and holes, shown by the violet and green lines, respectively. Figure 8.5b presents the dependence of the Larmor precession frequencies for electrons (green dots) and holes (violet dots) on B_V. Linear fits yield $|g_{V,e}| = 3.48$ and $|g_{V,h}| = 1.15$. Figure 8.5c shows the dynamics of the linear polarization degree $\rho_\pi^{\sigma^+}(t)$ measured at $B_V = 0.2$ T using σ^+ polarized excitation (red dots). The fit (red line) is performed using Equation (8.9) with $\omega_{L,X} = 0.048$ rad ps^{-1} and $\tau_X = 55$ ps. Figure 8.5d shows the magnetic field dependence of the Larmor precession frequency from $\rho_\pi^{\sigma^+}(t)$ (dots). A linear fit yields $|g_{V,X}| = 2.3$. The corresponding Zeeman splitting is indicated on the right axis.

The spin dynamics can be further explored by applying a magnetic field in the Voigt geometry that is oriented perpendicular to the wave vector of the light ($B_V \perp k$). In this configuration, the spins of excitons and/or charge carriers, which are initially optically oriented along the k vector, are subject to undergo a Larmor precession around the magnetic field direction with a frequency given by Equation (3.3) $\omega_L = \frac{g\mu_B B_V}{\hbar}$. The resulting spin dynamics allows direct access to the g-factor and the spin dephasing

time τ_X, where the latter is extracted from the decay of the signal. Time-resolved photoluminescence (TRPL) can be used to determine the spin precession quantum beats of excitons and charge carriers through the circular and linear polarization degrees of the emission [134, 135, 136]. This is demonstrated in Figure 8.5a, where the dynamics of $\rho_c^{\sigma^+}(t)$ are measured for $B_V = 0.5\,T$ at the exciton energy ($E_{det} = E_X = 1.506\,eV$). A complex pattern of spin beats with a weak decay is observed over a time span of 400 ps. The dynamics of the optical orientation degree can be described by the sum of decaying oscillatory functions from Equation (3.14)

$$\rho_c^{\sigma^+}(t) = \sum_i \rho_c^{\sigma^+}(0)\cos(\omega_{L,i}t)\exp\left(-\frac{t}{\tau_{s,i}}\right) \tag{8.7}$$

with the spin polarization degree at zero time delay $\rho_c^{\sigma^+}(0)$ and the index i = e,h denotes the electron or hole component to the Larmor precession frequency $\omega_{L,i}$ and in the spin relaxation time $\tau_{s,i}$.

The decay time is significantly longer than the exciton lifetime, leading to the assignment of the signal to the coherent spin precession of resident carriers. The signal comprises two oscillating components, with Larmor frequencies corresponding to the g-factors of the electron ($|g_{V,e}| = 3.48$) and the hole ($|g_{V,h}| = 1.15$), as shown by the fits in Figure 8.5a. The magnetic field dependence of these Larmor frequencies is depicted in Figure 8.5b, consistent with time-resolved Faraday/Kerr rotation measurements on the same perovskite crystal [51]. The absence of any offset in the Zeeman splittings as $B_V \to 0$ confirms that the signal arises from pairs of spatially separated electrons and holes, where the exchange interaction is negligible. The evolution of $\rho_c^{\sigma^+}(t)$ is accurately modeled using the approach developed for the case where there is no splitting between the singlet and triplet exciton states ($\Delta_{exch,e\text{-}h} = 0$) (see Section 3.8).

The exciton PL in the Voigt geometry is linearly polarized when excited with circular polarization. The degree of linear polarization is defined as

$$\rho_\pi^{\sigma^+} = \frac{I_\perp^{\sigma^+} - I_\parallel^{\sigma^+}}{I_\perp^{\sigma^+} + I_\parallel^{\sigma^+}} \tag{8.8}$$

where $I_\perp^{\sigma^+}$ and $I_\parallel^{\sigma^+}$ are the PL intensities in the linear polarizations perpendicular and parallel to the magnetic field direction, respectively. The dynamics of $\rho_\pi^{\sigma^+}(t)$, measured at $B_V = 0.2\,T$, is shown in Figure 8.5c. The exciton Larmor precession in the degree of linear polarization is described by Equation (3.14)

$$\rho_\pi^{\sigma^+}(t) = \rho_\pi^{\sigma^+}(t=0)\cos(\omega_{L,X}t)\exp\left(-\frac{t}{\tau_X}\right). \tag{8.9}$$

The degree of polarization decays with a time constant $\tau_X = 55\,ps$, during which it precesses with a Larmor frequency of $|g_{V,X}| = 2.3$ (Figure 8.5d). This value is close to the exciton g-factor obtained from PL measurements, $g_{F,X} = +2.4$ (Figure 8.4b), and the sum of the carrier g-factors, $g_{V,e} + g_{V,h} = +2.33$.

These observations enable the spin beats detected in the linear polarization degree to be reliably attributed to the dynamics of the bright exciton states with $J_z = \pm 1$, which possess a finite exchange interaction ($\Delta_{exch,e\text{-}h} > 0$) (see Section 3.8). The linear polarization beats serve as a clear indication of electron-hole spin correlations. It is important to note that individual charge carrier spin polarization alone can only result

in circular polarization of the emission, while the linear polarization $\rho_\pi^{\sigma^+}$ is governed by the quantum mechanical average $\langle \hat{s}_x^{\mathrm{e}} \hat{s}_x^{\mathrm{h}} - \hat{s}_y^{\mathrm{e}} \hat{s}_y^{\mathrm{h}} \rangle$, where $\hat{s}^{\mathrm{e/h}}$ represent the electron and hole spin operators, and x and y label their in-plane components (see Section 3.8).

For a non-zero $\rho_\pi^{\sigma^+}$, a non-zero average of $\hat{s}_x^{\mathrm{e}} \hat{s}_x^{\mathrm{h}}$ or $\hat{s}_y^{\mathrm{e}} \hat{s}_y^{\mathrm{h}}$ must exist, implying the necessity of electron-hole spin correlation. Spin precession in the magnetic field leads to oscillations in $\rho_\pi^{\sigma^+}$. Therefore, the polarization of both electron and hole spins is required to generate linear polarization, contrasting with the case of circular polarization, which can arise from the recombination of a polarized carrier with an unpolarized one. The presence of such correlations is crucial for the generation of entangled electron-hole spin states (see Section 3.8). It is noteworthy that the beats in both circular and linear polarization can be excited highly non-resonantly, for instance, with a detuning $E_{\mathrm{exc}} - E_{\mathrm{X}} = 0.17\,\mathrm{eV}$.

8.2 Spin Dynamics of Excitons and Charge Carriers in $MAPbI_3$ Microcrystal

8.2.1 Optical Properties

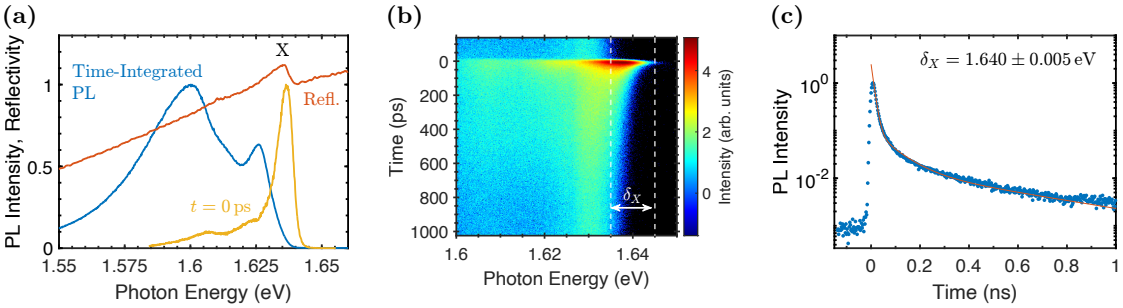

Figure 8.6: Figure 8.6a shows the time-integrated photoluminescence (PL) spectrum (blue) excited with a photon energy of $E_{\mathrm{exc}} = 1.771\,\mathrm{eV}$ and an excitation power of $P = 0.1\,\mathrm{mW}$, at $T = 1.6\,\mathrm{K}$. The reflectivity spectrum (red) is measured at $T = 7\,\mathrm{K}$ with a halogen lamp. The exciton resonance is marked by X. The yellow line shows the PL spectrum at $t = 0\,\mathrm{ps}$ at initial excitation integrated from the streak image. A streak image PL with the region of interest δ_{X} is shown in Figure 8.6b. Figure 8.6c shows the recombination dynamics, detected at the exciton resonance and integrated over the δ_{X} spectral range (dots). The red line corresponds to a fit with three exponential decay components, with decay times of $\tau_{\mathrm{R1}} = 15\,\mathrm{ps}$, $\tau_{\mathrm{R2}} = 85\,\mathrm{ps}$, and $\tau_{\mathrm{R3}} = 520\,\mathrm{ps}$.

The optical properties of the $MAPbI_3$ single microcrystal are shown in Figure 8.6a. The exciton resonance is observed at $E_{\mathrm{X}} = 1.636\,\mathrm{eV}$ at a temperature of $T = 1.6\,\mathrm{K}$. Given the exciton binding energy of bulk $MAPbI_3$ as 16 meV [128], the estimated band gap energy is $E_{\mathrm{g}} = 1.652\,\mathrm{eV}$. The time-integrated photoluminescence (PL) spectrum, obtained under pulsed laser excitation has a complex shape, with a high-energy peak at 1.627 eV and a full width at half maximum (FWHM) of 10 meV.

To clarify the origin of the emission lines, time-resolved photoluminescence measurements (TRPL) are carried out. The time- and spectrally-resolved PL is shown in Figure 8.6b as streak image. The spectral line at 1.627 eV has a long recombination time that exceeds the laser pulse repetition period of 12.5 ns. This long recombination time is attributed to the recombination of spatially separated electrons and holes, a property often observed in perovskite bulk structures [48, 49, 51, 137].

Immediately after optical excitation, the PL reaches its maximum at $E_{\mathrm{X}} = 1.636\,\mathrm{eV}$ (see Figure 8.6b and the yellow line in Figure 8.6a). This energy corresponds to the exciton resonance in the reflectivity spectrum. The spectrally integrated recombination dynamics over the exciton spectral range δ_{X} is shown in Figure 8.6c and extends up to 1 ns. The dynamics show a triple exponential decay. The two fast decay components with times $\tau_{\mathrm{R1}} = 15\,\mathrm{ps}$ and $\tau_{\mathrm{R2}} = 85\,\mathrm{ps}$ are attributed to exciton recombination. The longer component with a decay time of $\tau_{\mathrm{R3}} = 520\,\mathrm{ps}$ corresponds to the recombination of spatially separated electrons and holes.

8.2.2 Optical Orientation of Excitons, Electrons and Holes

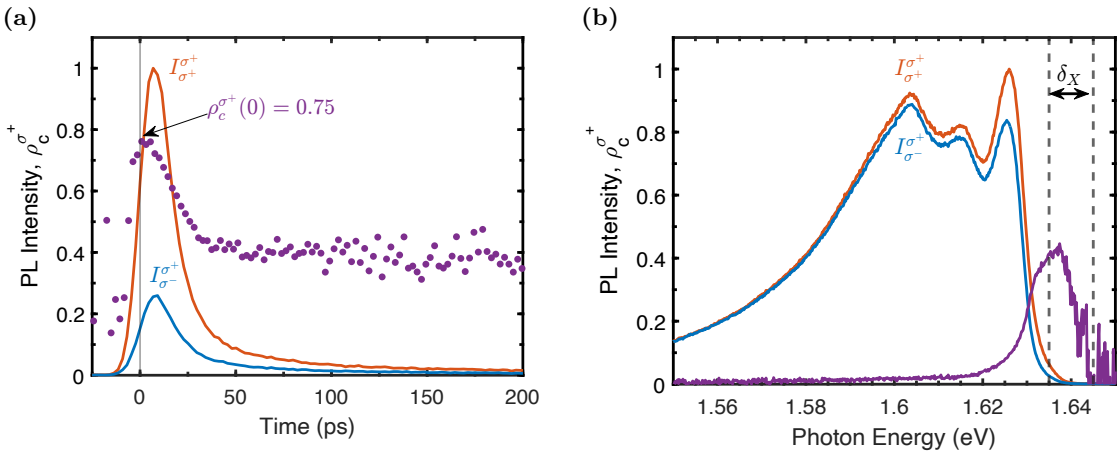

Figure 8.7: Figure 8.7a shows the photoluminescence (PL) dynamics measured for σ^+ excitation at $E_{\text{exc}} = 1.771\,\text{eV}$ and $P_{\text{exc}} = 100\,\mu\text{W}$ for the σ^+ (red line) and σ^- (blue line) polarizations in detection with the dynamic of the optical orientation degree $\rho_c^{\sigma^+}(t)$ that is calculated from the time-resolved photoluminescence (TRPL). The measurements are performed at a temperature of $T = 1.6\,\text{K}$. Figure 8.7b shows the time-integrated PL spectra for the σ^+ (red line) and σ^- (blue line) polarizations in detection under σ^+ excitation at $E_{\text{exc}} = 1.771\,\text{eV}$ and $P_{\text{exc}} = 100\,\mu\text{W}$ and the spectral dependence of the optical orientation degree $\rho_c^{\sigma^+}$, measured at $T = 1.6\,\text{K}$.

The photoluminescence (PL) dynamics detected in σ^+ and σ^- polarizations under σ^+ excitation are shown in Figure 8.7a. The measured signal amplitude in σ^+ polarization is larger than in σ^- polarization that indicates a strong optical orientation degree $\rho_c^{\sigma^+}(t)$ (see Equation (6.4)). The time-dependent behavior of $\rho_c^{\sigma^+}(t)$ is shown in Figure 8.7a. Immediately following optical excitation, $\rho_c^{\sigma^+}$ reaches a value of 0.75, then decreases to 0.4 within 15 ps, and remains constant within the observed time range.

This rapid decrease in $\rho_c^{\sigma^+}$ is attributed to exciton decay into electrons and holes, with the process limited by the exciton recombination time rather than the spin relaxation time. Consequently, the spin relaxation time cannot be directly inferred from the dynamics of $\rho_c^{\sigma^+}$. After exciton recombination, electron-hole pairs with long recombination times slowly relax their spin orientation, leading to a steady polarization $\rho_c^{\sigma^+} = 0.4$. The absence of $\rho_c^{\sigma^+}$ before pulse arrival (negative time in Figure 8.7a) suggests that the spin relaxation time of electron-hole pairs is less than the pulse repetition period of 12.5 ns.

The complete polarization of excitons in perovskites is described by $\rho_c^{\sigma^+}(0) = 1$ and the Equation (8.2) from Section 8.1.2 where the spin relaxation time τ_s can be estimated. By taking $\tau_X = \tau_{R1} = 15\,\text{ps}$ and $\rho_c^{\sigma^+} = 0.75$ from the experimental data, $\tau_s = 75\,\text{ps}$ is obtained.

The time-resolved photoluminescence (TRPL) measurements are performed with the laser photon energy E_{exc} detuned by 0.035 eV from the exciton resonance energy E_X, which may accelerate spin relaxation and reduce $\rho_c^{\sigma^+}(t \gg \tau_X, \tau_s)$.

The optical orientation can also be observed in the time-integrated spectrum. Figure 8.7b shows the time-integrated PL spectrum measured for σ^+ (red) and σ^- (blue) polarizations in detection under σ^+ excitation. The σ^+ polarized emission dominates σ^- polarized emission at the higher energy side of the PL spectrum. The corresponding

spectral dependence of the optical orientation degree $\rho_c^{\sigma^+}$. A pronounced maximum of $\rho_c^{\sigma^+} = 0.24$ is observed at the exciton resonance, indicating contributions from excitons, electrons, and holes. These contributions can be separated using a magnetic field (via the Hanle effect) or by examining decay times in TRPL.

In this work, the focus is on the optical orientation of excitons measured with the TRPL method.

8.2.3 Optical Detuning and Temperature Stability

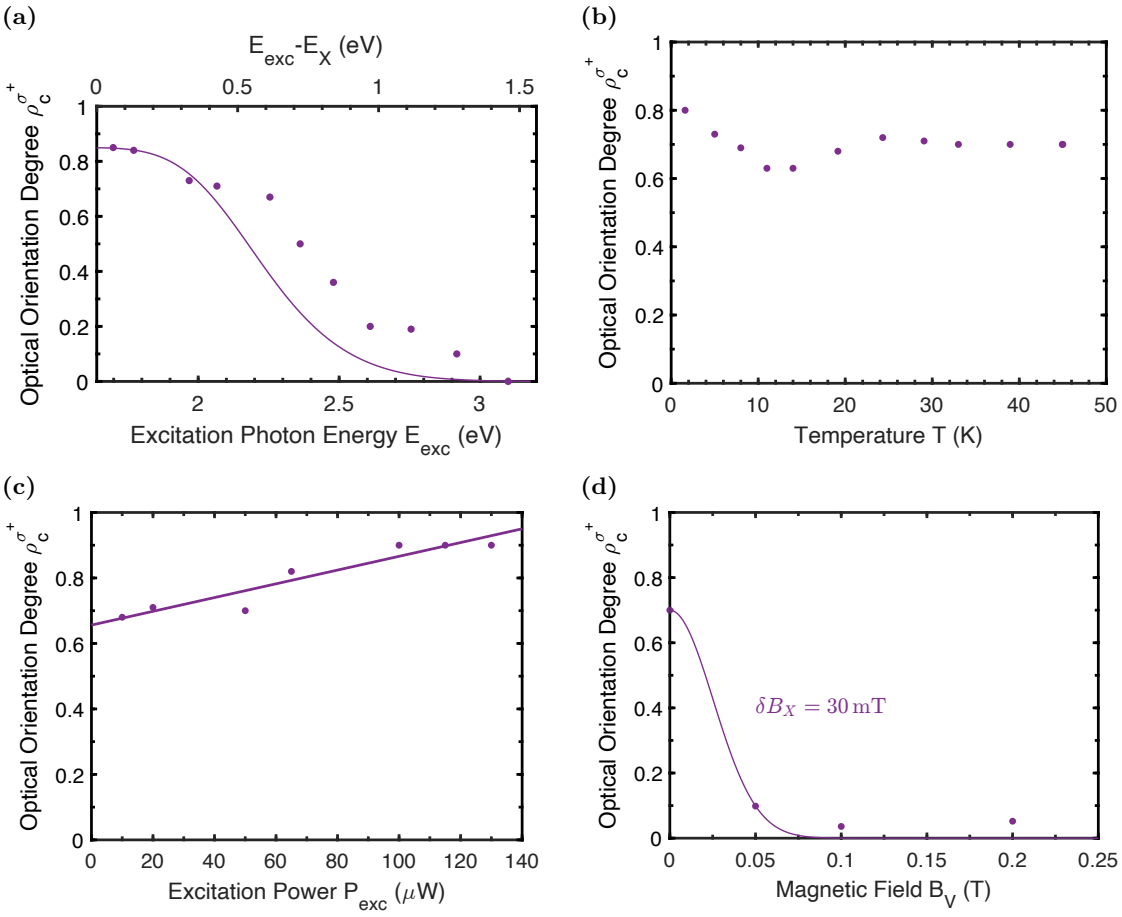

Figure 8.8: The optical orientation of excitons, detected at the exciton resonance energy of 1.64 eV. Figure 8.8a shows the dependence of the initial optical orientation degree $\rho_c^{\sigma^+}(t = 0)$ on the excitation photon energy E_{exc} for σ^+ excitation with a power of $P_{\mathrm{exc}} = 100\,\mu\mathrm{W}$ at $T = 1.6\,\mathrm{K}$. The upper axis indicates the optical detuning from the exciton resonance that is defined as $E_{\mathrm{exc}} - E_{\mathrm{X}}$. The solid line shows the theoretical curve of P^{SR} (see Section 8.1.2) accounting for the Elliott-Yafet spin relaxation due to interaction with longitudinal optical phonons. Figure 8.8b presents the temperature dependence of $\rho_c^{\sigma^+}(t = 0)$. Figure 8.8c shows the dependence of $\rho_c^{\sigma^+}(t = 0)$ on the excitation power. Figure 8.8d shows the dependence of $\rho_c^{\sigma^+}(t = 0)$ on the magnetic field applied in the Voigt geometry (B_{V}). The data are fitted with a Lorentzian curve, showing a half-width at half maximum of $\delta B_{\mathrm{X}} = 30\,\mathrm{mT}$.

Figure 8.8a presents the optical orientation degree $\rho_c^{\sigma^+}(t = 0)$ in dependence of the excitation photon energy (dots) measured at the exciton resonance energy of 1.64 eV. It is observed that $\rho_c^{\sigma^+}$ gradually decreases from 0.85 to 0.70 as the excitation photon energy increases from 1.7 eV to 2.3 eV, corresponding to an optical detuning of 0.6 eV. $\rho_c^{\sigma^+}$ decreases for higher detuning faster and approaches zero at $E_{\text{exc}} = 3.1$ eV, which corresponds to an optical detuning of 1.5 eV. A similar dependence was measured for $FA_{0.9}Cs_{0.1}PbI_{2.8}Br_{0.2}$ (see Section 8.1.2). The theoretical dependence (violet line) is calculated by accounting for the modification of the optical matrix elements for large detunings and the Elliott-Yafet spin relaxation mechanism due to interaction with longitudinal optical phonons. It is dependence in agreement with the experimental data in $FA_{0.9}Cs_{0.1}PbI_{2.8}Br_{0.2}$, and also closely follows the experimental data for the $MAPbI_3$. This leads to the conclusion that the Dyakonov-Perel spin relaxation mechanism is absent in $MAPbI_3$ and that the reduction of the crystal symmetry from cubic to orthorhombic does not provide a breaking of the spatial inversion symmetry.

Non-resonant optical excitation with energy exceeding the exciton binding energy generates electron-hole pairs with opposite momenta, reducing the probability of exciton formation. It is hypothesized that these electrons and holes relax to the band edges, where they can either form excitons or become localized.

The observation of large $\rho_c^{\sigma^+}$ under non-resonant excitation indicates that optical selection rules are maintained not only near the absorption edge but also for larger detunings. Unlike bulk materials, $\rho_c^{\sigma^+}$ in perovskites remains stable with increasing excitation power from 10 µW to 130 µW (Figure 8.8c) and temperature from 1.6 K to 45 K (Figure 8.8b). In this range of powers the optical orientation of excitons is weakly sensitive to the excitation density. The maximal used excitation power of 130 µW corresponds to an exciton density of about $1.3 \cdot 10^{13}\,\text{cm}^{-3}$, which is relatively small for effects related to exciton-exciton interaction to take account.

The depolarization of exciton spin in a transverse magnetic field (Hanle effect) was measured. $I_{\sigma^+}^{\sigma^+}(t)$ and $I_{\sigma^-}^{\sigma^+}(t)$ were integrated over a time range of 1 ns, which is longer than the exciton spin lifetime but shorter than the carrier recombination time. The results are presented in Figure 8.8d. The Hanle curves for electrons and holes, which exhibit narrow profiles due to their long spin relaxation times, are not included in this dependence. For magnetic fields weaker than the exciton exchange interaction, the Hanle effect in perovskites can be expressed by the same Equation (8.3) in Section 8.1.2 for the optical orientation degree $\rho_c^{\sigma^+}(B_{\text{V}})$, where the equation describes the Hanle curve under continuous wave excitation or when T_{s} is much shorter than the integration time in the time-resolved photoluminescence (TRPL) dynamics.

By fitting the Hanle curve, the half-width at half-maximum is determined to be (see Equation (3.11) in Section 3.4.1) $\delta B_{\text{X}} = \frac{2\hbar}{\mu_{\text{B}} g_{\text{V,X}} T_{\text{s}}} = 30$ mT and the exciton spin lifetime is calculated as $T_{\text{s}} = 300$ ps, using a g-factor of $g_{\text{V,X}} = 2.5$.

8.2.4 Exciton Spin Polarization in Longitudinal Magnetic Field

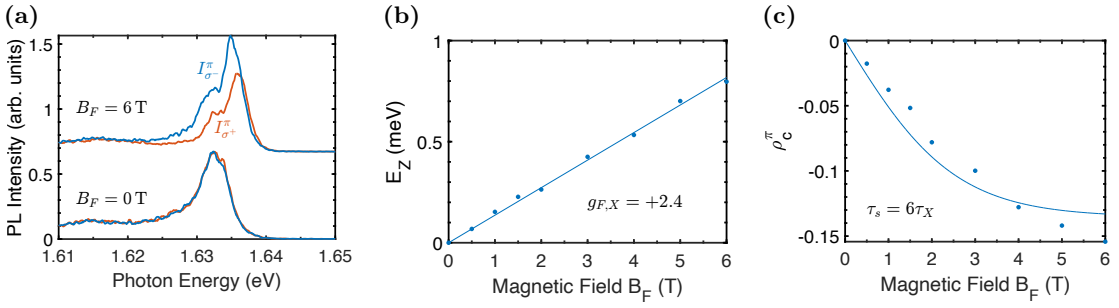

Figure 8.9: Figure 8.9a shows the photoluminescence (PL) spectra at $t = 0\,\mathrm{ps}$ measured in σ^+ (red) and σ^- (blue) polarizations under an applied longitudinal magnetic field of $B_\mathrm{F} = 0\,\mathrm{T}$ and $B_\mathrm{F} = 6\,\mathrm{T}$. The excitation is linearly polarized with a photon energy of $E_\mathrm{exc} = 1.771\,\mathrm{eV}$ and power $P_\mathrm{exc} = 100\,\mu\mathrm{W}$ at a temperature of $T = 1.6\,\mathrm{K}$. Figure 8.9b shows the dependence of the exciton Zeeman splitting energy E_Z in the magnetic field B_F. A linear fit of the data yields a g-factor of $g_\mathrm{F,X} = +2.4$. Figure 8.9c shows the dependence of the circular polarization degree induced by the longitudinal magnetic field B_F (dots). The line represents a fit using Equation (8.6) with a fitting parameter of $\tau_\mathrm{s} = 6\tau_\mathrm{X} = 90\,\mathrm{ps}$.

To determine the exciton g-factor directly and to observe the magneto-induced degree of circular polarization, time-resolved photoluminescence signals (TRPL) were measured under linearly polarized excitation in a longitudinal magnetic field with σ^+ and σ^- polarizations in detection and calculated the same way as described in Section 8.1.4.

The PL spectra at $t = 0\,\mathrm{ps}$ for σ^+ and σ^- polarizations in detection measured at $B_\mathrm{F} = 0\,\mathrm{T}$ and $B_\mathrm{F} = 6\,\mathrm{T}$ are shown in Figure 8.9a. The spectral shift of 0.8 eV between the two polarizations at $B_\mathrm{F} = 6\,\mathrm{T}$ results from the Zeeman splitting of the bright exciton $E_\mathrm{Z} = \mu_\mathrm{B} g_\mathrm{F,X} B_\mathrm{F}$ (see Equation (8.5)). The dependence of E_Z on the magnetic field is linear, with no zero-field offset, as shown in Figure 8.9b. The calculated g-factor is $g_\mathrm{F,X} = +2.4$, where the positive sign indicates that the polarized σ^+ spectrum appears at higher energy. The exciton g-factor is in agreement with the results in [52], where the exciton g-factor varies from +2.3 to +2.7 for various bulk lead halide perovskites with band gaps in the visible spectral range from 1.52 to 3.21 eV.

The PL spectrum detected in σ^- polarization exhibits a higher intensity than in σ^+ at $B_\mathrm{F} = 6\,\mathrm{T}$, whereas equal intensities are observed in the absence of a magnetic field. This indicates that the degree of circular polarization of the PL is induced by the applied magnetic field. The exciton spectrum was integrated over the exciton recombination time, and the circular polarization degree $\rho^{\pi}_c(B_\mathrm{F})$ was calculated as in the sections before. As shown in Figure 8.9c, in strong magnetic field the lower-energy spin state is more populated. The process is schematically depicted in Figure 8.4d. The circular polarization degree dependence on magnetic field can be described by exciton thermalization across Zeeman-split levels as before (see Equation (8.6) in Section 8.1.4). A fit to the data, using the experimentally determined exciton recombination time $\tau_\mathrm{X} = 15\,\mathrm{ps}$ and temperature $T = 1.6\,\mathrm{K}$, is shown in Figure 8.9c as a solid line. This fit yields a spin relaxation time of $\tau_\mathrm{s} = 90\,\mathrm{ps}$ as the only fitting parameter. This value is consistent with the spin relaxation time determined from the optical orientation degree at zero magnetic field. The longer spin relaxation time relative to the recombination time leads to a large degree of optical orientation and a low magneto-induced circular polarization degree ρ^{π}_c.

8.2.5 Spin Precession in Magnetic Field

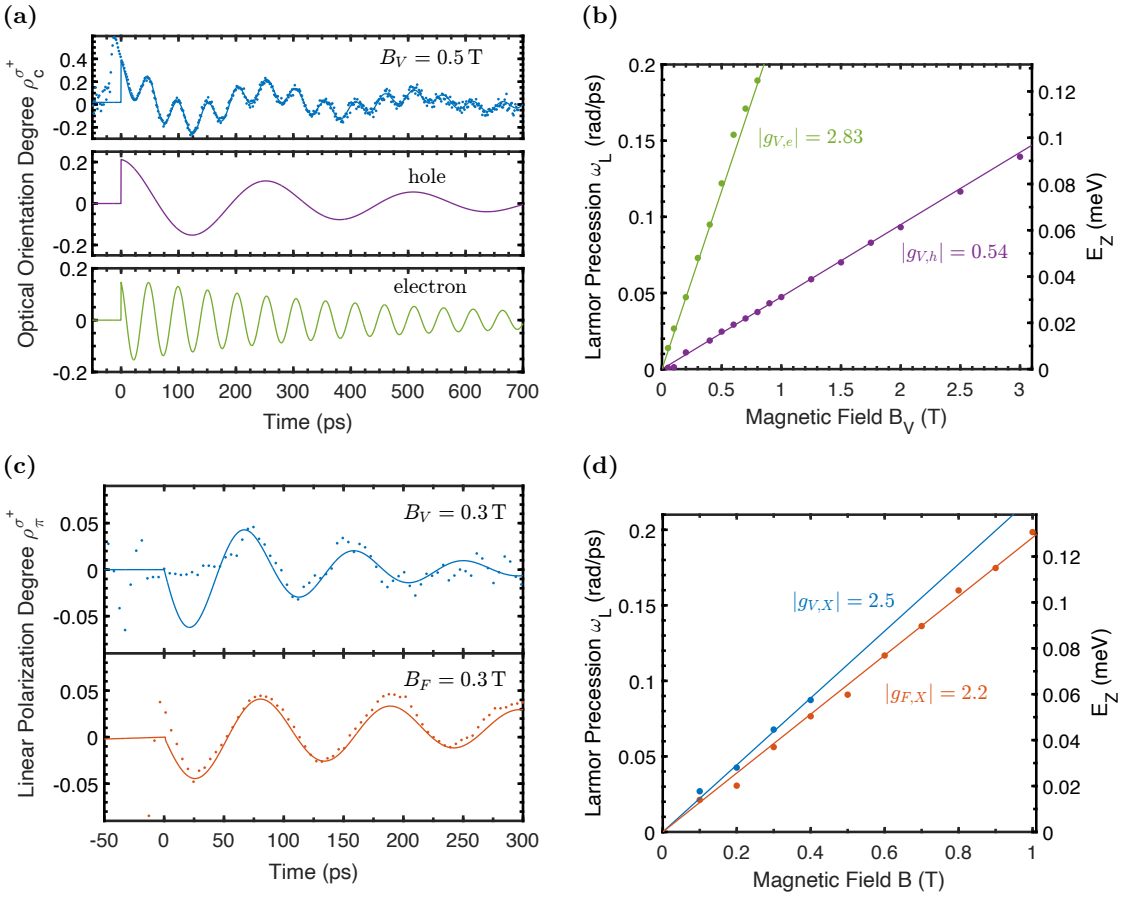

Figure 8.10: The spin precession of excitons measured in Voigt and Faraday geometries. Figure 8.10a shows the dynamics of the optical orientation degree $\rho_c^{\sigma^+}(t)$ for σ^+ excitation in a transverse magnetic field ($B_\mathrm{V} = 0.5\,\mathrm{T}$) at $T = 1.6\,\mathrm{K}$ (dots). The data were fitted with a double decaying cosine function, as represented by the solid line (violet for hole, green for electron, blue sum of hole and electron). Figure 8.10b presents the Larmor precession frequency of electron and hole as a function of B_V (dots). A linear fit to the data yields a g-factor of $|g_{\mathrm{V,e}}| = 2.83$ for the electron and $|g_{\mathrm{V,h}}| = 0.54$ for the hole. Figure 8.10c shows the dynamics of the linear polarization degree $\rho_\pi^{\sigma^+}(t)$ for σ^+ excitation in a transverse magnetic field ($B_\mathrm{V} = 0.3\,\mathrm{T}$) (blue dots) and $\rho_\pi^{\sigma^+}(t)$ for linearly polarized V excitation in a longitudinal magnetic field ($B_\mathrm{F} = 0.3\,\mathrm{T}$) (red dots) at $T = 1.6\,\mathrm{K}$ (dots). The data were fitted with a decaying cosine function, as represented by the solid line. Figure 8.10d shows the Larmor precession frequency of excitons as a function of magnetic field B obtained from $\rho_\pi^{\sigma^+}(t)$. A linear fit provides a g-factor of $|g_{\mathrm{V,X}}| = 2.5$ and $|g_{\mathrm{F,X}}| = 2.2$.

Figure 8.10a (top panel) presents the dynamics of $\rho_c^{\sigma^+}(t)$ measured at the exciton energy ($E_\mathrm{det} = 1.640\,\mathrm{eV}$) in a transverse magnetic field of $B_\mathrm{V} = 0.5\,\mathrm{T}$ (blue dots). A complex spin-beat pattern is observed, characterized by a slow decay over a temporal range of 600 ps. The decay time is significantly longer than the exciton lifetime, indicating that the signal originates from the coherent spin precession of spatially separated, localized electrons and holes. The optical orientation dynamics is fitted using equation (8.7). The

individual dynamics of hole and electron spin polarization are displayed in the middle and bottom panels of Figure 8.10a.

The dependence of the Larmor precession frequencies on the magnetic field is shown in Figure 8.10b. From linear fits, the Landé factors of the electron and hole are determined as $|g_{\mathrm{V,e}}| = 2.83$ and $|g_{\mathrm{V,h}}| = 0.54$, respectively. The absence of a finite offset in the Zeeman splittings as $B_{\mathrm{V}} \to 0$ confirms that the observed signal originates from spatially separated electron-hole pairs with negligible exchange interaction. Such an interaction would otherwise result in a finite offset for electron-hole pairs bound into excitons.

Considering that in $MAPbI_3$, the electron g-factor is positive and the hole g-factor is negative [49, 137], the bright exciton g-factor is calculated as $g_{\mathrm{V,X}} = g_{\mathrm{V,h}} + g_{\mathrm{V,e}} = +2.29$, which is in good agreement with the value $g_{\mathrm{F,X}} = +2.4$ obtained from the Zeeman splitting of the PL emission line measured in longitudinal magnetic field (see Section 8.2.4).

For calculation of the dynamics of the linear polarization degree $\rho_{\pi}^{\sigma^+}$ Equation (8.8) is used. The linear polarization degree $\rho_{\pi}^{\sigma^+}$ arises only from the spin orientation of both electrons and holes during exciton recombination, whereas the recombination of a polarized carrier with an unpolarized one could lead to circular polarization, complicating the optical orientation signal analysis.

The dynamics of $\rho_{\pi}^{\sigma^+}(t)$, measured at $B_{\mathrm{V}} = 0.3\,\mathrm{T}$ for σ^+ polarized excitation, is shown in the top panel of Figure 8.10c (blue dots). The signal exhibits a single oscillatory component with a short decay time, which can be fitted by Equation (8.9) the same way as in Section 8.1.5 (see Figure 8.10d). The dependence of $\omega_{\mathrm{V,X}}$ on B_{V} is linear with no zero-field offset, and the slope gives a g-factor of $|g_{\mathrm{V,X}}| = 2.5$, consistent with direct measurements from the spectral shift.

The spin coherence of the bright exciton can also be generated in Faraday geometry. In this configuration, a longitudinal magnetic field not only splits the Zeeman levels of the bright exciton but also creates a quantum superposition of the exciton's dipole moments, oriented both horizontally and vertically. Thus, if one of the dipole moments is induced by linearly polarized light, oscillations of the bright exciton can be observed in $\rho_{\pi}^{\sigma^+}$ in the presence of a longitudinal magnetic field.

The dynamics of $\rho_{\pi}^{\sigma^+}$ under vertically polarized excitation at $B_{\mathrm{F}} = 0.3\,\mathrm{T}$ are shown in bottom panel in Figure 8.10c (red dots), with a single oscillating component, which can also be fitted using (8.9). The dependence of $\omega_{\mathrm{F,X}}$ on B_{F} is linear with no zero-field offset, yielding a g-factor of $|g_{\mathrm{F,X}}| = 2.2$ that is comparable to $g_{\mathrm{F,X}} = 2.4$ from the Zeeman splitting for $MAPbI_3$ in Section 8.2.4 and for $FA_{0.9}Cs_{0.1}PbI_{2.8}Br_{0.2}$ in Section 8.1.4.

The theoretical modeling based on the fine structure of these signals in both geometries can accurately reproduce the observed results. The study of $\rho_{\pi}^{\sigma^+}$ dynamics in both longitudinal and transverse magnetic fields provides access to the anisotropy of the exciton g-factor. For the $MAPbI_3$ single microcrystal, a g-factor of $|g_{\mathrm{F,X}}| = 2.2$ (out-of-plane) and $|g_{\mathrm{V,X}}| = 2.5$ (in-plane) was measured. The similarity of these values suggests that the exciton g-factor is isotropic, a property commonly observed in bright excitons within bulk perovskites.

8.3 Summary

The use of time- and polarization-resolved photoluminescence spectroscopy techniques to distinguish between short lived exciton and long-lived electron-hole recombination signals. The perovskite samples demonstrate for excitons an optical orientation degree up to 85 % in $FA_{0.9}Cs_{0.1}PbI_{2.8}Br_{0.2}$ bulk perovskite crystals and in $MAPbI_3$ microcrystals at $T = 1.6\,\mathrm{K}$.

The optical orientation in $FA_{0.9}Cs_{0.1}PbI_{2.8}Br_{0.2}$ shows a robustness in detuning of the excitation energy up to 0.3 eV from the fundamental absorption edge, and is fully suppressed for excitation energies exceeding 1 eV. The robustness of the excitation detuning in $MAPbI_3$ is 0.3 eV, similar to $FA_{0.9}Cs_{0.1}PbI_{2.8}Br_{0.2}$, but has a larger suppression with about 1.5 eV.

A combination of symmetry analysis and atomistic calculations suggests that the optical orientation observed in lead halide perovskites is due to their unique intrinsic properties. In particular, these properties include the chiral selection rules that govern the optical transitions between the twofold degenerate valence and conduction bands, and the suppression of spin relaxation due to the lack of spin splitting in the bands, which is a direct consequence of the crystalline inversion center present in these materials.

In $FA_{0.9}Cs_{0.1}PbI_{2.8}Br_{0.2}$ and $MAPbI_3$ the coherent spin precession of electrons and holes were observed in time-resolved circularly polarized luminescence for non-resonant excitation in transverse magnetic field. The precession provides direct access to their Landé factors and shows preserved the spin orientation of the charge carriers during their energy relaxation.

A linear polarization of the emission was observed that serves as indication of electron and hole spin correlations in perovskites.

An overview of the achieved results of $FA_{0.9}Cs_{0.1}PbI_{2.8}Br_{0.2}$ and $MAPbI_3$ about spin lifetime $T_{\mathrm{s,e\text{-}h/X}}$, electron-hole/exciton lifetime $\tau_{\mathrm{e\text{-}h/X}}$, spin relaxation time $\tau_{\mathrm{s,e\text{-}h/X}}$ and initial optical orientation degree $\rho^{\sigma^+}_{\mathrm{c,e\text{-}h/X}}(0)$ of the exciton and electron-hole (e-h) in Table 8.1 and the Landé factors is in Table 8.2.

The initial polarization degree $\rho^{\sigma^+}_{\mathrm{c}}(0)$ for $FA_{0.9}Cs_{0.1}PbI_{2.8}Br_{0.2}$ and $MAPbI_3$ for exciton remains with 0.85 the same, but is different for e-h where the optical orientation degree in $FA_{0.9}Cs_{0.1}PbI_{2.8}Br_{0.2}$ (0.6) is higher compared to $MAPbI_3$ (0.4). The spin lifetime, exciton lifetime and spin relaxation time for $FA_{0.9}Cs_{0.1}PbI_{2.8}Br_{0.2}$ is higher compared to $MAPbI_3$. This changes for the e-h lifetime, where it is approximately twice longer for $MAPbI_3$ compared to $FA_{0.9}Cs_{0.1}PbI_{2.8}Br_{0.2}$. For both sample the spin lifetime T_{s} for exciton and e-h is closer and lower to the spin relaxation time τ_{s}, then to the higher lifetime τ.

The Landé factor for carrier in Voigt geometry $|g_{\mathrm{V,e}}|$ and $|g_{\mathrm{V,h}}|$ are in $FA_{0.9}Cs_{0.1}PbI_{2.8}Br_{0.2}$ higher compared to $MAPbI_3$, but in sum approximately the same for both samples ($g_{\mathrm{V,X}} = g_{\mathrm{V,e}} + g_{\mathrm{V,h}} \approx 2.3$) [49]. This is comparable to the measured values for the exciton in transverse magnetic fields with $g_{\mathrm{V,X}} = 2.3$ for $FA_{0.9}Cs_{0.1}PbI_{2.8}Br_{0.2}$ and $g_{\mathrm{V,X}} = 2.5$ for $MAPbI_3$. The Landé factor for exciton in longitudinal magnetic fields is with $g_{\mathrm{F,X}} = 2.4$ the same for both samples.

Table 8.1: Spin lifetime (T_s), lifetime (τ), spin relaxation time τ_s, initial optical orientation degree $\rho_c^{\sigma^+}(0)$ of the exciton (X) and carrier (e-h) in $FA_{0.9}Cs_{0.1}PbI_{2.8}Br_{0.2}$ and $MAPbI_3$.

Sample	τ_X (ps)	$\tau_{s,X}$ (ps)	$T_{s,X}$ (ps)	$\tau_{e\text{-}h}$ (ps)	$\tau_{s,e\text{-}h}$ (ps)	$T_{s,e\text{-}h}$ (ps)	$\rho_{c,X}^{\sigma^+}(0)$	$\rho_{c,e\text{-}h}^{\sigma^+}(0)$
$FA_{0.9}Cs_{0.1}PbI_{2.8}Br_{0.2}$	55	250	45	840	1260	505	0.85	0.6
$MAPbI_3$	15	90	13	520	2500	430	0.85	0.4

Table 8.2: Landé factors of the exciton and carrier in $FA_{0.9}Cs_{0.1}PbI_{2.8}Br_{0.2}$ and $MAPbI_3$.

Sample	$\lvert g_{V,e}\rvert$	$\lvert g_{V,h}\rvert$	$g_{V,e} + g_{V,h}$	$g_{V,X}$	$g_{F,X}$
$FA_{0.9}Cs_{0.1}PbI_{2.8}Br_{0.2}$	3.48	1.15	2.33	2.3	2.4
$MAPbI_3$	2.83	0.54	2.29	2.5	2.4

9 Summary and Outlook

In this thesis different polarization-resolved time-integrated and time-resolved magneto-optical spectroscopy techniques were used to investigate optically the spin and charge dynamics in FM-hybrid semiconductor structures, monolayer TMD hybrid structure and lead halide perovskite samples.

First, the long-range magnetic proximity effect was investigated in magnetite (semimetal) and nickel ferrite (dielectric) hybrid structure with CdTe QW separated by a nonmagnetic (Cd,Mg)Te barrier in Chapter 6. The effect consists in the effective p-d exchange interaction of acceptor-bound holes in the QW with d-electrons of the FM without overlap of their wave functions. It was shown that the magnetic proximity effect has an universal behavior due to the universal nature of the phononic mechanism. Moreover, the effect is caused by the magnetic material itself and not ferromagnetic interface. The dynamics of the magnetic proximity effect of nonmetals is nonmonotonic and differs from metal-based (Fe, Co) hybrid structures, that show a much longer spin relaxation time of the acceptor-bound holes. This dynamic behavior is explained by additional recombination-induced dynamic polarization of electrons in the quantum well, that becomes significant for much longer spin relaxation times of the electrons than their lifetime. The universal origin of the long-range exchange interaction along with the possibility of its electrical control offers prospects for the development of low-voltage spintronic devices compatible with existing solid-state electronics.

To investigate the long-range magnetic proximity effect in the samples the circular polarization degree in longitudinal magnetic fields studied and compared to the magnetization induced by the magnetic material of the samples. The g-factor from photoexcited carriers was evaluated from the Larmor precession from pump-probe Kerr-Rotation measurements and the effective exchange magnetic field induced by the magnetic layer was excluded. The population dynamics of photoexcited electrons and holes was evaluated for different temperature and applied longitudinal magnetic fields, thus a constant lifetime was achieved. By measuring of the dynamics the optical orientation degree in longitudinal magnetic fields the spin relaxation time was studied. With the investigations carried out previously, the dynamics of the magnetic proximity effect was studied, where the spin polarization of the acceptor-bound holes was achieved, that gave access to the exchange splitting energy $\Delta_{\text{exch}} = 70\,\mu\text{eV}$.

Second, the Hanle and polarization recovery effect on resident electrons in single-layer $MoSe_2$ were studied using single beam excitation and detection of spin polarization of resident electrons in Chapter 7.

The spin dynamics in weak magnetic fields are governed by localized resident electrons in the $MoSe_2$/EuS hybrid structure. Despite strong spin-orbit splitting, equivalent to an effective magnetic field of $\sim 100\,\text{T}$, a weak external field of just 1 mT can induce spin depolarization or polarization recovery.

Spin-conserving intervalley scattering is suppressed since electrons do not occupy higher-energy states $K\downarrow$ and $K'\uparrow$, preventing their contribution to the dynamical

averaging of the spin-orbit splitting Ω_{SO}. The similar widths of Hanle and polarization recovery curves resemble donor-bound electrons in bulk GaAs, where spin relaxation is dominated by random nuclear fields.

In 2D monolayers, the g-factor and spin relaxation are highly anisotropic compared to bulk semiconductors. The model requires a nonzero intervalley in-plane g-factor, achievable if electrons are localized within the layer. Localization breaks the symmetry and leads to non-zero in-plane g-factor, which fluctuates around zero value. When a magnetic field is applied this results spin dephasing but no oscillations are observed because the average g-factor is close to 0.

A single-laser beam technique reveals that localized electrons significantly influence spin dynamics in 2D monolayers. In the $MoSe_2$/EuS structure, spin relaxation is driven by random effective fields from contact spin interactions, such as hyperfine interactions in $MoSe_2$ or exchange interactions with EuS magnetic ions.

This work demonstrates that the implemented single laser beam technique is a powerful tool for spin studies in transition metal dichalcogenides. It opens new avenues for the investigation of proximity effects in hybrid structures and magnetic sensor applications with 2D monolayers.

Third, the spin dynamics of exciton and charge carriers in lead halide perovskite was studied in Chapter 8. The use of time- and polarization-resolved photoluminescence techniques enables to distinguish between short lived exciton and long-lived electron-hole recombination signals.

A high optical orientation degree of 85 % was achieved for excitons at low temperature. The detuning of the excitation energy shows a robustness from the edge to fully suppression. The investigation shows a suppression of spin relaxation due to lack of spin splitting in the bands due to crystalline inversion center. Spin precession was studied in the circular polarization degree in transverse magnetic fields and the g-factors were evaluated. Electron and hole correlation in perovskite was indicated through the observation of oscillations in linear polarized emission.

The combination of highly polarized exciton emission and extended spin relaxation times in lead halide perovskites makes these materials promising candidates for quantum information and spintronic technologies. Their ability for efficient optical spin manipulation and maintenance of long-lived spin coherence further emphasizes their potential for these applications.

Bibliography

[1] Charles Kittel. *Introduction to Solid State Physics*. 8th Edition. Wiley, 2005. ISBN: 978-0-471-41526-8.

[2] Qiming Shao, Peng Li, Luqiao Liu, Hyunsoo Yang, Shunsuke Fukami, Armin Razavi, Hao Wu, Kang Wang, Frank Freimuth, Yuriy Mokrousov, Mark D. Stiles, Satoru Emori, Axel Hoffmann, Johan Akerman, Kaushik Roy, Jian-Ping Wang, See-Hun Yang, Kevin Garello, and Wei Zhang. "Roadmap of Spin-Orbit Torques". In: *IEEE Transactions on Magnetics* 57.7 (2021), pp. 1–39. DOI: 10.1109/TMAG.2021.3078583.

[3] V. K. Kalevich and V. L. Korenev. "Effect of electric field on the optical orientation of 2D electrons". In: *ZhETF Pisma Redaktsiiu* 52 (1990), p. 859.

[4] Boris P. Zakharchenya and Vladimir L. Korenev. "Integrating Magnetism into Semiconductor Electronics". In: *Physics-Uspekhi* 48.6 (2005), pp. 603–608. DOI: 10.1070/PU2005v048n06ABEH002200.

[5] M. A. Pankov, B. A. Aronzon, V. V. Rylkov, A. B. Davydov, E. Z. Meilikhov, R. M. Farzetdinova, É. M. Pashaev, M. A. Chuev, I. A. Subbotin, I. A. Likhachev, B. N. Zvonkov, A. V. Lashkul, and R. Laiho. "Ferromagnetic Transition in GaAs/Mn/ GaAs/$In_xGa_{1-x}As$/GaAs Structures with a two-dimensional hole gas". In: *Journal of Experimental and Theoretical Physics* 109.2 (2009), pp. 293–301. DOI: 10.1134/S1063776109080159.

[6] M. V. Dorokhin, Yu A. Danilov, P. B. Demina, V. D. Kulakovskii, O. V. Vikhrova, S. V. Zaitsev, and B. N. Zvonkov. "Emission properties of InGaAs/GaAs heterostructures with δ<Mn>-doped Barrier". In: *Journal of Physics D: Applied Physics* 41.24 (2008), p. 245110. DOI: 10.1088/0022-3727/41/24/245110.

[7] V. L. Korenev, I. A. Akimov, S. V. Zaitsev, V. F. Sapega, L. Langer, D. R. Yakovlev, Yu. A. Danilov, and M. Bayer. "Dynamic spin polarization by orientation-dependent separation in a ferromagnet-semiconductor hybrid". In: *Nature Communications* 3.1 (2012), p. 959. DOI: 10.1038/ncomms1957.

[8] Vladimir L. Korenev. "Electric control of magnetic moment in a ferromagnet-semiconductor hybrid system". In: *Journal of Experimental and Theoretical Physics Letters* 78.9 (2003), pp. 564–568. DOI: 10.1134/1.1641485.

[9] V. L. Korenev, M. Salewski, I. A. Akimov, V. F. Sapega, L. Langer, I. V. Kalitukha, J. Debus, R. I. Dzhioev, D. R. Yakovlev, D. Müller, C. Schröder, H. Hövel, G. Karczewski, M. Wiater, T. Wojtowicz, Yu. G. Kusrayev, and M. Bayer. "Long-range p-d exchange interaction in a ferromagnet-semiconductor hybrid structure". In: *Nature Physics* 12.1 (2016), pp. 85–91. DOI: 10.1038/nphys3497.

[10] Claude Cohen-Tannoudji and Jacques Dupont-Roc. "Experimental Study of Zeeman Light Shifts in Weak Magnetic Fields". In: *Physical Review A* 5.2 (1972), pp. 968–984. DOI: 10.1103/PhysRevA.5.968.

[11] J. P. Van Der Ziel, P. S. Pershan, and L. D. Malmstrom. "Optically-Induced Magnetization Resulting from the Inverse Faraday Effect". In: *Physical Review Letters* 15.5 (1965), pp. 190–193. DOI: 10.1103/PhysRevLett.15.190.

[12] V. L. Korenev, I. V. Kalitukha, I. A. Akimov, V. F. Sapega, E. A. Zhukov, E. Kirstein, O. S. Ken, D. Kudlacik, G. Karczewski, M. Wiater, T. Wojtowicz, N. D. Ilyinskaya, N. M. Lebedeva, T. A. Komissarova, Yu. G. Kusrayev, D. R. Yakovlev, and M. Bayer. "Low voltage control of exchange coupling in a ferromagnet-semiconductor quantum well hybrid structure". In: *Nature Communications* 10.1 (2019), p. 2899. DOI: 10.1038/s41467-019-10774-0.

[13] Seung Gyo Jeong, Jiwoong Kim, Ambrose Seo, Sungkyun Park, Hu Young Jeong, Young-Min Kim, Valeria Lauter, Takeshi Egami, Jung Hoon Han, and Woo Seok Choi. "Unconventional interlayer exchange coupling via chiral phonons in synthetic magnetic oxide heterostructures". In: *Science Advances* 8.4 (2022), eabm4005. DOI: 10.1126/sciadv.abm4005.

[14] I. A. Akimov, M. Salewski, I. V. Kalitukha, S. V. Poltavtsev, J. Debus, D. Kudlacik, V. F. Sapega, N. E. Kopteva, E. Kirstein, E. A. Zhukov, D. R. Yakovlev, G. Karczewski, M. Wiater, T. Wojtowicz, V. L. Korenev, Yu. G. Kusrayev, and M. Bayer. "Direct measurement of the long-range p-d exchange coupling in a ferromagnet-semiconductor Co/CdMgTe/CdTe quantum well hybrid structure". In: *Physical Review B* 96.18 (2017), p. 184412. DOI: 10.1103/PhysRevB.96.184412.

[15] I. V. Kalitukha, M. Salewski, I. A. Akimov, V. L. Korenev, V. F. Sapega, D. R. Yakovlev, G. Karczewski, M. Wiater, T. Wojtowicz, Yu. G. Kusrayev, and M. Bayer. "Interfacial Ferromagnetism in a Co/CdTe Ferromagnet-Semiconductor Quantum Well Hybrid Structure". In: *Physics of the Solid State* 60.8 (2018), pp. 1578–1581. DOI: 10.1134/S1063783418080139.

[16] Ina V. Kalitukha, Olga S. Ken, Vladimir L. Korenev, Ilya A. Akimov, Victor F. Sapega, Dmitri R. Yakovlev, Grigorii S. Dimitriev, Lukas Langer, Grzegorz Karczewski, Sergij Chusnutdinow, Tomasz Wojtowicz, and Manfred Bayer. "Coexistence of Short- and Long-Range Ferromagnetic Proximity Effects in a Fe/(Cd,Mg)Te/CdTe Quantum Well Hybrid Structure". In: *Nano Letters* 21.6 (2021), pp. 2370–2375. DOI: 10.1021/acs.nanolett.0c04218.

[17] Chenhao Jin, Jonghwan Kim, M. Iqbal Bakti Utama, Emma C. Regan, Hans Kleemann, Hui Cai, Yuxia Shen, Matthew James Shinner, Arjun Sengupta, Kenji Watanabe, Takashi Taniguchi, Sefaattin Tongay, Alex Zettl, and Feng Wang. "Imaging of pure spin-valley diffusion current in WS_2-WSe_2 heterostructures". In: *Science* 360.6391 (2018), pp. 893–896. DOI: 10.1126/science.aao3503.

[18] Juan F. Sierra, Jaroslav Fabian, Roland K. Kawakami, Stephan Roche, and Sergio O. Valenzuela. "Van der Waals heterostructures for spintronics and opto-spintronics". In: *Nature Nanotechnology* 16.8 (2021), pp. 856–868. DOI: 10.1038/s41565-021-00936-x.

[19] T. P. Lyons, D. J. Gillard, C. Leblanc, J. Puebla, D. D. Solnyshkov, L. Klompmaker, I. A. Akimov, C. Louca, P. Muduli, A. Genco, M. Bayer, Y. Otani, G. Malpuech, and A. I. Tartakovskii. "Giant effective Zeeman splitting in a monolayer semiconductor realized by spin-selective strong light–matter coupling". In: *Nature Photonics* 16.9 (2022), pp. 632–636. DOI: 10.1038/s41566-022-01025-8.

[20] L. Ren, L. Lombez, C. Robert, D. Beret, D. Lagarde, B. Urbaszek, P. Renucci, T. Taniguchi, K. Watanabe, S. A. Crooker, and X. Marie. "Optical Detection of Long Electron Spin Transport Lengths in a Monolayer Semiconductor". In: *Physical Review Letters* 129.2 (2022), p. 027402. DOI: 10.1103/PhysRevLett.129.027402.

[21] M. M. Glazov, T. Amand, X. Marie, D. Lagarde, L. Bouet, and B. Urbaszek. "Exciton fine structure and spin decoherence in monolayers of transition metal dichalcogenides". In: *Physical Review B* 89.20 (2014), p. 201302. DOI: 10.1103/PhysRevB.89.201302.

[22] Wei-Ting Hsu, Yen-Lun Chen, Chang-Hsiao Chen, Pang-Shiuan Liu, Tuo-Hung Hou, Lain-Jong Li, and Wen-Hao Chang. "Optically initialized robust valley-polarized holes in monolayer WSe_2". In: *Nature Communications* 6.1 (2015), p. 8963. DOI: 10.1038/ncomms9963.

[23] Cedric Robert, Sangjun Park, Fabian Cadiz, Laurent Lombez, Lei Ren, Hans Tornatzky, Alistair Rowe, Daniel Paget, Fausto Sirotti, Min Yang, Dinh Van Tuan, Takashi Taniguchi, Bernhard Urbaszek, Kenji Watanabe, Thierry Amand, Hanan Dery, and Xavier Marie. "Spin-valley pumping of resident electrons in WSe_2 and WS_2 monolayers". In: *Nature Communications* 12.1 (2021), p. 5455. DOI: 10.1038/s41467-021-25747-5.

[24] Luyi Yang, Nikolai A. Sinitsyn, Weibing Chen, Jiangtan Yuan, Jing Zhang, Jun Lou, and Scott A. Crooker. "Long-lived nanosecond spin relaxation and spin coherence of electrons in monolayer MoS_2 and WS_2". In: *Nature Physics* 11.10 (2015), pp. 830–834. DOI: 10.1038/nphys3419.

[25] P. Dey, Luyi Yang, C. Robert, G. Wang, B. Urbaszek, X. Marie, and S. A. Crooker. "Gate-Controlled Spin-Valley Locking of Resident Carriers in WSe_2 Monolayers". In: *Physical Review Letters* 119.13 (2017), p. 137401. DOI: 10.1103/PhysRevLett.119.137401.

[26] Markus Schwemmer, Philipp Nagler, Andreas Hanninger, Christian Schüller, and Tobias Korn. "Long-lived spin polarization in n-doped $MoSe_2$ monolayers". In: *Applied Physics Letters* 111.8 (2017). DOI: 10.1063/1.4987000.

[27] Jing Li, M. Goryca, K. Yumigeta, H. Li, S. Tongay, and S. A. Crooker. "Valley relaxation of resident electrons and holes in a monolayer semiconductor: Dependence on carrier density and the role of substrate-induced disorder". In: *Physical Review Materials* 5.4 (2021), p. 044001. DOI: 10.1103/PhysRevMaterials.5.044001.

[28] F. Meier and Boris Petrovich Zakharchenia, eds. *Optical Orientation*. Modern problems in condensed matter sciences v. 8. Amsterdam; New York: New York: North-Holland; Sole distributors for the U.S.A. and Canada, Elsevier Science Pub. Co, 1984. ISBN: 978-0-444-86741-4.

[29] T. Smolenski, M. Goryca, M. Koperski, C. Faugeras, T. Kazimierczuk, A. Bogucki, K. Nogajewski, P. Kossacki, and M. Potemski. "Tuning Valley Polarization in a WSe_2 Monolayer with a Tiny Magnetic Field". In: *Physical Review X* 6.2 (2016), p. 021024. DOI: 10.1103/PhysRevX.6.021024.

[30] Yu. G. Kusrayev, B. R. Namozov, I. V. Sedova, and S. V. Ivanov. "Optically induced spin polarization and g-factor anisotropy of holes in CdSe/ZnSe quantum dots". In: *Physical Review B* 76.15 (2007), p. 153307. DOI: 10.1103/PhysRevB.76.153307.

[31] V. K. Kalevich and V. L. Korenev. "Anisotropy of the electron g-factor in GaAs/AlGaAs quantum wells". In: *JETP Lett* 56.5 (1992).

[32] Peng Wei, Sunwoo Lee, Florian Lemaitre, Lucas Pinel, Davide Cutaia, Wujoon Cha, Ferhat Katmis, Yu Zhu, Donald Heiman, James Hone, Jagadeesh S. Moodera, and Ching-Tzu Chen. "Strong interfacial exchange field in the graphene/EuS heterostructure". In: *Nature Materials* 15.7 (2016), pp. 711–716. DOI: 10.1038/nmat4603.

[33] Chuan Zhao, Tenzin Norden, Peiyao Zhang, Puqin Zhao, Yingchun Cheng, Fan Sun, James P. Parry, Payam Taheri, Jieqiong Wang, Yihang Yang, Thomas Scrace, Kaifei Kang, Sen Yang, Guo-xing Miao, Renat Sabirianov, George Kioseoglou, Wei Huang, Athos Petrou, and Hao Zeng. "Enhanced valley splitting in monolayer WSe_2 due to magnetic exchange field". In: *Nature Nanotechnology* 12.8 (2017), pp. 757–762. DOI: 10.1038/nnano.2017.68.

[34] Tenzin Norden, Chuan Zhao, Peiyao Zhang, Renat Sabirianov, Athos Petrou, and Hao Zeng. "Giant valley splitting in monolayer WS_2 by magnetic proximity effect". In: *Nature Communications* 10.1 (2019), p. 4163. DOI: 10.1038/s41467-019-11966-4.

[35] Ajay Kumar Jena, Ashish Kulkarni, and Tsutomu Miyasaka. "Halide Perovskite Photovoltaics: Background, Status, and Future Prospects". In: *Chemical Reviews* 119.5 (2019), pp. 3036–3103. DOI: 10.1021/acs.chemrev.8b00539.

[36] *Best Research-Cell Efficiencies*. URL: https://www.nrel.gov/pv/cell-efficiency.html (visited on 10/15/2024).

[37] Anna Vinattieri and Giacomo Giorgi, eds. *Halide Perovskites for Photonics*. AIP Publishing LLCMelville, New York, 2021. ISBN: 978-0-7354-2360-2 978-0-7354-2363-3 978-0-7354-2361-9 978-0-7354-2362-6. DOI: 10.1063/9780735423633.

[38] Zeev Valy Vardeny, ed. *Spin Response of Hybrid Organic Inorganic Perovskites*. Hybrid organic inorganic perovskites / editors-in-chief: Zeev Valy Vardeny (University of Utah, USA), Matt C. Beard (National Renewable Energy Laboratory, USA) volume 3. New Jersey London Singapore Beijing Shanghai Hong Kong Taipei Chennai Tokyo: World Scientific, 2022. ISBN: 9789811242052 9789811242045.

[39] Jingying Wang, Chuang Zhang, Haoliang Liu, Ryan McLaughlin, Yaxin Zhai, Shai R. Vardeny, Xiaojie Liu, Stephen McGill, Dmitry Semenov, Hangwen Guo, Ryuichi Tsuchikawa, Vikram V. Deshpande, Dali Sun, and Z. Valy Vardeny. "Spin-optoelectronic devices based on hybrid organic-inorganic trihalide perovskites". In: *Nature Communications* 10.1 (2019), p. 129. DOI: 10.1038/s41467-018-07952-x.

[40] Weihua Ning, Jinke Bao, et al. "Magnetizing lead-free halide double perovskites". In: *Science Advances* 6.45 (2020), eabb5381. DOI: 10.1126/sciadv.abb5381.

[41] Young-Hoon Kim, Yaxin Zhai, Haipeng Lu, Xin Pan, Chuanxiao Xiao, E. Ashley Gaulding, Steven P. Harvey, Joseph J. Berry, Zeev Valy Vardeny, Joseph M. Luther, and Matthew C. Beard. "Chiral-induced spin selectivity enables a room-temperature spin light-emitting diode". In: *Science* 371.6534 (2021), pp. 1129–1133. DOI: 10.1126/science.abf5291.

[42] Mikhail I. Dyakonov, ed. *Spin Physics in Semiconductors*. Vol. 157. Springer Series in Solid-State Sciences. Springer International Publishing, 2017. DOI: 10.1007/978-3-319-65436-2.

[43] David Giovanni, Hong Ma, Julianto Chua, Michael Grätzel, Ramamoorthy Ramesh, Subodh Mhaisalkar, Nripan Mathews, and Tze Chien Sum. "Highly Spin-Polarized Carrier Dynamics and Ultralarge Photoinduced Magnetization in $CH_3NH_3PbI_3$ Perovskite Thin Films". In: *Nano Letters* 15.3 (2015), pp. 1553–1558. DOI: 10.1021/nl5039314.

[44] M. O. Nestoklon, S. V. Goupalov, R. I. Dzhioev, O. S. Ken, V. L. Korenev, Yu. G. Kusrayev, V. F. Sapega, C. De Weerd, L. Gomez, T. Gregorkiewicz, Junhao Lin, Kazutomo Suenaga, Yasufumi Fujiwara, L. B. Matyushkin, and I. N. Yassievich. "Optical orientation and alignment of excitons in ensembles of inorganic perovskite nanocrystals". In: *Physical Review B* 97.23 (2018), p. 235304. DOI: 10.1103/PhysRevB.97.235304.

[45] C. Zhang, D. Sun, C-X. Sheng, Y. X. Zhai, K. Mielczarek, A. Zakhidov, and Z. V. Vardeny. "Magnetic field effects in hybrid perovskite devices". In: *Nature Physics* 11.5 (2015), pp. 427–434. DOI: 10.1038/nphys3277.

[46] Chuang Zhang, Dali Sun, Zhi-Gang Yu, Chuan-Xiang Sheng, Stephen McGill, Dmitry Semenov, and Zeev Valy Vardeny. "Field-induced spin splitting and anomalous photoluminescence circular polarization in $CH_3NH_3PbI_3$ films at high magnetic field". In: *Physical Review B* 97.13 (2018), p. 134412. DOI: 10.1103/PhysRevB.97.134412.

[47] Patrick Odenthal, William Talmadge, Nathan Gundlach, Ruizhi Wang, Chuang Zhang, Dali Sun, Zhi-Gang Yu, Z. Valy Vardeny, and Yan S. Li. "Spin-polarized exciton quantum beating in hybrid organic-inorganic perovskites". In: *Nature Physics* 13.9 (2017), pp. 894–899. DOI: 10.1038/nphys4145.

[48] Vasilii V. Belykh, Dmitri R. Yakovlev, Mikhail M. Glazov, Philipp S. Grigoryev, Mujtaba Hussain, Janina Rautert, Dmitry N. Dirin, Maksym V. Kovalenko, and Manfred Bayer. "Coherent spin dynamics of electrons and holes in $CsPbBr_3$ perovskite crystals". In: *Nature Communications* 10.1 (2019), p. 673. DOI: 10.1038/s41467-019-08625-z.

[49] E. Kirstein, D. R. Yakovlev, M. M. Glazov, E. A. Zhukov, D. Kudlacik, I. V. Kalitukha, V. F. Sapega, G. S. Dimitriev, M. A. Semina, M. O. Nestoklon, E. L. Ivchenko, N. E. Kopteva, D. N. Dirin, O. Nazarenko, M. V. Kovalenko, A. Baumann, J. Höcker, V. Dyakonov, and M. Bayer. "The Landé factors of electrons and holes in lead halide perovskites: universal dependence on the band gap". In: *Nature Communications* 13.1 (2022), p. 3062. DOI: 10.1038/s41467-022-30701-0.

[50] Carolin Harkort, Dennis Kudlacik, Natalia E. Kopteva, Dmitri R. Yakovlev, Marek Karzel, Erik Kirstein, Oleh Hordiichuk, Maksym V. Kovalenko, and Manfred Bayer. "Spin-Flip Raman Scattering on Electrons and Holes in Two-Dimensional$(PEA)_2PbI_4$ Perovskites". In: *Small* 19.32 (2023), p. 2300988. DOI: 10.1002/smll.202300988.

[51] Erik Kirstein, Dmitri R. Yakovlev, Mikhail M. Glazov, Eiko Evers, Evgeny A. Zhukov, Vasilii V. Belykh, Nataliia E. Kopteva, Dennis Kudlacik, Olga Nazarenko, Dmitry N. Dirin, Maksym V. Kovalenko, and Manfred Bayer. "Lead-Dominated Hyperfine Interaction Impacting the Carrier Spin Dynamics in Halide Perovskites". In: *Advanced Materials* 34.1 (2022), p. 2105263. DOI: 10.1002/adma.202105263.

[52] Natalia E. Kopteva, Dmitri R. Yakovlev, Erik Kirstein, Evgeny A. Zhukov, Dennis Kudlacik, Ina V. Kalitukha, Victor F. Sapega, Oleh Hordiichuk, Dmitry N. Dirin, Maksym V. Kovalenko, et al. "Weak dispersion of exciton Landé factor with band gap energy in lead halide perovskites: Approximate compensation of the electron and hole dependences". In: *Small* 20.16 (2024), p. 2300935. DOI: 10.1002/smll.202300935.

[53] Simone Strohmair, Amrita Dey, Yu Tong, Lakshminarayana Polavarapu, Bernhard J. Bohn, and Jochen Feldmann. "Spin Polarization Dynamics of Free Charge Carriers in $CsPbI_3$ Nanocrystals". In: *Nano Letters* 20.7 (2020), pp. 4724–4730. DOI: 10.1021/acs.nanolett.9b05325.

[54] E. Kirstein, N. E. Kopteva, D. R. Yakovlev, E. A. Zhukov, E. V. Kolobkova, M. S. Kuznetsova, V. V. Belykh, I. A. Yugova, M. M. Glazov, M. Bayer, and A. Greilich. "Mode locking of hole spin coherences in $CsPb(Cl,Br)_3$ perovskite nanocrystals". In: *Nature Communications* 14.1 (2023), p. 699. DOI: 10.1038/s41467-023-36165-0.

[55] Vasilii V. Belykh, Mikhail L. Skorikov, Evgeniya V. Kulebyakina, Elena V. Kolobkova, Maria S. Kuznetsova, Mikhail M. Glazov, and Dmitri R. Yakovlev. "Submillisecond Spin Relaxation in $CsPb(Cl,Br)_3$ Perovskite Nanocrystals in a Glass Matrix". In: *Nano Letters* 22.11 (2022), pp. 4583–4588. DOI: 10.1021/acs.nanolett.2c01673.

[56] Meng Zhou, Julio S. Sarmiento, Chengbin Fei, Xinwen Zhang, and He Wang. "Effect of Composition on the Spin Relaxation of Lead Halide Perovskites". In: *The Journal of Physical Chemistry Letters* 11.4 (2020), pp. 1502–1507. DOI: 10.1021/acs.jpclett.0c00004.

[57] Weijian Tao, Qiaohui Zhou, and Haiming Zhu. "Dynamic polaronic screening for anomalous exciton spin relaxation in two-dimensional lead halide perovskites". In: *Science Advances* 6.47 (2020), eabb7132. DOI: 10.1126/sciadv.abb7132.

[58] David Giovanni, Jia Wei Melvin Lim, Zhongcheng Yuan, Swee Sien Lim, Marcello Righetto, Jian Qing, Qiannan Zhang, Herlina Arianita Dewi, Feng Gao, Subodh Gautam Mhaisalkar, Nripan Mathews, and Tze Chien Sum. "Ultrafast long-range spin-funneling in solution-processed Ruddlesden-Popper halide perovskites". In: *Nature Communications* 10.1 (2019), p. 3456. DOI: 10.1038/s41467-019-11251-4.

[59] Sean A. Bourelle, Ravichandran Shivanna, Franco V. A. Camargo, Soumen Ghosh, Alexander J. Gillett, Satyaprasad P. Senanayak, Sascha Feldmann, Lissa Eyre, Arjun Ashoka, Tim W. J. Van De Goor, Haralds Abolins, Thomas Winkler, Giulio Cerullo, Richard H. Friend, and Felix Deschler. "How Exciton Interactions Control Spin-Depolarization in Layered Hybrid Perovskites". In: *Nano Letters* 20.8 (2020), pp. 5678–5685. DOI: 10.1021/acs.nanolett.0c00867.

[60] Sean A. Bourelle, Franco V. A. Camargo, Soumen Ghosh, Timo Neumann, Tim W. J. Van De Goor, Ravichandran Shivanna, Thomas Winkler, Giulio Cerullo, and Felix Deschler. "Optical control of exciton spin dynamics in layered metal halide perovskites via polaronic state formation". In: *Nature Communications* 13.1 (2022), p. 3320. DOI: 10.1038/s41467-022-30953-w.

[61] Xuyang Lin, Yaoyao Han, Jingyi Zhu, and Kaifeng Wu. "Room-temperature coherent optical manipulation of hole spins in solution-grown perovskite quantum dots". In: *Nature Nanotechnology* 18.2 (2023), pp. 124–130. DOI: 10.1038/s41565-022-01279-x.

[62] Ruizhi Wang, Shu Hu, Xiao Yang, Xiaoliang Yan, Heng Li, and ChuanXiang Sheng. "Circularly polarized photoluminescence and Hanle effect measurements of spin relaxation in organic-inorganic hybrid perovskite films". In: *Journal of Materials Chemistry C* 6.12 (2018), pp. 2989–2995. DOI: 10.1039/C7TC05916G.

[63] Bo Wu, Haifeng Yuan, Qiang Xu, Julian A. Steele, David Giovanni, Pascal Puech, Jianhui Fu, Yan Fong Ng, Nur Fadilah Jamaludin, Ankur Solanki, Subodh Mhaisalkar, Nripan Mathews, Maarten B. J. Roeffaers, Michael Grätzel, Johan Hofkens, and Tze Chien Sum. "Indirect tail states formation by thermal-induced polar fluctuations in halide perovskites". In: *Nature Communications* 10.1 (2019), p. 484. DOI: 10.1038/s41467-019-08326-7.

[64] Karl W. Böer and Udo W. Pohl. *Semiconductor Physics*. Springer, 2023. DOI: 10.1007/978-3-031-18286-0.

[65] Gui-Bin Liu, Wen-Yu Shan, Yugui Yao, Wang Yao, and Di Xiao. "Three-band tight-binding model for monolayers of group-VIB transition metal dichalcogenides". In: *Physical Review B—Condensed Matter and Materials Physics* 88.8 (2013), p. 085433. DOI: 10.1103/PhysRevB.88.085433.

[66] Mikhail M. Glazov, Eougenious L. Ivchenko, Gang Wang, Thierry Amand, Xavier Marie, Bernhard Urbaszek, and B. L. Liu. "Spin and valley dynamics of excitons in transition metal dichalcogenide monolayers". In: *physica status solidi (b)* 252.11 (2015), pp. 2349–2362. DOI: 10.1002/pssb.201552211.

[67] Christopher Eames, Jarvist M Frost, Piers RF Barnes, Brian C O'regan, Aron Walsh, and M Saiful Islam. "Ionic transport in hybrid lead iodide perovskite solar cells". In: *Nature communications* 6.1 (2015), p. 7497. DOI: 10.1038/ncomms8497.

[68] Alain Diebold and Tino Hofmann. "Optical and electrical properties of transition metal dichalcogenides (Monolayer and Bulk)". In: *Optical and electrical properties of nanoscale materials* (2021), pp. 295–361.

[69] Alexander V. Kolobov and Junji Tominaga. "Electronic Band Structure of 2D TMDCs". In: *Two-Dimensional Transition-Metal Dichalcogenides* (2016), pp. 165–226.

[70] Mark Fox. *Optical Properties of Solids*. Vol. 3. Oxford university press, 2010.

[71] Heinz Kalt and Claus F. Klingshirn. *Semiconductor Optics 1*. Springer, 2019. DOI: 10.1007/978-3-030-24152-0.

[72] Nataliia E. Kopteva, Dmitri R. Yakovlev, Eyüp Yalcin, Ilya A. Akimov, Mikhail O. Nestoklon, Mikhail M. Glazov, Mladen Kotur, Dennis Kudlacik, Evgeny A. Zhukov, Erik Kirstein, Oleh Hordiichuk, Dmitry N. Dirin, Maksym V. Kovalenko, and Manfred Bayer. "Highly-Polarized Emission Provided by Giant Optical Orientation of Exciton Spins in Lead Halide Perovskite Crystals". In: *Advanced Science* 11.31 (2024), p. 2403691. DOI: 10.1002/advs.202403691.

[73] Igor Žutić, Jaroslav Fabian, and S. Das Sarma. "Spintronics: Fundamentals and Applications". In: *Reviews of modern physics* 76.2 (2004), p. 323.

[74] Laura M. Roth, Benjamin Lax, and Solomon Zwerdling. "Theory of optical magneto-absorption effects in semiconductors". In: *Physical Review* 114.1 (1959), p. 90. DOI: 10.1103/PhysRev.114.90.

[75] S. Chikazumi. *Physics of Ferromagnetism*. Vol. 506. Oxford University Press, 1997.

[76] A. K. Zvezdin and V. A. Kotov. *Modern Magnetooptics and Magnetooptical Materials*. CRC Press, 1997.

[77] Satoru Sugano and Norimichi Kojima. *Magneto-Optics*. Vol. 128. Springer Series in Solid-State Sciences. Springer, 2000. DOI: 10.1007/978-3-662-04143-7.

[78] Wilhelm Hanle. "Über magnetische Beeinflussung der Polarisation der Resonanzfluoreszenz". In: *Zeitschrift für Physik* 30.1 (1924), pp. 93–105. DOI: 10.1007/BF01331827.

[79] Feng Liu, A. V. Rodina, D. R. Yakovlev, A. Greilich, A. A. Golovatenko, A. S. Susha, A. L. Rogach, Yu. G. Kusrayev, and M. Bayer. "Exciton spin dynamics of colloidal CdTe nanocrystals in magnetic fields". In: *Phys. Rev. B* 89 (11 2014), p. 115306. DOI: 10.1103/PhysRevB.89.115306.

[80] Damien Canneson, Elena V. Shornikova, Dmitri R. Yakovlev, Tobias Rogge, Anatolie A. Mitioglu, Mariana V. Ballottin, Peter C. M. Christianen, Emmanuel Lhuillier, Manfred Bayer, and Louis Biadala. "Negatively charged and dark excitons in CsPbBr3 perovskite nanocrystals revealed by high magnetic fields". In: *Nano Letters* 17.10 (2017), pp. 6177–6183. DOI: 10.1021/acs.nanolett.7b02827.

[81] Eugeniyus Levovich Ivchenko. "Magnetic circular polarization of exciton photoluminescence". In: *Physics of the Solid State* 60 (2018), pp. 1514–1526. DOI: 10.1134/S1063783418080127.

[82] D. S. Smirnov, E. A. Zhukov, D. R. Yakovlev, E. Kirstein, M. Bayer, and A. Greilich. "Spin polarization recovery and Hanle effect for charge carriers interacting with nuclear spins in semiconductors". In: *Physical Review B* 102.23 (2020), p. 235413. DOI: 10.1103/PhysRevB.102.235413.

[83] Johan Erik Kirstein. "Coherent spin dynamics and carrier-nuclear interaction in lead halide perovskite crystals". PhD thesis. TU Dortmund University, 2022. DOI: 10.17877/DE290R-22888.

[84] I. A. Merkulov, Al. L. Efros, and M. Rosen. "Electron spin relaxation by nuclei in semiconductor quantum dots". In: *Physical Review B* 65.20 (2002), p. 205309. DOI: 10.1103/PhysRevB.65.205309.

[85] N. I. Zheludev, M. A. Brummell, R. T. Harley, A. Malinowski, S. V. Popov, D. E. Ashenford, and B. Lunn. "Giant specular inverse Faraday effect in Cd0. 6Mn0. 4Te". In: *Solid state communications* 89.10 (1994), pp. 823–825.

[86] S. A. Crooker, D. D. Awschalom, J. J. Baumberg, F. Flack, and N. Samarth. "Optical spin resonance and transverse spin relaxation in magnetic semiconductor quantum wells". In: *Physical Review B* 56.12 (1997), p. 7574.

[87] David Awschalom and Daniel Loss. *Semiconductor Spintronics and Quantum Computation*. Springer Science & Business Media, 2002. DOI: 10.1007/978-3-662-05003-3.

[88] J. M. Kikkawa and D. D. Awschalom. "Resonant spin amplification in n-type GaAs". In: *Physical Review Letters* 80.19 (1998), p. 4313.

[89] E. A. Zhukov, D. R. Yakovlev, M. Bayer, M. M. Glazov, E. L. Ivchenko, G. Karczewski, T. Wojtowicz, and J. Kossut. "Spin coherence of a two-dimensional electron gas induced by resonant excitation of trions and excitons in CdTe/(Cd,Mg)Te quantum wells". In: *Physical Review B* 76.20 (2007), p. 205310. DOI: 10.1103/PhysRevB.76.205310.

[90] I. A. Yugova, A. A. Sokolova, D. R. Yakovlev, A. Greilich, D. Reuter, A. D. Wieck, and M. Bayer. "Long-Term Hole Spin Memory in the Resonantly Amplified Spin Coherence of InGaAs/GaAs Quantum Well Electrons". In: *Physical review letters* 102.16 (2009), p. 167402. DOI: 10.1103/PhysRevLett.102.167402.

[91] Tobias Korn, Michael Kugler, Michael Griesbeck, Robert Schulz, A. Wagner, Michael Hirmer, Christian Gerl, Dieter Schuh, Werner Wegscheider, and Christian Schüller. "Engineering ultralong spin coherence in two-dimensional hole systems at low temperatures". In: *New Journal of Physics* 12.4 (2010), p. 043003.

[92] F. Heisterkamp, E. A. Zhukov, A. Greilich, D. R. Yakovlev, V. L. Korenev, A. Pawlis, and M. Bayer. "Longitudinal and transverse spin dynamics of donor-bound electrons in fluorine-doped ZnSe: Spin inertia versus Hanle effect". In: *Physical Review B* 91.23 (2015), p. 235432.

[93] E. A. Zhukov, E. Kirstein, N. E. Kopteva, F. Heisterkamp, I. A. Yugova, V. L. Korenev, D. R. Yakovlev, A. Pawlis, M Bayer., and A. Greilich. "Discretization of the total magnetic field by the nuclear spin bath in fluorine-doped ZnSe". In: *Nature Communications* 9.1 (2018), p. 1941.

[94] F. Saeed, M. Kuhnert, I. A. Akimov, V. L. Korenev, G. Karczewski, M. Wiater, T. Wojtowicz, A. Ali, A. S. Bhatti, D. R. Yakovlev, and M. Bayer. "Single-beam optical measurement of spin dynamics in CdTe/(Cd,Mg)Te quantum wells". In: *Physical Review B* 98.7 (2018), p. 075308. DOI: 10.1103/PhysRevB.98.075308.

[95] William Happer. "Optical pumping". In: *Reviews of modern physics* 44.2 (1972), p. 169.

[96] I. A. Akimov, D. H. Feng, and F. Henneberger. "Electron Spin Dynamics in a Self-Assembled Semiconductor Quantum Dot: The Limit of Low Magnetic Fields". In: *Physical Review Letters* 97.5 (2006), p. 056602. DOI: 10.1103/PhysRevLett.97.056602.

[97] G. V. Astakhov, M. M. Glazov, D. R. Yakovlev, E. A. Zhukov, W. Ossau, L. W. Molenkamp, and M. Bayer. "Time-resolved and continuous-wave optical spin pumping of semiconductor quantum wells". In: *Semiconductor Science and Technology* 23.11 (2008), p. 114001. DOI: 10.1088/0268-1242/23/11/114001.

[98] L. Langer, S. V. Poltavtsev, I. A. Yugova, M. Salewski, D. R. Yakovlev, G. Karczewski, T. Wojtowicz, I. A. Akimov, and M. Bayer. "Access to long-term optical memories using photon echoes retrieved from semiconductor spins". In: *Nature Photonics* 8.11 (2014), pp. 851–857.

[99] Ivan D. Avdeev and Dmitry S. Smirnov. "Hyperfine interaction in atomically thin transition metal dichalcogenides". In: *Nanoscale Advances* 1.7 (2019), pp. 2624–2632. DOI: 10.1039/C8NA00360B.

[100] R. I. Dzhioev, B. P. Zakharchenya, E. L. Ivchenko, V. L. Korenev, Yu. G. Kusraev, N. N. Ledentsov, V. M. Ustinov, A. E. Zhukov, and A. F. Tsatsul'nikov. "Fine structure of excitonic levels in quantum dots". In: *Journal of Experimental and Theoretical Physics Letters* 65.10 (1997), pp. 804–809. DOI: 10.1134/1.567429.

[101] C. Kittel. "Interaction of Spin Waves and Ultrasonic Waves in Ferromagnetic Crystals". In: *Physical Review* 110.4 (1958), pp. 836–841. DOI: 10.1103/PhysRev.110.836.

[102] I. V. Kalitukha, E. Yalcin, O. S. Ken, V. L. Korenev, I. A. Akimov, C. Harkort, G. S. Dimitriev, D. Kudlacik, V. F. Sapega, V. Nedelea, E. A. Zhukov, D. R. Yakovlev, A. G. Banshchikov, A. K. Kaveev, G. Karczewski, T. Wojtowicz, M. Müller, and M. Bayer. "Universal magnetic proximity effect in ferromagnet-semiconductor quantum well hybrid structures". In: *The Journal of Chemical Physics* 159.1 (2023), p. 014702. DOI: 10.1063/5.0153310.

[103] Mai Hussein Abdalla Hamed. "Interface Functionalization of Magnetic Oxide Fe_3O_4/$SrTiO_3$ Heterostructures". PhD thesis. Forschungzentrum Jülich, 2021.

[104] Mai Hussein Hamed, Ronja Anika Hinz, Patrick Lömker, Marek Wilhelm, Andrei Gloskovskii, Peter Bencok, Carolin Schmitz-Antoniak, Hebatalla Elnaggar, Claus M. Schneider, and Martina Müller. "Tunable Magnetic Phases at Fe_3O_4/$SrTiO_3$ Oxide Interfaces". In: *ACS Applied Materials & Interfaces* 11.7 (2019), pp. 7576–7583. DOI: 10.1021/acsami.8b20625.

[105] Mai Hussein Hamed, David N. Mueller, and Martina Müller. "Thermal phase design of ultrathin magnetic iron oxide films: from Fe_3O_4 to γ-Fe_2O_3 and FeO". In: *Journal of Materials Chemistry C* 8.4 (2020), pp. 1335–1343. DOI: 10.1039/C9TC05921K.

[106] Mai Hussein Hamed, David N. Mueller, and Martina Müller. "Active participation of inert YSZ substrates on interface formation in Fe_3O_4/YSZ heterostructures". In: *Applied Surface Science Advances* 6 (2021), p. 100132. DOI: 10.1016/j.apsadv.2021.100132.

[107] Martina Müller, Patrick Lömker, Paul Rosenberger, Mai Hussein Hamed, David N. Mueller, Ronja A. Heinen, Thomas Szyjka, and Lutz Baumgarten. "Hard x-ray photoelectron spectroscopy of tunable oxide interfaces". In: *Journal of Vacuum Science & Technology A* 40.1 (2022), p. 013215. DOI: 10.1116/6.0001491.

[108] Olga Nazarenko, Sergii Yakunin, Viktoriia Morad, Ihor Cherniukh, and Maksym V Kovalenko. "Single crystals of caesium formamidinium lead halide perovskites: solution growth and gamma dosimetry". In: *NPG Asia Materials* 9.4 (2017), e373–e373. DOI: 10.1038/am.2017.45.

[109] Julian Höcker, Felix Brust, Melina Armer, and Vladimir Dyakonov. "A temperature-reduced method for the rapid growth of hybrid perovskite single crystals with primary alcohols". In: *CrystEngComm* 23.11 (2021), pp. 2202–2207. DOI: 10.1039/D0CE01759K.

[110] Hamamatsu Photonics Deutschland GmbH. *Picosecond flourescence lifetime measurement streak camera.*

[111] Hamamatsu Photonics Deutschland GmbH. *High Performance Digital Temporal Analyzer Ver 8.4 HPD-TA users manual.*

[112] Theodore C Oakberg. "Magneto-optic Kerr effect". In: *Hinds Instruments* 1.1 (2005).

[113] D. T. Margulies, F. T. Parker, F. E. Spada, R. S. Goldman, J. Li, R. Sinclair, and A. E. Berkowitz. "Anomalous moment and anisotropy behavior in Fe_3O_4 films". In: *Physical Review B* 53.14 (1996), pp. 9175–9187. DOI: 10.1103/PhysRevB.53.9175.

[114] Dmitri R Yakovlev and Igor A Merkulov. "Spin and energy transfer between carriers, magnetic ions, and lattice". In: *Introduction to the Physics of Diluted Magnetic Semiconductors*. Springer, 2010, pp. 263–303. DOI: 10.1007/978-3-642-15856-8_8.

[115] A. A. Sirenko, T. Ruf, M. Cardona, D. R. Yakovlev, W. Ossau, A. Waag, and G. Landwehr. "Electron and hole g-factors measured by spin-flip Raman scattering in CdTe/$Cd_{1-x}Mg_xTe$ single quantum wells". In: *Physical Review B* 56.4 (1997), pp. 2114–2119. DOI: 10.1103/PhysRevB.56.2114.

[116] Donald E. Cooper and P. R. Newman. "Exciton-polariton dynamics and photoluminescence line shapes in cadmium telluride". In: *Physical Review B* 39.11 (1989), pp. 7431–7440. DOI: 10.1103/PhysRevB.39.7431.

[117] M. Bombeck, J. V. Jäger, A. V. Scherbakov, T. Linnik, D. R. Yakovlev, X. Liu, J. K. Furdyna, A. V. Akimov, and M. Bayer. "Magnetization precession induced by quasitransverse picosecond strain pulses in (311) ferromagnetic (Ga,Mn)As". In: *Physical Review B* 87.6 (2013), p. 060302. DOI: 10.1103/PhysRevB.87.060302.

[118] Eougenious L. Ivchenko and Grigory E. Pikus. *Superlattices and Other Heterostructures: Symmetry and Optical Phenomena*. Ed. by Manuel Cardona, Peter Fulde, Klaus Von Klitzing, Hans-Joachim Queisser, and Helmut K. V. Lotsch. Vol. 110. Springer Series in Solid-State Sciences. Berlin, Heidelberg: Springer Berlin Heidelberg, 1997. ISBN: 978-3-642-64493-1 978-3-642-60650-2. DOI: 10.1007/978-3-642-60650-2.

[119] V. F. Sapega, M. Cardona, K. Ploog, E. L. Ivchenko, and D. N. Mirlin. "Spin-flip Raman scattering in GaAs/Al_xGa_{1-x} As multiple quantum wells". In: *Physical Review B* 45.8 (1992), pp. 4320–4326. DOI: 10.1103/PhysRevB.45.4320.

[120] Eyüp Yalcin, Ina V. Kalitukha, Ilya A. Akimov, Vladimir L. Korenev, Olga S. Ken, Jorge Puebla, Yoshichika Otani, Oscar M. Hutchings, Daniel J. Gillard, Alexander I. Tartakovskii, et al. "Spin relaxation of localized electrons in monolayer $MoSe_2$: Importance of random effective magnetic fields". In: *Physical Review B* 110.16 (2024), p. L161405. DOI: 10.1103/PhysRevB.110.L161405.

[121] Andor Kormányos, Viktor Zólyomi, Neil D. Drummond, and Guido Burkard. "Spin-Orbit Coupling, Quantum Dots, and Qubits in Monolayer Transition Metal Dichalcogenides". In: *Physical Review X* 4.1 (2014), p. 011034. DOI: 10.1103/PhysRevX.4.011034.

[122] S. Döhrmann, D. Hägele, J. Rudolph, M. Bichler, D. Schuh, and M. Oestreich. "Anomalous Spin Dephasing in (110) GaAs Quantum Wells: Anisotropy and Intersubband Effects". In: *Physical Review Letters* 93.14 (2004), p. 147405. DOI: 10.1103/PhysRevLett.93.147405.

[123] R. I. Dzhioev, V. L. Korenev, I. A. Merkulov, B. P. Zakharchenya, D. Gammon, Al. L. Efros, and D. S. Katzer. "Manipulation of the Spin Memory of Electrons in n-GaAs". In: *Physical Review Letters* 88.25 (2002), p. 256801. DOI: 10.1103/PhysRevLett.88.256801.

[124] Maciej Koperski, Maciej R. Molas, Ashish Arora, Karol Nogajewski, Miroslav Bartos, Jan Wyzula, Diana Vaclavkova, Piotr Kossacki, and Marek Potemski. "Orbital, spin and valley contributions to Zeeman splitting of excitonic resonances in $MoSe_2$, WSe_2 and WS_2 Monolayers". In: *2D Materials* 6.1 (2018), p. 015001. DOI: 10.1088/2053-1583/aae14b.

[125] Nataliia E. Kopteva, Dmitri R. Yakovlev, Eyüp Yalcin, Ilya A. Akimov, Mladen Kotur, Bekir Turedi, Dmitry N. Dirin, Maksym V. Kovalenko, and Manfred Bayer. "Optical orientation of excitons and charge carriers in methylammonium lead iodide perovskite single crystals in the orthorhombic phase". In: *Phys. Rev. B* 111 (2025), p. 195201. DOI: 10.1103/PhysRevB.111.195201.

[126] Nataliia E. Kopteva, Dmitri R. Yakovlev, Eyüp Yalcin, Ina V. Kalitukha, Ilya A. Akimov, Mikhail O. Nestoklon, Bekir Turedi, Oleh Hordiichuk, Dmitry N. Dirin, Maksym V. Kovalenko, et al. "Effect of crystal symmetry of lead halide perovskites on the optical orientation of excitons". In: *Advanced Science* (2025), p. 2416782. DOI: 10.1002/advs.202416782.

[127] Stefan Grisard, Artur V. Trifonov, Ivan A. Solovev, Dmitri R. Yakovlev, Oleh Hordiichuk, Maksym V. Kovalenko, Manfred Bayer, and Ilya A. Akimov. "Long-Lived Exciton Coherence in Mixed-Halide Perovskite Crystals". In: *Nano Letters* 23.16 (2023), pp. 7397–7403. DOI: 10.1021/acs.nanolett.3c01817.

[128] Krzysztof Galkowski, Anatolie Mitioglu, Atsuhiko Miyata, Paulina Plochocka, Oliver Portugall, Giles E. Eperon, Jacob Tse-Wei Wang, Thomas Stergiopoulos, Samuel D. Stranks, Henry J. Snaith, and Robin J. Nicholas. "Determination of the exciton binding energy and effective masses for methylammonium and formamidinium lead tri-halide perovskite semiconductors". In: *Energy & Environmental Science* 9.3 (2016), pp. 962–970. DOI: 10.1039/C5EE03435C.

[129] Dennis Kudlacik, Nataliia E. Kopteva, Mladen Kotur, Dmitri R. Yakovlev, Kirill V. Kavokin, Carolin Harkort, Marek Karzel, Evgeny A. Zhukov, Eiko Evers, Vasilii V. Belykh, and Manfred Bayer. "Optical Spin Orientation of Localized Electrons and Holes Interacting with Nuclei in a $FA_{0.9}Cs_{0.1}PbI_{2.8}Br_{0.2}$ Perovskite Crystal". In: *ACS Photonics* 11.7 (2024), pp. 2757–2769. DOI: 10.1021/acsphotonics.4c00637.

[130] Michail M. Glazov. *Electron and Nuclear Spin Dynamics in Semiconductor Nanostructures*. Oxford science publications 23. Oxford New York: Oxford university press, 2018. DOI: 10.1093/oso/9780198807308.001.0001.

[131] Junqing Xu, Kejun Li, Uyen N. Huynh, Mayada Fadel, Jinsong Huang, Ravishankar Sundararaman, Valy Vardeny, and Yuan Ping. "How spin relaxes and dephases in bulk halide perovskites". In: *Nature Communications* 15.1 (2024), p. 188. DOI: 10.1038/s41467-023-42835-w.

[132] Jinsoo Park, Jin-Jian Zhou, and Marco Bernardi. "Spin-phonon relaxation times in centrosymmetric materials from first principles". In: *Physical Review B* 101.4 (2020), p. 045202. DOI: 10.1103/PhysRevB.101.045202.

[133] Go Yumoto, Fumiya Sekiguchi, Ruito Hashimoto, Tomoya Nakamura, Atsushi Wakamiya, and Yoshihiko Kanemitsu. "Rapidly expanding spin-polarized exciton halo in a two-dimensional halide perovskite at room temperature". In: *Science Advances* 8.30 (2022), eabp8135. DOI: 10.1126/sciadv.abp8135.

[134] A. P. Heberle, W. W. Rühle, and K. Ploog. "Quantum beats of electron Larmor precession in GaAs wells". In: *Physical Review Letters* 72.24 (1994), pp. 3887–3890. DOI: 10.1103/PhysRevLett.72.3887.

[135] M. Dyakonov, X. Marie, T. Amand, P. Le Jeune, D. Robart, M. Brousseau, and J. Barrau. "Coherent spin dynamics of excitons in quantum wells". In: *Physical Review B* 56.16 (1997), pp. 10412–10422. DOI: 10.1103/PhysRevB.56.10412.

[136] X. Marie, T. Amand, J. Barrau, P. Renucci, P. Lejeune, and V. K. Kalevich. "Electron-spin quantum-beat dephasing in quantum wells as a probe of the hole band structure". In: *Physical Review B* 61.16 (2000), pp. 11065–11077. DOI: 10.1103/PhysRevB.61.11065.

[137] Erik Kirstein, Dmitri R. Yakovlev, Evgeny A. Zhukov, Julian Höcker, Vladimir Dyakonov, and Manfred Bayer. "Spin Dynamics of Electrons and Holes Interacting with Nuclei in $MAPbI_3$ Perovskite Single Crystals". In: *ACS Photonics* 9.4 (2022), pp. 1375–1384. DOI: 10.1021/acsphotonics.2c00096.

[138] Snoop Dogg. *Acceptance Speech on Hollywood Walk of Fame*. Link. Accessed: 2025-03-16. 2018.

Associated Publications

[1] S. A. Dyakov, I. M. Fradkin, N. A. Gippius, L. Klompmaker, F. Spitzer, E. Yalcin, I. A. Akimov, M. Bayer, D. A. Yavsin, S. I. Pavlov, et al. "Wide-band enhancement of the transverse magneto-optical Kerr effect in magnetite-based plasmonic crystals". In: *Physical Review B* 100.21 (2019), p. 214411. DOI: 10.1103/PhysRevB.100.214411.

[2] Lars Klompmaker, Alexander N. Poddubny, Eyüp Yalcin, Leonid V. Litvin, Ralf Jede, Grzegorz Karczewski, Sergij Chusnutdinow, Tomasz Wojtowicz, Dmitri R. Yakovlev, Manfred Bayer, et al. "Transverse magnetic routing of light emission in hybrid plasmonic-semiconductor nanostructures: Towards operation at room temperature". In: *Physical Review Research* 4.1 (2022), p. 013058. DOI: 10.1103/PhysRevResearch.4.013058.

[3] I. V. Kalitukha, E. Yalcin, O. S. Ken, V. L. Korenev, I. A. Akimov, C. Harkort, G. S. Dimitriev, D. Kudlacik, V. F. Sapega, V. Nedelea, E. A. Zhukov, D. R. Yakovlev, A. G. Banshchikov, A. K. Kaveev, G. Karczewski, T. Wojtowicz, M. Müller, and M. Bayer. "Universal magnetic proximity effect in ferromagnet-semiconductor quantum well hybrid structures". In: *The Journal of Chemical Physics* 159.1 (2023), p. 014702. DOI: 10.1063/5.0153310.

[4] Erik Kirstein, Evgeny A. Zhukov, Dmitri R. Yakovlev, Nataliia E. Kopteva, Eyüp Yalcin, Ilya A. Akimov, Oleh Hordiichuk, Dmitry N. Dirin, Maksym V. Kovalenko, and Manfred Bayer. "Coherent carrier spin dynamics in FAPbBr3 perovskite crystals". In: *The Journal of Physical Chemistry Letters* 15.10 (2024), pp. 2893–2903. DOI: 10.1021/acs.jpclett.4c00098.

[5] Nataliia E. Kopteva, Dmitri R. Yakovlev, Eyüp Yalcin, Ilya A. Akimov, Mikhail O. Nestoklon, Mikhail M. Glazov, Mladen Kotur, Dennis Kudlacik, Evgeny A. Zhukov, Erik Kirstein, Oleh Hordiichuk, Dmitry N. Dirin, Maksym V. Kovalenko, and Manfred Bayer. "Highly-Polarized Emission Provided by Giant Optical Orientation of Exciton Spins in Lead Halide Perovskite Crystals". In: *Advanced Science* 11.31 (2024), p. 2403691. DOI: 10.1002/advs.202403691.

[6] Eyüp Yalcin, Ina V. Kalitukha, Ilya A. Akimov, Vladimir L. Korenev, Olga S. Ken, Jorge Puebla, Yoshichika Otani, Oscar M. Hutchings, Daniel J. Gillard, Alexander I. Tartakovskii, et al. "Spin relaxation of localized electrons in monolayer $MoSe_2$: Importance of random effective magnetic fields". In: *Physical Review B* 110.16 (2024), p. L161405. DOI: 10.1103/PhysRevB.110.L161405.

[7] Nataliia E. Kopteva, Dmitri R. Yakovlev, Eyüp Yalcin, Ina V. Kalitukha, Ilya A. Akimov, Mikhail O. Nestoklon, Bekir Turedi, Oleh Hordiichuk, Dmitry N. Dirin, Maksym V. Kovalenko, et al. "Effect of crystal symmetry of lead halide perovskites on the optical orientation of excitons". In: *Advanced Science* (2025), p. 2416782. DOI: 10.1002/advs.202416782.

[8] Nataliia E. Kopteva, Dmitri R. Yakovlev, Eyüp Yalcin, Ilya A. Akimov, Mladen Kotur, Bekir Turedi, Dmitry N. Dirin, Maksym V. Kovalenko, and Manfred Bayer. "Optical orientation of excitons and charge carriers in methylammonium lead iodide perovskite single crystals in the orthorhombic phase". In: *Phys. Rev. B* 111 (2025), p. 195201. DOI: 10.1103/PhysRevB.111.195201.

Acknowledgements

I would like to express my gratitude to all those who have contributed to the academic journey and this thesis. I am thankful to:
Prof. Dr. Manfred Bayer for giving me the opportunity to work in his research group and providing a friendly and modern working environment.
Prof. Dr. Marc Aßmann for representing the chair and commitment.
Prof. Dr. Ilya Akimov for supervising, his patience, guidance and numerous discussions through all the journey.
Prof. Dr. Vladimir Korenev, Dr. Olga Ken, Dr. Ina Kalitukha, Dr. Natalia Kopteva, Prof. Dr. Dmitiri Yakovlev, Prof. Dr. Evgeny Zhukov, Prof. Dr. Alexander Tartakovskii, Dr. Daniel Gillard, involved in the projects.
My colleagues and friends from the office Martin Bergen and Mariam Harati for the talks and discussion about physics, experiments and life.
Dr. Dennis Kudlacik, Dr. Artur Trifonov, Dr. Erik Kirstein, Dr. Carolin Lüders, Dr. Felix Godejohann and Dr. Alex Greilich for discussions and support regarding experimental methods, data analysis and evaluation techniques.
Dr. Alexey Scherbakov, Dr. Anton Samusev and Marek Karzel for the nice atmosphere in the laboratory.
The colleagues from the chair who have enriched the academic environment and made it pleasant. Special thanks to Michaela Wäscher and Katharina Goldack for the administrative support, and furthermore, Lars Wieschollek, Patrick McLelland and Daniel Tüttmann for the technical assistance and support, and for providing of liquid helium and liquid nitrogen.
I am grateful to my parents Sakir and Gülbeyaz, my brothers Adem and Dr. Ertugrul, and my friends for all the support.
And finally, “I want to thank me for believing in me. I want to thank me for doing all this hard work. I want to thank me for having no days off. I want to thank me for never quitting. I want to thank me for always being a giver and trying to give more than I receive. I want to thank me for trying to do more right than wrong. I want to thank me for just being me at all times.” [138] Do not give up when you are faced with problems. Trust the process and accept the challenge.